

## Resonance production and $\pi\pi$ S-wave in $\pi^- + p \rightarrow \pi^- \pi^- \pi^+ + p_{\text{recoil}}$ at 190 GeV/c

C. Adolph,<sup>9</sup> R. Akhunzhanov,<sup>8</sup> M. G. Alexeev,<sup>28</sup> G. D. Alexeev,<sup>8</sup> A. Amoroso,<sup>28,29</sup> V. Andrieux,<sup>22</sup> V. Anosov,<sup>8</sup>  
W. Augustyniak,<sup>31</sup> A. Austregesilo,<sup>17</sup> C. D. R. Azevedo,<sup>2</sup> B. Badelek,<sup>32</sup> F. Balestra,<sup>28,29</sup> J. Barth,<sup>5</sup> R. Beck,<sup>4</sup> Y. Bedfer,<sup>22,11</sup>  
J. Bernhard,<sup>14,11</sup> K. Bicker,<sup>17,11</sup> E. R. Bielert,<sup>11</sup> R. Birsa,<sup>26</sup> J. Bisplinghoff,<sup>4</sup> M. Bodlak,<sup>19</sup> M. Boer,<sup>22</sup> P. Bordalo,<sup>13,d</sup>  
F. Bradamante,<sup>25,26</sup> C. Braun,<sup>9</sup> A. Bressan,<sup>25,26</sup> M. Büchele,<sup>10</sup> E. Burtin,<sup>22</sup> W.-C. Chang,<sup>23</sup> M. Chiosso,<sup>28,29</sup> I. Choi,<sup>30</sup>  
S.-U. Chung,<sup>17,e</sup> A. Cicuttin,<sup>27,26</sup> M. L. Crespo,<sup>27,26</sup> Q. Curiel,<sup>22</sup> S. Dalla Torre,<sup>26</sup> S. S. Dasgupta,<sup>7</sup> S. Dasgupta,<sup>25,26</sup>  
O. Yu. Denisov,<sup>29,a</sup> L. Dhara,<sup>7</sup> S. V. Donskov,<sup>21</sup> N. Doshita,<sup>34</sup> V. Duic,<sup>25</sup> W. Dünneweber,<sup>f</sup> M. Dziewiecki,<sup>33</sup> A. Efremov,<sup>8</sup>  
P. D. Eversheim,<sup>4</sup> W. Eyrich,<sup>9</sup> M. Faessler,<sup>f</sup> A. Ferrero,<sup>22</sup> M. Finger,<sup>19</sup> M. Finger, Jr.,<sup>19</sup> H. Fischer,<sup>10</sup> C. Franco,<sup>13</sup>  
N. du Fresne von Hohenesche,<sup>14</sup> J. M. Friedrich,<sup>17</sup> V. Frolov,<sup>8,11</sup> E. Fuchey,<sup>22</sup> F. Gautheron,<sup>3</sup> O. P. Gavrichtchouk,<sup>8</sup>  
S. Gerassimov,<sup>16,17</sup> F. Giordano,<sup>30</sup> I. Gnesi,<sup>28,29</sup> M. Gorzellik,<sup>10</sup> S. Grabmüller,<sup>17</sup> A. Grasso,<sup>28,29</sup> M. Grosse Perdekamp,<sup>30</sup>  
B. Grube,<sup>17,b</sup> T. Grussenmeyer,<sup>10</sup> A. Guskov,<sup>8</sup> F. Haas,<sup>17</sup> D. Hahne,<sup>5</sup> D. von Harrach,<sup>14</sup> R. Hashimoto,<sup>34</sup> F. H. Heinsius,<sup>10</sup>  
F. Herrmann,<sup>10</sup> F. Hinterberger,<sup>4</sup> N. Horikawa,<sup>18,g</sup> N. d'Hose,<sup>22</sup> C.-Y. Hsieh,<sup>23</sup> S. Huber,<sup>17</sup> S. Ishimoto,<sup>34,h</sup> A. Ivanov,<sup>8</sup>  
Yu. Ivanshin,<sup>8</sup> T. Iwata,<sup>34</sup> R. Jahn,<sup>4</sup> V. Jary,<sup>20</sup> R. Joosten,<sup>4</sup> P. Jörg,<sup>10</sup> E. Kabuß,<sup>14</sup> B. Ketzer,<sup>17,i</sup> G. V. Khaustov,<sup>21</sup>  
Yu. A. Khokhlov,<sup>21,j</sup> Yu. Kisselev,<sup>8</sup> F. Klein,<sup>5</sup> K. Klimaszewski,<sup>31</sup> J. H. Koivuniemi,<sup>3</sup> V. N. Kolosov,<sup>8</sup> K. Kondo,<sup>34</sup>  
K. Königsmann,<sup>10</sup> I. Konorov,<sup>16,17</sup> V. F. Konstantinov,<sup>21</sup> A. M. Kotzinian,<sup>28,29</sup> O. Kouznetsov,<sup>8</sup> M. Krämer,<sup>17</sup> P. Kremser,<sup>10</sup>  
F. Krinner,<sup>17</sup> Z. V. Kroumchtein,<sup>8</sup> N. Kuchinski,<sup>8</sup> F. Kunne,<sup>22</sup> K. Kurek,<sup>31</sup> R. P. Kurjata,<sup>33</sup> A. A. Lednev,<sup>21</sup> A. Lehmann,<sup>9</sup>  
M. Levillain,<sup>22</sup> S. Levorato,<sup>26</sup> J. Lichtenstadt,<sup>24</sup> R. Longo,<sup>28,29</sup> A. Maggiora,<sup>29</sup> A. Magnon,<sup>22</sup> N. Makins,<sup>30</sup> N. Makke,<sup>25,26</sup>  
G. K. Mallot,<sup>11,c</sup> C. Marchand,<sup>22</sup> B. Marianski,<sup>31</sup> A. Martin,<sup>25,26</sup> J. Marzec,<sup>33</sup> J. Matoušek,<sup>19</sup> H. Matsuda,<sup>34</sup> T. Matsuda,<sup>15</sup>  
G. Meshcheryakov,<sup>8</sup> W. Meyer,<sup>3</sup> T. Michigami,<sup>34</sup> Yu. V. Mikhailov,<sup>21</sup> Y. Miyachi,<sup>34</sup> P. Montuenga,<sup>30</sup> A. Nagaytsev,<sup>8</sup> F. Nerling,<sup>14</sup>  
D. Neyret,<sup>22</sup> V. I. Nikolaenko,<sup>21</sup> J. Nový,<sup>20,11</sup> W.-D. Nowak,<sup>10</sup> G. Nukazuka,<sup>34</sup> A. S. Nunes,<sup>13</sup> A. G. Olshevsky,<sup>8</sup> I. Orlov,<sup>8</sup>  
M. Ostrick,<sup>14</sup> D. Panzieri,<sup>1,29</sup> B. Parsamyan,<sup>28,29</sup> S. Paul,<sup>17</sup> J.-C. Peng,<sup>30</sup> F. Pereira,<sup>2</sup> M. Pešek,<sup>19</sup>  
D. V. Peshekhonov,<sup>8</sup> S. Platchkov,<sup>22</sup> J. Pochodzalla,<sup>14</sup> V. A. Polyakov,<sup>21</sup> J. Pretz,<sup>5,k</sup> M. Quaresma,<sup>13</sup> C. Quintans,<sup>13</sup> S. Ramos,<sup>13,d</sup>  
C. Regali,<sup>10</sup> G. Reicherz,<sup>3</sup> C. Riedl,<sup>30</sup> N. S. Rossiyskaya,<sup>8</sup> D. I. Ryabchikov,<sup>21,l</sup> A. Rychter,<sup>33</sup> V. D. Samoylenko,<sup>21</sup> A. Sandacz,<sup>31</sup>  
C. Santos,<sup>26</sup> S. Sarkar,<sup>7</sup> I. A. Savin,<sup>8</sup> G. Sbrizzai,<sup>25,26</sup> P. Schiavon,<sup>25,26</sup> T. Schlüter,<sup>f</sup> K. Schmidt,<sup>10,m</sup> H. Schmieden,<sup>5</sup>  
K. Schönning,<sup>11,n</sup> S. Schopferer,<sup>10</sup> A. Selyunin,<sup>8</sup> O. Yu. Shevchenko,<sup>8,\*</sup> L. Silva,<sup>13</sup> L. Sinha,<sup>7</sup> S. Sirtl,<sup>10</sup> M. Slunecka,<sup>8</sup> F. Sozzi,<sup>26</sup>  
A. Srnka,<sup>6</sup> M. Stolarski,<sup>13</sup> M. Sulc,<sup>12</sup> H. Suzuki,<sup>34,o</sup> A. Szabelski,<sup>31</sup> T. Szameitat,<sup>10,m</sup> P. Sznajder,<sup>31</sup> S. Takekawa,<sup>28,29</sup> S. Tessaro,<sup>26</sup>  
F. Tessarotto,<sup>26</sup> F. Thibaud,<sup>22</sup> F. Tosello,<sup>29</sup> V. Tskhay,<sup>16</sup> S. Uhl,<sup>17</sup> J. Veloso,<sup>2</sup> M. Virius,<sup>20</sup> T. Weisrock,<sup>14</sup> M. Wilfert,<sup>14</sup>  
J. ter Wolbeek,<sup>10,p</sup> K. Zaremba,<sup>33</sup> M. Zavertyaev,<sup>16</sup> E. Zemlyanichkina,<sup>8</sup> M. Ziembicki,<sup>33</sup> and A. Zink<sup>9</sup>

(COMPASS Collaboration)

<sup>1</sup>University of Eastern Piedmont, 15100 Alessandria, Italy

<sup>2</sup>University of Aveiro, Department of Physics, 3810-193 Aveiro, Portugal

<sup>3</sup>Universität Bochum, Institut für Experimentalphysik, 44780 Bochum, Germany

<sup>4</sup>Universität Bonn, Helmholtz-Institut für Strahlen- und Kernphysik, 53115 Bonn, Germany

<sup>5</sup>Universität Bonn, Physikalisches Institut, 53115 Bonn, Germany

<sup>6</sup>Institute of Scientific Instruments, AS CR, 61264 Brno, Czech Republic

<sup>7</sup>Matrivani Institute of Experimental Research & Education, Calcutta 700 030, India

<sup>8</sup>Joint Institute for Nuclear Research, 141980 Dubna, Moscow region, Russia

<sup>9</sup>Universität Erlangen–Nürnberg, Physikalisches Institut, 91054 Erlangen, Germany

<sup>10</sup>Universität Freiburg, Physikalisches Institut, 79104 Freiburg, Germany

<sup>11</sup>CERN, 1211 Geneva 23, Switzerland

<sup>12</sup>Technical University in Liberec, 46117 Liberec, Czech Republic

<sup>13</sup>LIP, 1000-149 Lisbon, Portugal

<sup>14</sup>Universität Mainz, Institut für Kernphysik, 55099 Mainz, Germany

<sup>15</sup>University of Miyazaki, Miyazaki 889-2192, Japan

<sup>16</sup>Lebedev Physical Institute, 119991 Moscow, Russia

<sup>17</sup>Technische Universität München, Physik Department, 85748 Garching, Germany

<sup>18</sup>Nagoya University, 464 Nagoya, Japan

<sup>19</sup>Charles University in Prague, Faculty of Mathematics and Physics, 18000 Prague, Czech Republic

<sup>20</sup>Czech Technical University in Prague, 16636 Prague, Czech Republic

<sup>21</sup>State Scientific Center Institute for High Energy Physics of National Research Center

‘Kurchatov Institute’, 142281 Protvino, Russia

<sup>22</sup>CEA IRFU/SPhN Saclay, 91191 Gif-sur-Yvette, France

<sup>23</sup>Academia Sinica, Institute of Physics, Taipei, 11529 Taiwan

<sup>24</sup>Tel Aviv University, School of Physics and Astronomy, 69978 Tel Aviv, Israel

<sup>25</sup>University of Trieste, Department of Physics, 34127 Trieste, Italy

<sup>26</sup>*Trieste Section of INFN, 34127 Trieste, Italy*<sup>27</sup>*Abdus Salam ICTP, 34151 Trieste, Italy*<sup>28</sup>*University of Turin, Department of Physics, 10125 Turin, Italy*<sup>29</sup>*Torino Section of INFN, 10125 Turin, Italy*<sup>30</sup>*University of Illinois at Urbana-Champaign, Department of Physics, Urbana, Illinois 61801-3080, USA*<sup>31</sup>*National Centre for Nuclear Research, 00-681 Warsaw, Poland*<sup>32</sup>*University of Warsaw, Faculty of Physics, 02-093 Warsaw, Poland*<sup>33</sup>*Warsaw University of Technology, Institute of Radioelectronics, 00-665 Warsaw, Poland*<sup>34</sup>*Yamagata University, Yamagata, 992-8510 Japan*

(Received 3 September 2015; published 16 February 2017)

The COMPASS collaboration has collected the currently largest data set on diffractively produced  $\pi^- \pi^- \pi^+$  final states using a negative pion beam of 190 GeV/ $c$  momentum impinging on a stationary proton target. This data set allows for a systematic partial-wave analysis in 100 bins of three-pion mass,  $0.5 < m_{3\pi} < 2.5$  GeV/ $c^2$ , and in 11 bins of the reduced four-momentum transfer squared,  $0.1 < t' < 1.0$  (GeV/ $c$ )<sup>2</sup>. This two-dimensional analysis offers sensitivity to genuine one-step resonance production, i.e. the production of a state followed by its decay, as well as to more complex dynamical effects in nonresonant  $3\pi$  production. In this paper, we present detailed studies on selected  $3\pi$  partial waves with  $J^{PC} = 0^{-+}, 1^{++}, 2^{-+}, 2^{++},$  and  $4^{++}$ . In these waves, we observe the well-known ground-state mesons as well as a new narrow axial-vector meson  $a_1(1420)$  decaying into  $f_0(980)\pi$ . In addition, we present the results of a novel method to extract the amplitude of the  $\pi^- \pi^+$  subsystem with  $I^G J^{PC} = 0^+ 0^{++}$  in various partial waves from the  $\pi^- \pi^- \pi^+$  data. Evidence is found for correlation of the  $f_0(980)$  and  $f_0(1500)$  appearing as intermediate  $\pi^- \pi^+$  isobars in the decay of the known  $\pi(1800)$  and  $\pi_2(1880)$ .

DOI: 10.1103/PhysRevD.95.032004

\*Deceased.

<sup>a</sup>Corresponding author.  
oleg.denisov@cern.ch<sup>b</sup>Corresponding author.  
bgrube@tum.de<sup>c</sup>Corresponding author.  
gerhard.mallot@cern.ch<sup>d</sup>Also at Instituto Superior Técnico, Universidade de Lisboa, Lisbon, Portugal.<sup>e</sup>Also at Department of Physics, Pusan National University, Busan 609-735, Republic of Korea and at Physics Department, Brookhaven National Laboratory, Upton, NY 11973, U.S.A.<sup>f</sup>Supported by the DFG cluster of excellence ‘Origin and Structure of the Universe’ ([www.universe-cluster.de](http://www.universe-cluster.de)).<sup>g</sup>Also at Chubu University, Kasugai, Aichi, 487-8501 Japan.<sup>h</sup>Also at KEK, 1-1 Oho, Tsukuba, Ibaraki, 305-0801 Japan.<sup>i</sup>Present address: Universität Bonn, Helmholtz-Institut für Strahlen- und Kernphysik, 53115 Bonn, Germany.<sup>j</sup>Also at Moscow Institute of Physics and Technology, Moscow Region, 141700, Russia; supported by Presidential grant NSh—999.2014.2.<sup>k</sup>Present address: RWTH Aachen University, III. Physikalisches Institut, 52056 Aachen, Germany.<sup>l</sup>Supported by Presidential grant NSh—999.2014.2.<sup>m</sup>Supported by the DFG Research Training Group Programme 1102 ‘Physics at Hadron Accelerators.’<sup>n</sup>Present address: Uppsala University, Box 516, SE-75120 Uppsala, Sweden.<sup>o</sup>Also at Chubu University, Kasugai, Aichi, 487-8501 Japan.<sup>p</sup>Supported by the DFG Research Training Group Programme 1102 ‘Physics at Hadron Accelerators.’

*Published by the American Physical Society under the terms of the Creative Commons Attribution 3.0 License. Further distribution of this work must maintain attribution to the author(s) and the published article’s title, journal citation, and DOI.*

## I. INTRODUCTION

In this paper, we report on the results of a partial-wave analysis of the  $\pi^- \pi^- \pi^+$  system produced by a 190 GeV/ $c$   $\pi^-$  beam impinging on a liquid-hydrogen target. The reaction of interest is diffractive dissociation of a  $\pi^-$  into a  $\pi^- \pi^- \pi^+$  system,

$$\pi^- + p \rightarrow \pi^- \pi^- \pi^+ + p_{\text{recoil}}, \quad (1)$$

with  $p_{\text{recoil}}$  denoting the recoiling target proton. The data for this analysis were recorded with the COMPASS experiment at the CERN SPS in 2008.

Despite many decades of research in hadron spectroscopy, the excitation spectrum of light mesons, which are made of  $u$ ,  $d$ , and  $s$  quarks, is still only partially known. In the framework of the simple constituent-quark model using  $SU(3)_{\text{flavor}} \otimes SU(2)_{\text{spin}} \otimes SU(3)_{\text{color}}$  symmetry, a number of frequently observed states are commonly interpreted in terms of orbital and radial excitations of quark-antiquark ground-state mesons, i.e. they are assigned to the multiplets resulting from the symmetry. Some of these assignments are still disputed, as e.g. the isovector mesons  $\rho(1450)$ ,  $\rho(1700)$ ,  $\pi(1300)$ , and  $\pi(1800)$  [1], as well as the whole sector of scalar mesons [2]. In addition, a number of extra states have been found, which cannot be accommodated by the constituent-quark model. These extra states appear in mass ranges where quark-model states have already been identified, e.g. the  $\pi_2(1880)$  which is close to the  $\pi_2(1670)$

ground state. Other observed states seem to have peculiar decay modes or decay widths that do not fit well into the general pattern. Searching for new states beyond the constituent-quark model, attempts have been made to establish the existence of gluonic degrees of freedom. The fingerprints are expected to be so-called *exotic* spin quantum numbers<sup>1</sup> or decay branching ratios, which could identify them as *hybrids* [3,4], *glueballs* [5,6], or *tetra-quark systems* [1]. Potential candidates are e.g.  $\pi_1(1600)$ ,  $\pi(1800)$ ,  $\pi_2(1880)$  or  $f_0(1500)$ ,  $f_0(1710)$  or  $f_0(980)$ ,  $a_0(980)$ ,  $f_1(1420)$ , respectively.

The COMPASS collaboration has already studied properties of isovector  $3\pi$  resonances [7,8] in the mass range between 1.1 and 2.1 GeV/ $c^2$  using a lead target. In this paper, isovector mesons decaying into three charged pions are studied using a hydrogen target with the emphasis on (i) production kinematics, (ii) separation of nonresonant processes, (iii) search for new and excited mesons, and (iv) on properties of the  $\pi\pi$  S-wave amplitude. This paper is the first in a planned series of publications to present precision studies revisiting all quantum numbers accessible in reaction (1) up to total spin  $J = 6$ . The analysis is limited to states belonging to the family of  $\pi_J$  and  $a_J$ . In addition, the large data set allows us to apply a novel method for investigating isoscalar states, which occur as  $\pi^-\pi^+$  subsystems in the decays of isovector mesons.

The Particle Data Group (PDG) [9] lists a total of eleven well-established isovector states with masses below 2.1 GeV/ $c^2$  (see Table I), where only the  $a_0$  states do not decay into  $3\pi$  due to parity conservation. The widths of the  $a_0$ ,  $a_2$ , and  $a_4$  ground states have values of about 10% of their mass values, while the  $a_1(1260)$  is much broader. Pionic excitations are typically broader with values of their width being about 15% to 20% of their mass values. In addition, the table contains a number of less well-established states. Even for some established states, properties such as mass and width are poorly determined, e.g. for the  $a_1(1260)$  as the lightest  $a_1$  state, the reported widths vary between 250 and 600 MeV/ $c^2$ . Another example is the inconsistency in the mass measurements of  $\pi(1800)$ , where experimental results cluster around two different mean values. This has led to speculations on the existence of two states, one being an ordinary meson and the other one a hybrid. Extensive discussions of the light-meson sector are found in Refs. [1,10].

The partial-wave analysis of the  $3\pi$  system has a long history [1]. The technique of partial-wave analysis (PWA) of  $3\pi$  systems was established by the work of Ascoli *et al.* [11,12] in 1968. The CERN-Munich collaboration (ACCMOR) [13–16] further developed this method and measured significant contributions from partial waves up to

<sup>1</sup> $J^{PC}$  quantum numbers that are forbidden for  $q\bar{q}$  in the nonrelativistic limit.

TABLE I. Resonance parameters of  $a_J$  and  $\pi_J$  mesons in the mass region below 2.1 GeV/ $c^2$  as given in PDG [9]. Note that due to parity conservation the  $a_0$  states cannot decay into  $\pi^-\pi^-\pi^+$ .

Particle	$J^{PC}$	Mass [MeV/ $c^2$ ]	Width [MeV/ $c^2$ ]
Established states			
$a_0(980)$	$0^{++}$	$980 \pm 20$	50 to 100
$a_1(1260)$	$1^{++}$	$1230 \pm 40$	250 to 600
$a_2(1320)$	$2^{++}$	$1318.3_{-0.6}^{+0.5}$	$107 \pm 5$
$a_0(1450)$	$0^{++}$	$1474 \pm 19$	$265 \pm 13$
$a_4(2040)$	$4^{++}$	$1996_{-9}^{+10}$	$255_{-24}^{+28}$
$\pi(1300)$	$0^{-+}$	$1300 \pm 100$	200 to 600
$\pi_1(1400)$	$1^{-+}$	$1354 \pm 25$	$330 \pm 35$
$\pi_1(1600)$	$1^{-+}$	$1662_{-9}^{+8}$	$241 \pm 40$
$\pi_2(1670)$	$2^{-+}$	$1672.2 \pm 3.0$	$260 \pm 9$
$\pi(1800)$	$0^{-+}$	$1812 \pm 12$	$208 \pm 12$
$\pi_2(1880)$	$2^{-+}$	$1895 \pm 16$	$235 \pm 34$
States omitted from summary table			
$a_1(1640)$	$1^{++}$	$1647 \pm 22$	$254 \pm 27$
$a_2(1700)$	$2^{++}$	$1732 \pm 16$	$194 \pm 40$
$\pi_2(2100)$	$2^{-+}$	$2090 \pm 29$	$625 \pm 50$
Further states			
$a_3(1875)$	$3^{++}$	$1874 \pm 43 \pm 96$	$385 \pm 121 \pm 114$
$a_1(1930)$	$1^{++}$	$1930_{-70}^{+30}$	$155 \pm 45$
$a_2(1950)$	$2^{++}$	$1950_{-70}^{+30}$	$180_{-70}^{+30}$
$a_2(1990)$	$2^{++}$	$2050 \pm 10 \pm 40$	$190 \pm 22 \pm 100$
		$2003 \pm 10 \pm 19$	$249 \pm 23 \pm 32$
$a_0(2020)$	$0^{++}$	$2025 \pm 30$	$330 \pm 75$
$a_2(2030)$	$2^{++}$	$2030 \pm 20$	$205 \pm 30$
$a_3(2030)$	$3^{++}$	$2031 \pm 12$	$150 \pm 18$
$a_1(2095)$	$1^{++}$	$2096 \pm 17 \pm 121$	$451 \pm 41 \pm 81$
$\pi_2(2005)$	$2^{-+}$	$1974 \pm 14 \pm 83$	$341 \pm 61 \pm 139$
		$2005 \pm 15$	$200 \pm 40$
$\pi_1(2015)$	$1^{-+}$	$2014 \pm 20 \pm 16$	$230 \pm 32 \pm 73$
		$2001 \pm 30 \pm 92$	$333 \pm 52 \pm 49$
$\pi(2070)$	$0^{-+}$	$2070 \pm 35$	$310_{-50}^{+100}$
$X(1775)$	$?^{-+}$	$1763 \pm 20$	$192 \pm 60$
		$1787 \pm 18$	$118 \pm 60$
$X(2000)$	$?^{2+}$	$1964 \pm 35$	$225 \pm 50$
		$\sim 2100$	$\sim 500$
		$2214 \pm 15$	$355 \pm 21$
		$2080 \pm 40$	$340 \pm 80$

$J = 2$ , without including spin-exotic waves. The largest data set used so far, which is the basis of several publications on the  $3\pi$  final state, was obtained and analyzed by the BNL E852 collaboration [17–19]. They have studied reaction (1) at beam momenta of 18 GeV/ $c$  and observed significant waves with  $J^{PC} = 0^{-+}, 1^{++}, 2^{++}$ , and  $2^{-+}$  quantum numbers. In addition, they have detected a  $1^{-+}$  spin-exotic wave in the  $\rho(770)\pi$  decay channel with significant fluctuation in intensity depending on the number of partial waves used, i.e. with a considerable model dependence. Also the VES experiment has large data sets,

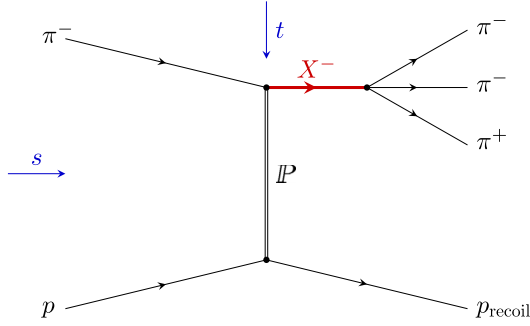


FIG. 1. Diffractive dissociation of a beam pion on a target proton into the three-pion final state. The figure shows the excitation of an intermediate resonance  $X^-$  via Pomeron exchange and its subsequent decay into  $3\pi$ .

the analysis of which was published mostly in conference proceedings, see e.g. Refs. [20–23].

As illustrated in Fig. 1, for reaction (1) at 190 GeV beam energy, the strong interaction can be described by the exchange of a quasiparticle called Pomeron,  $\mathbb{P}$ , which is a flavorless glueball-like object that accounts for diffractive dissociation and most of the two-body elastic scattering [24]. The Regge trajectory  $\alpha_{\mathbb{P}}(t)$  of the Pomeron determines the elastic scattering amplitude

$$A(s, t) \propto s^{\alpha_{\mathbb{P}}(t)}. \quad (2)$$

Here,  $s$  is the squared center-of-mass energy,  $t$  the squared four-momentum transferred between beam particle and target nucleon, and

$$\alpha_{\mathbb{P}}(t) = 1 + \epsilon_{\mathbb{P}} + \alpha'_{\mathbb{P}} t, \quad (3)$$

where  $0.081 \lesssim \epsilon_{\mathbb{P}} \lesssim 0.112$  and  $\alpha'_{\mathbb{P}} \approx 0.25$  (GeV/c) $^{-2}$  [24]. The Pomeron is an even-signature Regge trajectory with  $J^{PC} = 2^{++}, 4^{++}, 6^{++}, \dots$ , and its first Regge pole corresponds to a flavorless hadron with  $J^{PC} = 2^{++}$  and a mass of about 1.9 GeV/c $^2$ . The parameter  $\alpha'_{\mathbb{P}}$  modifies the dependence of the differential cross section on the four-momentum transfer. Equation (2) implies a dependence of the cross section on  $t$  as

$$\frac{d\sigma}{dt} \propto e^{-bt}. \quad (4)$$

The slope parameter  $b$  is given by

$$b = b_0 + 4\alpha'_{\mathbb{P}} \ln \sqrt{\frac{s}{s_0}}, \quad (5)$$

where  $b_0$  is a generic slope parameter and the unknown scale parameter  $s_0$  is usually taken to be 1 GeV $^2$ . The reduced four-momentum transfer squared is

$$t' \equiv |t| - |t|_{\min} \geq 0, \quad \text{where } |t|_{\min} \approx \left( \frac{m_{3\pi}^2 - m_{\pi}^2}{2|\vec{p}_{\text{beam}}|} \right)^2 \quad (6)$$

is the minimum momentum transfer needed to excite the beam particle to a mass  $m_{3\pi}$ , which is the invariant mass of the  $3\pi$  final state. The beam momentum  $\vec{p}_{\text{beam}}$  is measured in the laboratory frame. For the  $3\pi$  mass range of 0.5 to 2.5 GeV/c $^2$  considered in this analysis, typical values of  $|t|_{\min}$  are well below  $10^{-3}$  (GeV/c) $^2$ . Different production mechanisms, i.e. different exchange particles, can lead to different slopes  $b$ . The existence of concurrent exchange processes thus results in a more complex form of the  $t'$  dependence with coherently and/or incoherently overlapping exponentials. The  $t'$  range for this analysis is 0.1 to 1.0 (GeV/c) $^2$ .

Studies of diffractive dissociation of pions, see e.g. Refs. [8,16,19,22], reveal the existence of nonresonant background processes such as the Deck effect [25]. These processes exhibit strongly mass-dependent production amplitudes that occur in the same partial waves as the resonances under study. In particular, the analyses presented in Refs. [16,19] showed the importance of the kinematic variable  $t'$  in a partial-wave analysis and illustrated the power of accounting for the difference in the  $t'$  dependence of the reaction mechanisms and also of the different resonances. In this work, we take advantage of the large size of our data sample and develop this approach further in order to better disentangle resonant and non-resonant components.

In the case of Pomeron exchange, the partial waves induced by a pion beam can be assessed as follows: the  $\pi^-$  is an isovector pseudoscalar with negative  $G$  parity and the Pomeron is assumed to be an isoscalar  $C = +1$  object, so that the partial waves all have  $I^G = 1^-$ . Possible  $J^{PC}$  quantum numbers<sup>2</sup> of partial waves are listed in Table II for the lowest values of the relative orbital angular momentum  $\ell$  between the beam particle and a  $J^{PC} = 2^{++}$  Pomeron as an example. As we will demonstrate in this paper, almost all partial waves listed in Table II are indeed observed in our data. Higher-spin waves with  $J \geq 5$  contribute significantly only at masses above 2 GeV/c $^2$ . The table includes spin-exotic partial waves such as  $J^{PC} = 1^{-+}, 3^{-+}$ , and  $5^{-+}$ . The present paper focuses on nonexotic spin quantum numbers with the emphasis on known states. They are extracted from the data by partial-wave methods that contain an *a priori* unknown dependence on  $t'$ , which is extracted from the data.

<sup>2</sup>Although the  $C$  parity is not defined for a charged system, it is customary to quote the  $J^{PC}$  quantum numbers of the corresponding neutral partner state in the isospin multiplet. The  $C$  parity can be generalized to the  $G$  parity  $G \equiv C e^{i\pi I_y}$ , a multiplicative quantum number, which is defined for the nonstrange states of a meson multiplet.

TABLE II. List of allowed  $J^{PC}$  quantum numbers for  $X$  assuming that it is produced in the interaction of a  $J^{PC} = 0^{-+}$  beam pion and a  $2^{++}$  Pomeron as an example, with relative orbital angular momentum  $\ell$  between the two.

$\ell$	$J^{PC}$ of $X$
0	$2^{-+}$
1	$1^{++}, 2^{++}, 3^{++}$
2	$0^{-+}, 1^{-+}, 2^{-+}, 3^{-+}, 4^{-+}$
3	$1^{++}, 2^{++}, 3^{++}, 4^{++}, 5^{++}$
4	$2^{-+}, 3^{-+}, 4^{-+}, 5^{-+}, 6^{-+}$
⋮	

The work related to this topic is subdivided into two publications, owing to the large amount of material and various, in parts novel analysis techniques used. This paper contains details on the experiment in Sec. II A and a description of the basic event selection criteria in Secs. II B and II C, where we also present the general features of our data set and the overall kinematic distributions for both  $m_{3\pi}$  and  $t'$ . Section III contains a detailed description of our analysis method and the PWA model used. For clarity, we include a rather extensive mathematical description summarizing the work of many authors, who laid the basis for our analysis (see e.g. Refs. [26–32]). In this scheme, the analysis follows a two-step procedure described in Ref. [32]. In the first step, a PWA is performed in bins of  $m_{3\pi}$  and  $t'$ . The results of this so-called *mass-independent* fit are presented and discussed in Secs. IV and V. In these and the following sections, the focus lies on  $3\pi$  resonances with masses below  $2.1 \text{ GeV}/c^2$ . The discussion on  $t'$  dependences includes the kinematic distributions and  $J^{PC}$ -resolved  $t'$  spectra. In Sec. VI, we present a novel approach that allows us to investigate the amplitude of  $\pi^-\pi^+$  subsystems in the decay process. In particular, we address the topic of the scalar sector containing  $f_0$  mesons and its complicated relation to  $\pi\pi$  S-wave scattering. The relation of  $f_0(980)$  and  $f_0(1500)$  mesons to  $\pi\pi$  scattering will be demonstrated. In this paper, all error bars shown in the figures represent statistical uncertainties only. Systematic effects are discussed in Sec. IV F and Appendix B. In Sec. VII, we conclude by summarizing the findings based on qualitative arguments. The appendices contain details about more technical issues.

The analysis methods and results presented in this paper will serve as a basis for further publications that will be dedicated to individual partial waves. In the second step of the analysis, physics parameters will be extracted from the data presented in this paper by performing a fit that models the resonance amplitudes and the amplitudes of nonresonant processes. This involves simultaneous fitting to many partial-wave amplitudes in all bins of  $t'$ . Such a *mass-dependent* fit, which will allow us to extract the  $t'$  dependences of various components, i.e. resonant

and nonresonant contributions for individual partial waves as well as resonance parameters for the mesonic states observed with different  $J^{PC}$ , will be described in a forthcoming paper [33].

## II. EXPERIMENTAL SETUP AND EVENT SELECTION

### A. COMPASS Setup

The COMPASS spectrometer, which is described in general in Ref. [34], is situated at the CERN SPS. The setup used for the measurement presented here is explained in more detail in Ref. [35]. COMPASS uses secondary hadron and tertiary muon beams that are produced by the  $400 \text{ GeV}/c$  SPS proton beam impinging on a  $50 \text{ cm}$  long beryllium target. The measurement described in this paper is based on data recorded during the 2008 COMPASS run. The beam was tuned to deliver negatively charged hadrons of  $190 \text{ GeV}/c$  momentum passing through a pair of beam Cherenkov detectors (CEDARs) for beam particle identification. The beam impinged on a  $40 \text{ cm}$  long liquid-hydrogen target with an intensity of  $5 \times 10^7$  particles per SPS spill ( $10 \text{ s}$  extraction with a repetition time of  $45 \text{ s}$ ). At the target, the hadronic component of the beam consisted of  $96.8\% \pi^-$ ,  $2.4\% K^-$ , and  $0.8\% \bar{p}$ . In addition, the beam contained about  $1\% \mu^-$  and an even smaller amount of electrons.

The target was surrounded by a recoil-proton detector (RPD) consisting of two concentric, inner and outer, barrels of scintillators with 12 and 24 azimuthal segments, respectively. Recoil protons emerging from diffraction-like reactions must carry momenta of at least  $270 \text{ MeV}/c$  in order to traverse the target containment and to be detected in the two RPD rings. This leads to a minimum detectable squared four-momentum transfer  $t'$  of about  $0.07 \text{ GeV}/c^2$ .

Incoming beam particles and outgoing reaction products that emerge in the forward region were detected by a set of silicon microstrip detector stations, each consisting of two double-sided detector modules that were arranged to view four projections. Particles emerging in the forward direction were momentum-analyzed by the two-stage magnetic spectrometer with a wide angular acceptance of  $\pm 180 \text{ mrad}$ . Both spectrometer stages are each composed of a bending magnet, charged-particle tracking, electromagnetic and hadronic calorimetry, and muon identification. Particles in the momentum range between  $2.5$  and  $50 \text{ GeV}/c$  and passing through the ring-imaging Cherenkov (RICH) detector in the first stage can be identified as pion, kaon, or proton. The experiment offers large acceptance and high reconstruction efficiency over a wide range of three-pion mass  $m_{3\pi}$  and squared four-momentum transfer  $t'$ .

### B. Hardware trigger

A minimum-bias trigger, the so-called *diffractive trigger* (DT0) [35,36], was used to preselect events with interacting beam particles and a recoiling proton emerging from the target. The trigger elements are shown schematically in

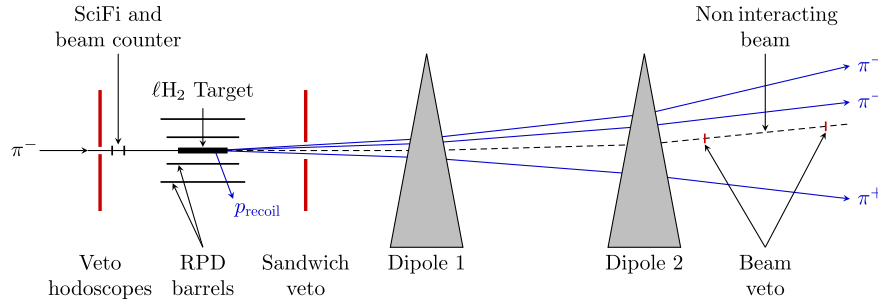


FIG. 2. Simplified scheme of the diffractive trigger. The main components are the beam trigger, which selects beam particles, and the RPD, which triggers on slow charged particles leaving the target. The veto system (red) rejects uninteresting events and consists of three parts: The veto hodoscopes, the sandwich, and the beam veto.

Fig. 2. The DT0 trigger is a coincidence of three independent trigger signals: (i) the *beam trigger*, (ii) the *recoil-proton trigger*, and (iii) the veto signal. Incoming beam particles are selected by the beam trigger requiring a signal in one plane of the scintillating-fiber detector (SciFi) in coincidence with a hit in the beam counter, which is a scintillator disc of 32 mm diameter and 4 mm thickness. Both beam-trigger elements are located upstream of the target. The proton trigger selects events with protons recoiling from the target. It features target pointing and discrimination of protons from other charged particles by measuring the energy loss in each ring of the RPD. The veto signal has three subcomponents. The *veto hodoscopes* reject incoming beam particles with trajectories far from the nominal one. Similarly, the *sandwich* scintillation detector that is positioned downstream close to the target, vetoes events with particles leaving the target area outside of the geometrical acceptance of the spectrometer. Lastly, the *beam veto*, two scintillator discs of 35 mm diameter and 5 mm thickness positioned between the second analyzing magnet and the second electromagnetic calorimeter, vetoes signals from noninteracting beam particles. Events recorded with the diffractive trigger can be regarded as good candidates for diffractive dissociation reactions.

### C. Event selection

The analysis is based on a data set of about  $6.4 \times 10^9$  events selected by the hardware trigger (see Sec. II B). The event selection aims at a clean sample of exclusive  $\pi^- + p \rightarrow \pi^- \pi^- \pi^+ + p_{\text{recoil}}$  events (see Fig. 1) and consists of the following criteria (see Ref. [37] for more details):

- (1) A vertex is required to be formed by the beam particle and three charged outgoing tracks with a total charge sum of  $-1$ . The vertex must be located within the fiducial volume of the liquid-hydrogen target.
- (2) Momentum conservation is applied by requiring exactly one recoil particle detected in the RPD that is back-to-back with the outgoing  $\pi^- \pi^- \pi^+$  system in the plane transverse to the beam (transverse momentum balance). This suppresses contributions

from double-diffractive processes, in which also the target proton is excited.

- (3) The beam energy  $E_{\text{beam}}$ , which is calculated from the energy and momentum of the three outgoing particles corrected for the target recoil, must be within a window of  $\pm 3.78$  GeV around the nominal beam energy, which corresponds to two standard deviations [see Fig. 3(a)].

A number of additional selection criteria is applied in order to reject background events originating from other processes. Events are disregarded if the incoming beam particle is identified by the two beam Cherenkov detectors (CEDARs) as a kaon. This suppresses kaon-beam induced events, like e.g.  $K^- + p \rightarrow K^- \pi^- \pi^+ + p_{\text{recoil}}$ . If at least one of the three forward-going particles is identified by the RICH detector as a kaon, proton, electron, muon, or noise, the event is rejected, thereby suppressing events such as e.g.  $\pi^- + p \rightarrow \pi^- K^- K^+ + p_{\text{recoil}}$ . In order to reject background events stemming from the central-production reaction  $\pi^- + p \rightarrow \pi^-_{\text{fast}} + \pi^- \pi^+ + p_{\text{recoil}}$ , in which no three-pion resonances are formed, the faster  $\pi^-$  in the event is required to have a Feynman- $x$  below 0.9 defined in the overall center-of-mass frame. The rapidity difference between the faster  $\pi^-$  and the remaining  $\pi^- \pi^+$  pair is limited to the range from 2.7 to 4.5. Figure 4 shows the  $m_{3\pi}$  and  $m_{\pi^- \pi^+}$  distributions of the sample that is cut away.

After all cuts, the data sample consists of  $46 \times 10^6$  events in the analyzed kinematic region of three-pion mass,  $0.5 < m_{3\pi} < 2.5$  GeV/ $c^2$ , and four-momentum transfer squared,  $0.1 < t' < 1.0$  (GeV/ $c$ ) $^2$ . Figures 5(a) and 5(b) show for all selected events the mass spectrum of  $\pi^- \pi^- \pi^+$  and of the two  $\pi^- \pi^+$  combinations. The known pattern of resonances  $a_1(1260)$ ,  $a_2(1320)$ , and  $\pi_2(1670)$  is seen in the  $3\pi$  system as well as  $\rho(770)$ ,  $f_0(980)$ ,  $f_2(1270)$ , and  $\rho_3(1690)$  in the  $\pi^- \pi^+$  subsystem. From Fig. 5(c), the correlation of the resonances in the  $\pi^- \pi^- \pi^+$  system and in the  $\pi^- \pi^+$  subsystem is clearly visible. This correlation is the basis of our analysis model described in Sec. III. The  $t'$  spectrum is shown in Fig. 5(d).

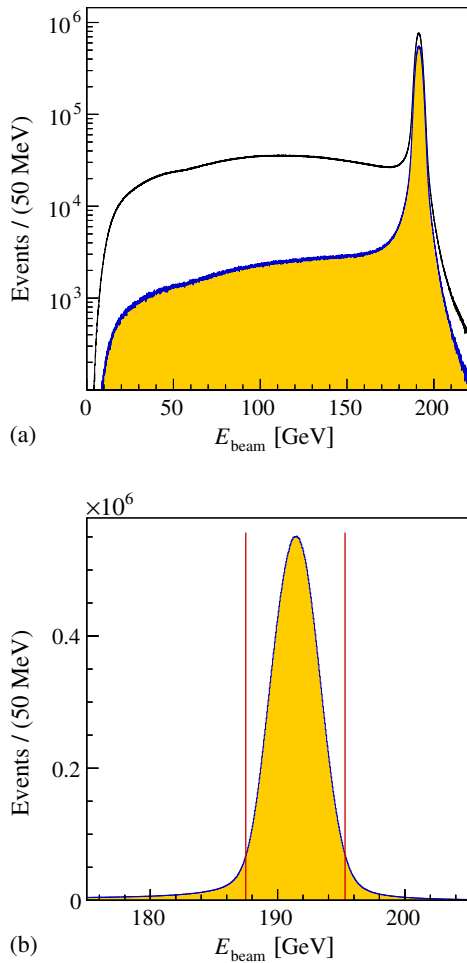


FIG. 3. Panels (a) and (b) show the reconstructed beam energy  $E_{\text{beam}}$  after selection cuts (filled histograms). The open histogram in (a) represents the energy distribution without the RPD information. In the zoomed view (b), the vertical red lines indicate the accepted range.

A Monte Carlo simulation has shown that for the reaction under study, the  $3\pi$  mass resolution of the spectrometer varies between  $5.4 \text{ MeV}/c^2$  at small  $m_{3\pi}$  (in the range from  $0.5$  to  $1.0 \text{ GeV}/c^2$ ) and  $15.5 \text{ MeV}/c^2$  at large  $m_{3\pi}$  (in the range from  $2.0$  to  $2.5 \text{ GeV}/c^2$ ), respectively. The  $t'$  resolution as obtained from the reconstructed  $3\pi$  final state ranges between  $7 \times 10^{-3}$  and  $20 \times 10^{-3} \text{ (GeV}/c^2)$  depending on the  $m_{3\pi}$  and  $t'$  region. The resolution of the reconstructed beam energy  $E_{\text{beam}}$  is smaller than the intrinsic energy spread of the beam and varies between  $0.6$  and  $0.9 \text{ GeV}$ . The position of the primary interaction vertex along the beam axis is reconstructed with a resolution of approximately  $6 \text{ mm}$  at small and  $1.5 \text{ mm}$  at large  $m_{3\pi}$ . The overall *detection efficiency*, which includes detector acceptance, reconstruction efficiency, and event selection, is estimated for isotropically distributed (phase-space)  $\pi^-\pi^-\pi^+$  events. Integrated over the analyzed kinematic region, it is  $49\%$  on average. More details are found in Appendix C and Ref. [37].

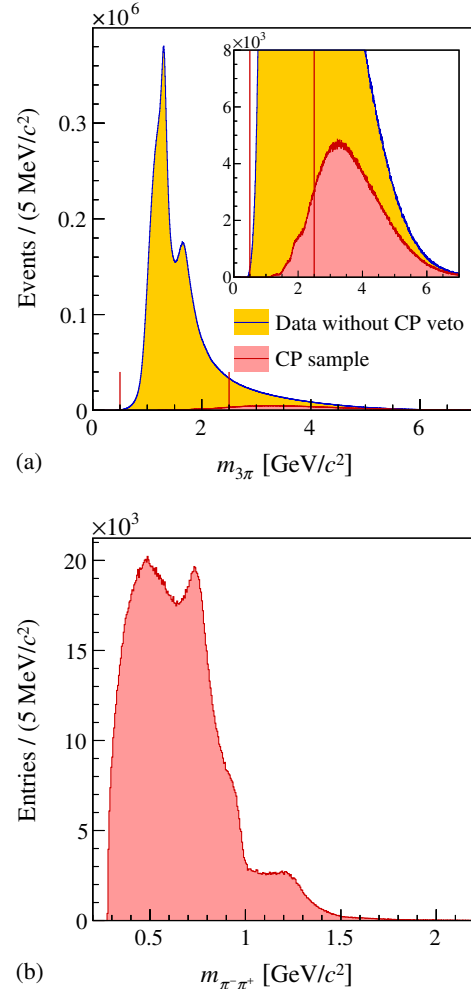


FIG. 4. Effect of the central-production (CP) veto. Panel (a):  $\pi^-\pi^-\pi^+$  invariant mass spectrum without the central-production veto (yellow histogram) together with the sample that is removed by the central-production veto (red histogram). The inset shows the same histogram with magnified ordinate scale. Note that the partial-wave analysis is performed only in the mass region of  $0.5 < m_{3\pi} < 2.5 \text{ GeV}/c^2$  indicated by the vertical red lines. Panel (b):  $\pi^-\pi^+$  invariant mass distribution (two entries per event) of the sample that is cut away.

### III. PARTIAL-WAVE ANALYSIS METHOD

The goal of the analysis described in this paper is to extract the resonances contributing to the reaction  $\pi^- + p \rightarrow \pi^-\pi^-\pi^+ + p_{\text{recoil}}$  and to determine their quantum numbers from the observed kinematic distributions of the outgoing  $\pi^-\pi^-\pi^+$  system. This is accomplished using partial-wave analysis techniques. The basic assumption is that resonances dominate the  $3\pi$  intermediate states  $X^-$  produced in the scattering process, so that the  $X^-$  production can be treated independently of the  $X^-$  decay (see Fig. 1). The amplitude for a certain intermediate state  $X^-$  is therefore factorized into two terms: (i) the *transition amplitude*  $\mathcal{T}$  describing the production of a state  $X^-$  with

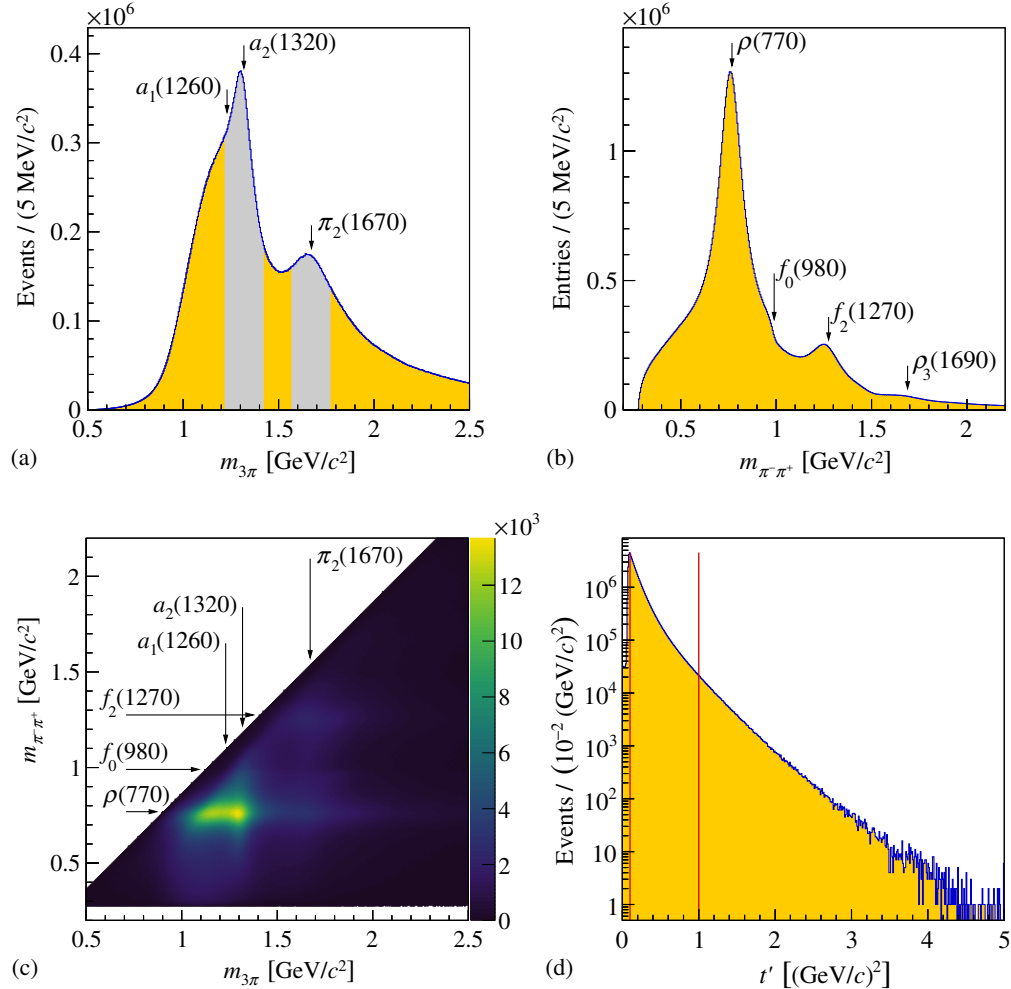


FIG. 5. Final event sample after all selection cuts: (a) invariant mass spectrum of  $\pi^- \pi^- \pi^+$  in the range used in this analysis [see vertical lines in Fig. 4(a)], (b)  $\pi^- \pi^+$  mass distribution, (c) correlation of the two, (d)  $t'$  distribution with vertical lines indicating the range of  $t'$  values used in this analysis. The histograms in (b) and (c) have two entries per event. The labels indicate the position of major  $3\pi$  and  $2\pi$  resonances, the gray shaded areas in (a) the mass regions used to generate the Dalitz plots in Fig. 6.

specific quantum numbers and (ii) the *decay amplitude*  $\Psi$  that describes the decay of the  $X^-$  state into a particular  $\pi^- \pi^- \pi^+$  final state. For fixed beam energy, the measured kinematic distribution of the final-state particles depends on the  $3\pi$  invariant mass  $m_{3\pi}$ , the four-momentum transfer squared  $t'$ , and a set of five additional phase-space variables denoted as  $\tau$ , which fully describe the three-body decay and are defined below.

### A. Isobar model

In order to illustrate the isobar ansatz, we give in Fig. 6 two examples for Dalitz plots for two different regions of  $m_{3\pi}$ . In the  $3\pi$  mass region around  $a_2(1320)$ , which also includes contributions from  $a_1(1260)$ , we see a dominant contribution of the  $\rho(770)$  in the  $\pi^- \pi^+$  subsystem, while for values of  $m_{3\pi}$  around  $\pi_2(1670)$  several  $2\pi$  resonances contribute, i.e.  $\rho(770)$ ,  $f_0(980)$ , and  $f_2(1270)$ .

Because of the strong contribution of resonances in the  $\pi^- \pi^+$  subsystem, the three-body decay amplitude  $\tilde{\Psi}(\tau, m_{3\pi})$

is factorized into two two-body decay terms (see Fig. 7). This factorization is known as the *isobar model*<sup>3</sup> and the introduced intermediate  $\pi^- \pi^+$  state  $\xi$  is called the *isobar*. In the first two-body decay,  $X^- \rightarrow \xi^0 + \pi^-$ , a relative orbital angular momentum  $L$  is involved in the decay. The decay amplitude  $\tilde{\Psi}(\tau, m_{3\pi})$  completely describes the kinematic distribution of the three outgoing pions for particular quantum numbers of  $X^-$  and for a particular isobar channel with a given  $L$ .

The two subsequent two-body decays are described in different right-handed coordinate systems, i.e. the Gottfried-Jackson and the helicity reference frame (see Fig. 8). The Gottfried-Jackson (GJ) frame is used to describe the angular distribution of the decay of the intermediate state  $X^-$  into the isobar  $\xi$  and the bachelor pion. It is constructed in the  $X^-$  rest system, in which the direction of the beam particle defines the  $z_{\text{GJ}}$  axis and the

<sup>3</sup>An early detailed discussion can be found in Ref. [30].

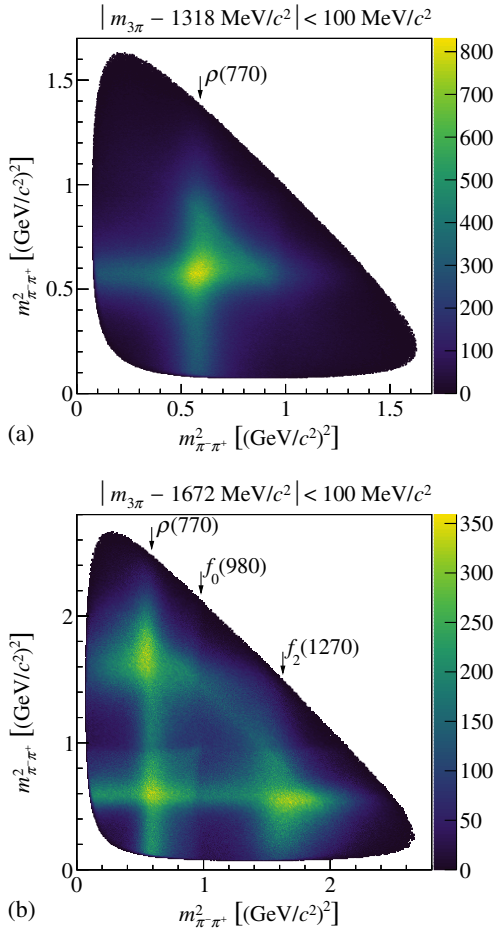


FIG. 6. (a) Dalitz plot in the mass regions of the  $a_2(1320)$ , which also includes the  $a_1(1260)$ , (b) around the  $\pi_2(1670)$ . The used  $3\pi$  mass regions are indicated in Fig. 5(a). The dominant  $\rho(770)$   $\pi$  decays of  $a_1(1260)$  and  $a_2(1320)$  are clearly visible. The  $\pi_2(1670)$  region exhibits  $\rho(770)$   $\pi$ ,  $f_2(1270)$   $\pi$ , and  $f_0(980)$   $\pi$  decay modes.

$y_{\text{GJ}}$  axis is oriented along the normal to the production plane ( $\hat{y}_{\text{GJ}} \equiv \hat{p}_{\text{beam}}^{\text{lab}} \times \hat{p}_X^{\text{lab}} = \hat{p}_{\text{recoil}}^{\text{GJ}} \times \hat{p}_{\text{beam}}^{\text{GJ}}$ , where unit vectors are indicated by a circumflex). In this system, the momenta of the isobar and the bachelor pion are back to back, so that the two-body decay  $X^- \rightarrow \xi^0 + \pi^-$  is

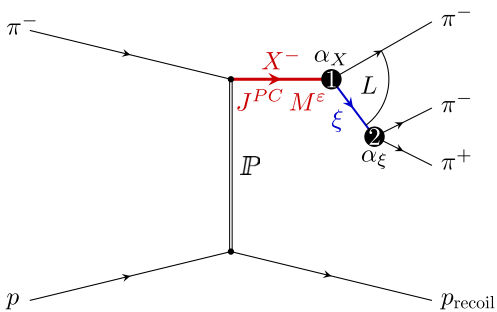


FIG. 7. The decay of  $X^-$ , as described in the isobar model, is assumed to proceed via an intermediate  $\pi^- \pi^+$  state  $\xi$ , the so-called isobar.

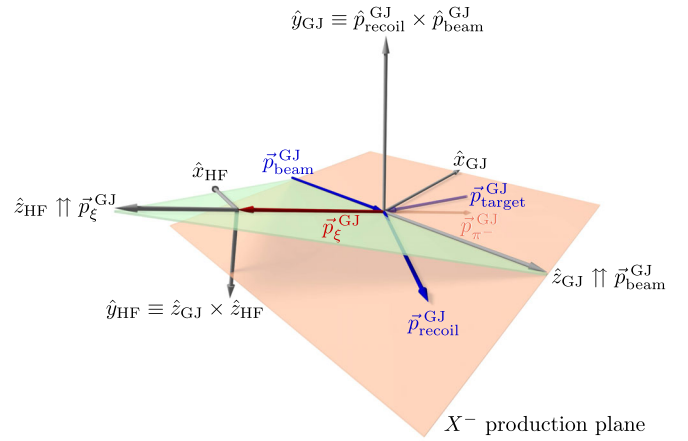


FIG. 8. Definition of the Gottfried-Jackson reference frame (GJ) in the  $X^-$  rest system and of the helicity reference frame (HF) in the  $\xi^0$  rest system as they are used to analyze the angular distributions of the decays  $X^- \rightarrow \xi^0 + \pi^-$  and  $\xi^0 \rightarrow \pi^- + \pi^+$ , respectively. Unit vectors are indicated by a circumflex.

described by the polar angle  $\vartheta_{\text{GJ}}$  and the azimuthal angle  $\phi_{\text{TY}}$  of the isobar, the latter being also referred to as Treiman-Yang angle.

For the decay of the isobar  $\xi$  into  $\pi^- \pi^+$ , the helicity reference system (HF) is used to describe the angular distribution. This frame is constructed by boosting from the Gottfried-Jackson system into the  $\xi$  rest frame. The  $z_{\text{HF}}$  axis is taken along the original direction of the isobar and  $\hat{y}_{\text{HF}} \equiv \hat{z}_{\text{GJ}} \times \hat{z}_{\text{HF}}$ . The two pions are emitted back to back, so that the  $\xi^0 \rightarrow \pi^- \pi^+$  decay is described by the polar angle  $\vartheta_{\text{HF}}$  and the azimuthal angle  $\phi_{\text{HF}}$  of the negative pion.

For illustration, Fig. 9 shows the observed, i.e. acceptance-uncorrected angular distributions in the two reference systems for events around the  $\pi_2(1670)$  mass region. The main decay of this resonance is through the  $f_2(1270)$  isobar, which is a  $J^{PC} = 2^{++}$  state decaying into  $\pi^- \pi^+$  in a relative  $D$ -wave in the helicity reference frame. The  $f_2(1270)$  and the bachelor pion are emitted in a relative  $S$  or  $D$ -wave in the Gottfried-Jackson coordinate system. Note that the shown distribution is complicated by the fact that other decay modes of the  $\pi_2(1670)$  as well as decays of other  $3\pi$  resonances with different angular distributions interfere with the  $\pi_2(1670) \rightarrow f_2(1270) \pi^-$  decay.

## B. Parametrization of decay amplitudes

In the helicity formalism [26,27,31], the amplitude  $\mathcal{A}_M^R$  for a two-body decay of a state  $R$  with spin  $J$  into particles 1 and 2 can be factorized into a dynamic part  $f_{\lambda_1 \lambda_2}^J(m_R; m_1, m_2)$  that describes the mass dependence and an angular part. The latter is related to the rotation between the rest frame of the parent system  $R$ , in which its spin projection  $M$  is defined, and the helicity frame used to define the daughter spin states, which are given by the helicities  $\lambda_{1,2}$ . The rotation is described by the Wigner

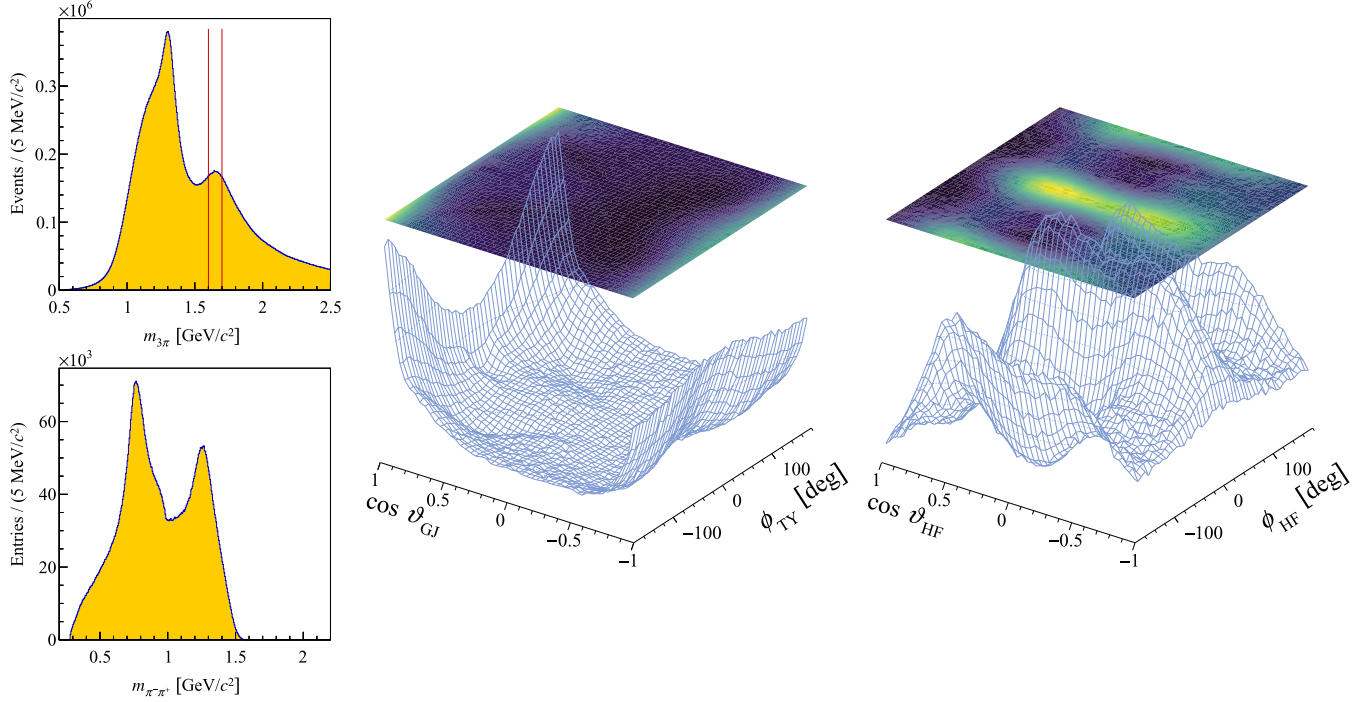


FIG. 9. Example of a  $3\pi$  angular distribution observed in the mass region  $1.6 < m_{3\pi} < 1.7$   $\text{GeV}/c^2$  around the  $\pi_2(1670)$  indicated by vertical red lines in the upper left panel. The main decay of this resonance is through the  $f_2(1270)$  isobar, which is a  $J^{PC} = 2^{++}$  state, decaying into  $\pi^-\pi^+$  in a  $D$ -wave. The  $f_2(1270)$  and the bachelor pion are in a relative  $S$  or  $D$ -wave.

$D$ -function. In addition, there are two Clebsch-Gordan coefficients arising in the decay  $R \rightarrow 1 + 2$ : (i) for the coupling of the spins  $J_{1,2}$  of the daughter particles to the total intrinsic spin  $S$  and (ii) for the coupling of the relative orbital angular momentum  $L_{12}$  between the daughter particles with  $S$  to  $J$ . As the orbital angular momentum  $L_{12}$  in the decay is by definition perpendicular to the quantization axis in the helicity formalism, its  $z$  projection vanishes.

The amplitude  $\mathcal{A}_\lambda^\xi$  for the two-body decay of the isobar  $\xi$  with spin  $J_\xi$  and helicity  $\lambda$  into  $\pi^-\pi^+$  is given by

$$\mathcal{A}_\lambda^\xi(\vartheta_{\text{HF}}, \phi_{\text{HF}}, m_\xi) = D_{\lambda 0}^{J_\xi^*}(\phi_{\text{HF}}, \vartheta_{\text{HF}}, 0) f_{00}^{J_\xi}(m_\xi; m_\pi, m_\pi), \quad (7)$$

with  $m_\xi$  being the  $\pi^-\pi^+$  invariant mass. The dynamic part factorizes into several components:

$$f_{00}^{J_\xi}(m_\xi; m_\pi, m_\pi) = \underbrace{\sqrt{2J_\xi + 1}}_{\text{normalization}} \underbrace{\alpha_\xi F_{J_\xi}(m_\xi; m_\pi, m_\pi) \Delta_\xi(m_\xi; m_\pi, m_\pi)}_{\text{dynamics}}. \quad (8)$$

Here, the fact was already used that pions are spinless isospin-1 particles. Therefore, the  $L$ - $S$  coupling Clebsch-Gordan coefficient is unity and the orbital angular momentum  $L_\xi$  in the decay is identical to the spin  $J_\xi$  of the isobar. The coupling amplitude  $\alpha_\xi$  describes the strength of the

decay and is usually unknown. Parametrizations for the barrier factor  $F_{J_\xi}$  and the isobar line shape  $\Delta_\xi$  are discussed in Sec. IV A.

The amplitude  $\mathcal{A}_M^X$  for the two-body decay of  $X^-$  into the isobar  $\xi$  and the bachelor pion is constructed by summing over the helicity  $\lambda$  of the intermediate isobar:

$$\mathcal{A}_M^X(\vartheta_{\text{GJ}}, \phi_{\text{TY}}, m_{3\pi}) = \sum_\lambda D_{M\lambda}^{J_X^*}(\phi_{\text{TY}}, \vartheta_{\text{GJ}}, 0) f_{\lambda 0}^J(m_{3\pi}; m_\xi, m_\pi). \quad (9)$$

Taking into account the quantum numbers of the bachelor pion the dynamic part of the amplitude reads:

$$f_{\lambda 0}^J(m_{3\pi}; m_\xi, m_\pi) = \underbrace{\sqrt{2L + 1}}_{\text{normalization}} \underbrace{(L 0 J_\xi \lambda | J \lambda)}_{\substack{L\text{-}S \text{ coupling} \\ \text{Clebsch-Gordan}}} \underbrace{\alpha_X F_L(m_{3\pi}; m_\xi, m_\pi)}_{\text{dynamics}}. \quad (10)$$

This is the nonrelativistic  $L$ - $S$  coupling scheme as introduced by Jacob and Wick in Ref. [26], which is equivalent to the nonrelativistic Zemach tensors [38,39]. Relativistic corrections as worked out in Ref. [40] are not applied. The results presented here are therefore comparable to those of previous analyses. The relativistic corrections are expected to become important for large breakup momenta in the  $X^- \rightarrow \xi^0 + \pi^-$  decay and will be studied in detail in a future analysis.

In Eq. (10), again an unknown coupling amplitude  $\alpha_X$  appears. Note that the line shape  $\Delta_X(m_{3\pi})$  of the  $X^-$  is unknown. It is actually the goal of the analysis to extract it from the data. This is achieved by setting  $\Delta_X$  to unity so that it does not appear in the above formula and by performing the analysis in narrow bins of  $m_{3\pi}$ , thereby neglecting the  $m_{3\pi}$  dependence within each bin.

Combining Eqs. (7) and (9) yields the  $X^-$  decay amplitude

$$\begin{aligned} & \psi_{i,j}(\overbrace{\vartheta_{\text{HF}}, \phi_{\text{HF}}, m_\xi, \vartheta_{\text{GJ}}, \phi_{\text{TY}}; m_{3\pi}} \equiv \tau) \\ &= \sum_\lambda D_{M\lambda}^{J*}(\phi_{\text{TY}}, \vartheta_{\text{GJ}}, 0) f_{\lambda 0}^J(m_{3\pi}; m_\xi, m_\pi) \\ & \times \mathcal{A}_\lambda^\xi(\vartheta_{\text{HF}}, \phi_{\text{HF}}, m_\xi). \end{aligned} \quad (11)$$

However, the above amplitude does not yet have the correct Bose symmetry under exchange of the two indistinguishable  $\pi^-$  in the final state. The symmetrized amplitude is

$$\tilde{\Psi}_{i,j}(\tau_{13}, \tau_{23}; m_{3\pi}) = \frac{1}{\sqrt{2}} [\psi_{i,j}(\tau_{13}; m_{3\pi}) + \psi_{i,j}(\tau_{23}; m_{3\pi})] \quad (12)$$

where  $\tau_{13}$  and  $\tau_{23}$  are the sets of phase-space variables calculated for the two possible  $\pi^-\pi^+$  combinations of the  $\pi_1^-\pi_2^-\pi_3^+$  system. Equation (12) takes correctly into account the self-interference due to the particle-exchange symmetry. For better readability, we will use the simplified notation  $\tilde{\Psi}_{i,j}(\tau; m_{3\pi})$  in the text below.

The  $X^-$  decay amplitude  $\tilde{\Psi}_{i,j}$  is uniquely defined by two indices: (a) the set of  $X^-$  quantum numbers (isospin  $I$ ,  $G$  parity, spin  $J$ , parity  $P$ ,  $C$  parity, and the spin projection  $M$ ), represented here by the index  $i \equiv (I^G, J^{PC}, M)$ , and (b) by the  $X^-$  decay mode enumerated by  $j \equiv (\xi, L)$ . In this way we can describe the decay of a diffractively produced intermediate state  $X^-$  with mass  $m_{3\pi}$  decaying into a  $\pi^-\pi^+$  isobar  $\xi$  and a bachelor  $\pi^-$ .

### C. Partial-wave decomposition

The intensity distribution  $\mathcal{I}(m_{3\pi}, t', \tau)$  of the final-state particles is written as a truncated series of partial waves denoted by the indices  $i$  and  $j$ , which represent certain quantum number combinations as discussed in Sec. III B. The strengths and phases, with which the different intermediate states  $X^-$  are produced, are described by the production amplitudes  $\tilde{T}_i^{re}(m_{3\pi}, t')$ . They depend on the production kinematics and on the set  $i = (I^G, J^{PC}, M)$  of the  $X^-$  quantum numbers. Together with the decay amplitudes from Eq. (12), the intensity is written as the coherent sum over the different intermediate  $X^-$  states represented by  $i$  and the different  $X^-$  decay modes enumerated by  $j$ :

$$\mathcal{I}(\tau; m_{3\pi}, t') = \sum_{\varepsilon=\pm 1} \sum_{r=1}^{N_r^\varepsilon} \left| \sum_i \tilde{T}_i^{re}(m_{3\pi}, t') \sum_j \tilde{\Psi}_{i,j}^\varepsilon(\tau; m_{3\pi}) \right|^2. \quad (13)$$

In the above formula, two additional indices, the so-called reflectivity  $\varepsilon$  and the rank index  $r$ , are introduced, which are both summed over incoherently. Before discussing these two indices, we transform Eq. (13) further.

In the helicity formalism, the isobar-model decay amplitudes are calculable up to the unknown couplings  $\alpha_\xi$  and  $\alpha_X$ , which appear at each decay vertex and were introduced in Sec. III B [see Eqs. (8), (10), and Fig. 7]. Assuming that these couplings do not depend on the kinematics, these unknowns can be pulled out of the decay amplitude in Eq. (12) and absorbed into the production amplitudes by the following redefinitions:

$$\tilde{\Psi}_{i,j}^\varepsilon(\tau; m_{3\pi}) \equiv \frac{\tilde{\Psi}_{i,j}^\varepsilon(\tau; m_{3\pi})}{\alpha_\xi \alpha_X} \quad (14)$$

and

$$\tilde{T}_{i,j}^{re}(m_{3\pi}, t') \equiv \alpha_\xi \alpha_X \tilde{T}_i^{re}(m_{3\pi}, t'). \quad (15)$$

Note that now the amplitudes  $\tilde{T}_{i,j}^{re}$  carry not only information about the production of the state  $i$ , but also about its coupling to a certain decay channel  $j$ . Therefore, we will refer to the  $\tilde{T}_{i,j}^{re}$  as *transition amplitudes* in the rest of the text. We introduce the index

$$a \equiv (i, j). \quad (16)$$

This notation represents a certain partial wave and contains all information about the production as well as the decay (see Sec. III B). With these modifications, we rewrite the expression for the intensity:

$$\mathcal{I}(\tau; m_{3\pi}, t') = \sum_{\varepsilon=\pm 1} \sum_{r=1}^{N_r^\varepsilon} \left| \sum_a \tilde{T}_a^{re}(m_{3\pi}, t') \tilde{\Psi}_a^\varepsilon(\tau; m_{3\pi}) \right|^2. \quad (17)$$

It is convenient to introduce the *spin-density matrix*

$$\tilde{\varrho}_{ab}^\varepsilon(m_{3\pi}, t') = \sum_{r=1}^{N_r^\varepsilon} \tilde{T}_a^{re} \tilde{T}_b^{re*}, \quad (18)$$

which represents the full information that is obtainable about  $X^-$ . The diagonal elements of  $\tilde{\varrho}$  are proportional to the partial-wave intensities and the off-diagonal entries to the interference terms.

There are several effects that could lead to deviations from full coherence of the intermediate states, e.g. spin-flip

and spin-nonflip processes or the excitation of baryon resonances. Also, performing the analysis over a large range of four-momentum transfer without taking into account the different  $t'$  dependences of the intermediate states may appear like incoherence (see Sec. V). One way of including these incoherences is the introduction of the additional rank index  $r$  for the transition amplitudes, which is summed over incoherently [see Eq. (17)]. The parameter  $N_r$  is called the *rank* of the spin-density matrix.

The constraints due to parity conservation in the production process are directly taken into account by working in the so-called *reflectivity basis*, where positive and negative values for the spin projection  $M$  are combined to yield amplitudes characterized by  $M \geq 0$  and an additional quantum number  $\varepsilon = \pm 1$ , called reflectivity. This is achieved by replacing the  $D$ -function in the  $X^- \rightarrow \xi^0 + \pi^-$  two-body decay amplitude of Eq. (9) by

$$\begin{aligned} {}^\varepsilon D_{M\lambda}^J(\phi_{\text{TY}}, \vartheta_{\text{GJ}}, 0) &\equiv c(M)[D_{(+M)\lambda}^J(\phi_{\text{TY}}, \vartheta_{\text{GJ}}, 0) \\ &\quad - \varepsilon P(-)^{J-M} D_{(-M)\lambda}^J(\phi_{\text{TY}}, \vartheta_{\text{GJ}}, 0)], \end{aligned} \quad (19)$$

with  $\varepsilon = \pm 1$ ,  $M \geq 0$ , and the normalization factor

$$c(M) = \begin{cases} 1/2 & \text{for } M = 0, \\ 1/\sqrt{2} & \text{otherwise.} \end{cases} \quad (20)$$

The reflectivity is the eigenvalue of reflection through the  $X$  production plane. In the high-energy limit,  $\varepsilon$  corresponds to the naturality of the exchange in the scattering process, such that  $\varepsilon = +1$  ( $-1$ ) corresponds to natural spin-parity of the exchanged Reggeon, i.e.  $J^P = 1^-$  or  $2^+$  or  $3^- \dots$  (unnatural spin-parity:  $J^P = 0^-$  or  $1^+$  or  $2^- \dots$ ) transfer to the beam particle. Expressing the amplitudes in the reflectivity basis brings the spin-density matrix into a block-diagonal form with respect to  $\varepsilon$  [29]. Hence states with different reflectivities, i.e. those produced by Regge-trajectories with different naturalities, do not interfere and are thus summed up incoherently [see Eq. (17)]. In general, the rank  $N_r$  of the spin-density matrix may be different in the two reflectivity sectors, i.e.  $N_r^\varepsilon$ .

Finally, we introduce the phase-space-normalized decay amplitudes  $\Psi_a^\varepsilon(\tau; m_{3\pi})$  as

$$\Psi_a^\varepsilon(\tau; m_{3\pi}) \equiv \frac{\bar{\Psi}_a^\varepsilon(\tau; m_{3\pi})}{\sqrt{\int d\varphi_3(\tau') |\bar{\Psi}_a^\varepsilon(\tau'; m_{3\pi})|^2}}, \quad (21)$$

where  $d\varphi_3(\tau')$  is the differential three-body phase-space element. This normalizes the transition amplitudes via

$$\mathcal{T}_a^{r\varepsilon}(m_{3\pi}, t') \equiv \bar{\mathcal{T}}_a^{r\varepsilon}(m_{3\pi}, t') \sqrt{\int d\varphi_3(\tau') |\bar{\Psi}_a^\varepsilon(\tau'; m_{3\pi})|^2} \quad (22)$$

with

$$\mathcal{Q}_{ab}^\varepsilon(m_{3\pi}, t') = \sum_{r=1}^{N_r^\varepsilon} \mathcal{T}_a^{r\varepsilon} \mathcal{T}_b^{r\varepsilon*}, \quad (23)$$

such that the partial-wave intensities, which are the diagonal elements of the spin-density matrix in Eq. (22), are given in terms of number of events that would be observed in a perfect detector.

The goal of the partial-wave analysis is to extract the unknown transition amplitudes  $\mathcal{T}_a^{r\varepsilon}(m_{3\pi}, t')$  from the data, because they contain information about the intermediate  $3\pi$  resonances. Since the mass dependence of the transition amplitudes is unknown, the event sample is divided into  $m_{3\pi}$  bins much narrower than the width of typical hadronic resonances. Within each mass bin, the  $m_{3\pi}$  dependence is assumed to be negligible, so that the  $\mathcal{T}_a^{r\varepsilon}$  only depend on  $t'$ .

Also the  $t'$  dependence of the transition amplitudes is *a priori* unknown. In previous analyses it was often assumed that the  $m_{3\pi}$  and  $t'$  dependences factorize and the  $t'$  dependence was modeled by real functions  $g_a^\varepsilon(t')$ . These functions were extracted from the analyzed data set by integrating over wide  $m_{3\pi}$  ranges, often only for groups of waves. The COMPASS data, however, exhibit a complicated and significant correlation of the  $t'$  and  $m_{3\pi}$  dependences (see Sec. V), which renders this approach inapplicable. As it will be shown in Sec. IV C, this is mainly due to different production processes (resonance production and nonresonant processes, like e.g. the Deck process [25]), which contribute with amplitudes that may have very different dependences on  $t'$ . Therefore, the partial-wave decomposition is performed for each  $m_{3\pi}$  bin independently in different slices of  $t'$  (see Sec. IV B and Table IV). Within a  $t'$  bin, the transition amplitude is assumed to be independent of  $t'$ . Taking out the explicit assumptions about the  $t'$  dependences by virtue of our large data set is an advantage compared to most previous analyses (e.g. [8]).

For a given bin in  $m_{3\pi}$  and  $t'$ , the intensity has thus a simpler form as it depends only on the five phase-space variables  $\tau$ :

$$\mathcal{I}(\tau) = \sum_{\varepsilon=\pm 1} \sum_{r=1}^{N_r^\varepsilon} \left| \sum_a \mathcal{T}_a^{r\varepsilon} \Psi_a^\varepsilon(\tau) \right|^2 + \mathcal{I}_{\text{flat}}, \quad (24)$$

with the transition amplitudes appearing as constants. Here, we introduced an additional incoherently added wave that is isotropic in  $\tau$  and from now on is referred to as *flat wave*. The purpose of this wave is to absorb intensity of events with three uncorrelated pions in the final state, e.g.

nonexclusive background. The flat wave is always part of the wave set, even if not mentioned explicitly.

#### D. Maximum-likelihood method

The transition amplitudes  $T_a^{re}$  are determined for each bin in  $m_{3\pi}$  and  $t'$  by fitting the model intensity  $\mathcal{I}(\tau)$  of Eq. (24) to the measured  $\tau$  distribution. The fit is based on an extended likelihood function constructed from the probabilities to observe the  $N$  measured events with phase-space coordinates  $\tau_i$ :

$$\mathcal{L} = \underbrace{\frac{\bar{N}^N}{N!} e^{-\bar{N}}}_{\text{Poisson probability}} \prod_{i=1}^N \underbrace{\frac{\mathcal{I}(\tau_i)}{\int d\varphi_3(\tau) \eta(\tau) \mathcal{I}(\tau)}}_{\text{Probability for event } i}. \quad (25)$$

Here,  $\eta(\tau)$  is the detection efficiency and  $d\varphi_3(\tau)$  the differential three-body phase-space element. The expected number of events  $\bar{N}$  in the detector is given by the normalization integral

$$\bar{N} = \int d\varphi_3(\tau) \eta(\tau) \mathcal{I}(\tau). \quad (26)$$

By this integral, the detection efficiency is taken into account in the fit model, thereby avoiding the binning of the data, which would be impractical given the high dimensionality of the intensity distribution.

Inserting Eq. (26) into Eq. (25) and dropping all constant terms as well as taking the logarithm, the expression reads

$$\begin{aligned} \ln \mathcal{L} = & \sum_{i=1}^N \ln \left[ \sum_{\epsilon=\pm 1} \sum_{r=1}^{N_r^\epsilon} \left| \sum_a T_a^{re} \Psi_a^\epsilon(\tau_i) \right|^2 + \mathcal{I}_{\text{flat}} \right] \\ & - \sum_{\epsilon=\pm 1} \sum_{r=1}^{N_r^\epsilon} \sum_{a,b} T_a^{re} T_b^{re*} \underbrace{\int d\varphi_3(\tau) \eta(\tau) \Psi_a^\epsilon(\tau) \Psi_b^{\epsilon*}(\tau)}_{\equiv I_{ab}^\epsilon} \\ & - \underbrace{\mathcal{I}_{\text{flat}} \int d\varphi_3(\tau) \eta(\tau)}_{\equiv I_{\text{flat}}} \end{aligned} \quad (27)$$

Here, the complex-valued integral matrix  $I_{ab}^\epsilon$ , which is independent of the transition amplitudes, is calculated using Monte Carlo methods. The same is true for the real-valued integral  $I_{\text{flat}}$  for the isotropic flat wave.

In every individual  $(m_{3\pi}, t')$  bin, the transition amplitudes  $T_a^{re}$  are determined by maximizing the likelihood function of Eq. (27), which allows the determination of the spin-density matrix elements

$$Q_{ab}^\epsilon = \sum_{r=1}^{N_r^\epsilon} T_a^{re} T_b^{re*}. \quad (28)$$

Setting the detection efficiency  $\eta(\tau) = 1$  in Eq. (26) gives the expected acceptance-corrected number of events:

$$\begin{aligned} N_{\text{corr}} &= \int d\varphi_3(\tau) \mathcal{I}(\tau) \\ &= \sum_{\epsilon=\pm 1} \sum_{a,b} Q_{ab}^\epsilon \int d\varphi_3(\tau) \Psi_a^\epsilon(\tau) \Psi_b^{\epsilon*}(\tau) \\ &\quad + \mathcal{I}_{\text{flat}} \int d\varphi_3(\tau). \end{aligned} \quad (29)$$

Using the fact that the decay amplitudes  $\Psi_a^\epsilon(\tau)$  are normalized via Eq. (21) and that  $Q_{ab}^\epsilon$  is Hermitian, the expression can be rewritten as

$$\begin{aligned} N_{\text{corr}} &= \sum_{\epsilon=\pm 1} \left\{ \sum_a \underbrace{Q_{aa}^\epsilon}_{\text{Intensities}} \right. \\ &\quad \left. + \sum_{a<b} \underbrace{2\text{Re}[Q_{ab}^\epsilon \int d\varphi_3(\tau) \Psi_a^\epsilon(\tau) \Psi_b^{\epsilon*}(\tau)]}_{\text{Overlaps}} \right\} \\ &\quad + \mathcal{I}_{\text{flat}} \int d\varphi_3(\tau). \end{aligned} \quad (30)$$

From this equation, the interpretation of the spin-density matrix elements becomes obvious. The diagonal elements  $Q_{aa}^\epsilon$  are the *partial wave intensities*, i.e. the expected acceptance-corrected number of events in wave  $a$ . The *overlaps* are the respective number of events that exhibit interference between waves  $a$  and  $b$ . Limiting the summation in Eq. (30) to a subset of partial waves yields the expected acceptance-corrected number of events in these waves including all interferences. Such sums will be denoted as *coherent sums* of partial waves in the following text.

The procedure described in this section is referred to as *mass-independent* fit. It is worth stressing that fits in different kinematic bins are independent of each other. The fit model of Eq. (24) does not contain any assumptions about possible  $3\pi$  resonances. They will be extracted in a second analysis step from the  $m_{3\pi}$  dependence of the spin-density matrix. This so-called *mass-dependent* fit will be described in a forthcoming paper [33].

#### IV. PARTIAL-WAVE DECOMPOSITION IN BINS OF $m_{3\pi}$ AND $t'$

In principle, the partial-wave expansion in Eq. (24) includes an infinite number of waves. In practice, the expansion series has to be truncated. This means that one has to define a *wave set* that describes the data sufficiently well, without introducing too many free parameters.

Since the intermediate state  $X^-$  decays into a system of three charged pions, the  $G$  parity of  $X^-$  is  $-1$  and the isospin  $I = 1$ , ignoring flavor-exotic states with  $I > 1$ . The number of possible partial waves is largely determined by the maximum allowed spin  $J$  of  $X^-$ , the maximum allowed orbital angular momentum  $L$  in the decay of the  $X^-$  to the

TABLE III. Overview of the isobar parametrizations used in the partial-wave analysis.

Isobar	Formula	Parameters
$[\pi\pi]_S$	$M$ solution from Ref. [41] (see Fig. 10)	see text and Table 1 in Ref. [41]
$\rho(770)$	Eq. (31) with Eq. (40)	$m_0 = 768.5 \text{ MeV}/c^2$ , $\Gamma_0 = 150.7 \text{ MeV}/c^2$
$f_0(980)$	Eq. (43) (see Ref. [42])	$m_0 = 965 \text{ MeV}/c^2$ , $g_{\pi\pi} = 0.165 (\text{GeV}/c^2)^2$ , $g_{K\bar{K}}/g_{\pi\pi} = 4.21$
$f_2(1270)$	Eq. (31) with Eq. (32)	$m_0 = 1275.4 \text{ MeV}/c^2$ , $\Gamma_0 = 185.2 \text{ MeV}/c^2$
$f_0(1500)$	Eq. (31) with Eq. (42)	$m_0 = 1507 \text{ MeV}/c^2$ , $\Gamma_0 = 109 \text{ MeV}/c^2$
$\rho_3(1690)$	Eq. (41)	$m_0 = 1690 \text{ MeV}/c^2$ , $\Gamma_0 = 190 \text{ MeV}/c^2$

isobar and the bachelor  $\pi^-$ , and the choice of the isobars. Since there are no known resonances in the flavor-exotic  $\pi^-\pi^-$  channel, we choose to include only  $\pi^-\pi^+$  isobars. We include  $[\pi\pi]_S$ ,  $\rho(770)$ ,  $f_0(980)$ ,  $f_2(1270)$ ,  $f_0(1500)$ , and  $\rho_3(1690)$  as isobars into the fit model. This selection is based on the features observed in the  $\pi^-\pi^+$  invariant mass spectrum in Figs. 5(b) and 6 and on findings of previous experiments [17–20,22].

### A. Isobar parametrization

In this section, we present the parametrizations of the mass-dependent amplitudes of the six isobars chosen above, which enter the analysis via Eqs. (7), (9), and (11) and are summarized in Table III.

In most cases, the  $\pi^-\pi^+$  isobar resonances are described using a relativistic Breit-Wigner amplitude [43]

$$\Delta_{\text{BW}}(m; m_0, \Gamma_0) = \frac{m_0 \Gamma_0}{m_0^2 - m^2 - im_0 \Gamma(m)}, \quad (31)$$

where  $m_0$  and  $\Gamma_0$  are mass and width of the resonance. For a single two-body decay channel, the mass-dependent width  $\Gamma(m)$  is given by

$$\Gamma(m) = \Gamma_0 \frac{m_0}{m} \frac{q}{q_0} \frac{F_\ell^2(q)}{F_\ell^2(q_0)}. \quad (32)$$

By applying Eq. (32), we assume that the isobar decays predominantly into two pions and neglect other decay modes. Here,  $q(m)$  is the momentum of  $\pi^-$  and  $\pi^+$  in the rest frame of the isobar with mass  $m$ . At the nominal resonance mass, the breakup momentum is given by  $q_0 = q(m_0)$ . By  $F_\ell(q)$  we denote the Blatt-Weisskopf barrier factors [44], which appear also in Eq. (8) and take into account the centrifugal-barrier effect caused by the orbital angular momentum  $\ell$  in the isobar decay.<sup>4</sup> We use the parametrization of von Hippel and Quigg [45], where

$$F_0^2(q) = 1, \quad (33)$$

$$F_1^2(q) = \frac{2z}{z+1}, \quad (34)$$

$$F_2^2(q) = \frac{13z^2}{z^2 + 3z + 9}, \quad (35)$$

$$F_3^2(q) = \frac{277z^3}{z^3 + 6z^2 + 45z + 225}, \quad (36)$$

$$F_4^2(q) = \frac{12746z^4}{z^4 + 10z^3 + 135z^2 + 1575z + 11025}, \quad (37)$$

$$F_5^2(q) = \frac{998881z^5}{z^5 + 15z^4 + 315z^3 + 6300z^2 + 99225z + 893025}, \quad \text{and} \quad (38)$$

$$F_6^2(q) = \frac{118394977z^6}{z^6 + 21z^5 + 630z^4 + 18900z^3 + 496125z^2 + 9823275z + 108056025}. \quad (39)$$

Here,  $z \equiv (q/q_R)^2$  with the range parameter  $q_R = 202.4 \text{ MeV}/c$  that corresponds to an assumed strong interaction range of 1 fm.<sup>5</sup> For small breakup momenta  $q \approx 0$ , the amplitude behaves like  $F_\ell(q) \propto q^\ell$ .

The description of the  $\rho(770)$  isobar is slightly improved by modifying Eq. (32) as shown in Refs. [46,47]:

$$\Gamma(m) = \Gamma_0 \frac{q}{q_0} \frac{F_\ell^2(q)}{F_\ell^2(q_0)}. \quad (40)$$

<sup>4</sup>For the decay of the isobar into two spinless particles,  $\ell$  is given by the spin  $J_\xi$  of the isobar.

<sup>5</sup>Instead of the original normalization of the barrier factors such that  $F_\ell(q) \rightarrow 1$  for  $q \rightarrow \infty$ , von Hippel and Quigg modified the normalization in a way that  $F_\ell(q) = 1$  for  $z = 1$ .

For the  $\rho_3(1690)$  isobar, a slightly modified Breit-Wigner amplitude is used:

$$\Delta_{\rho_3(1690)}(m; m_0, \Gamma_0) = \frac{\sqrt{mm_0}\Gamma_0}{m_0^2 - m^2 - im_0\Gamma_0}. \quad (41)$$

Since the  $\pi^-\pi^+$  decay mode of the  $\rho_3(1690)$  is not dominant, a constant total width is used.

The most difficult sector is that of the scalar isobars with  $J^{PC} = 0^{++}$ , which consists of several overlapping  $f_0$  resonances. In this analysis, we consider three independent isobar amplitudes that have quite different properties. A broad component with slow phase motion, which we denote by  $[\pi\pi]_S$ , dominates the mass spectrum from low to intermediate two-pion masses. This component interferes with the narrow  $f_0(980)$ . In elastic  $\pi\pi$  scattering, this interference is destructive, so that the  $f_0(980)$  appears as a pronounced dip. However, in  $\pi^-\pi^-\pi^+$  decays, the  $\pi\pi$  S-wave subsystem behaves differently. As will be shown in Sec. VI, the relative phase between the two components depends on the quantum numbers of the  $3\pi$  intermediate state and on its mass. In order to give the model the freedom to adjust the couplings of the various  $3\pi$  states to the  $[\pi\pi]_S\pi$  and  $f_0(980)\pi$  decay modes separately, the broad  $\pi\pi$  S-wave component and the  $f_0(980)$  are treated as independent isobars. Similarly, the  $f_0(1500)$  is included using a Breit-Wigner amplitude [see Eq. (31)] with constant width

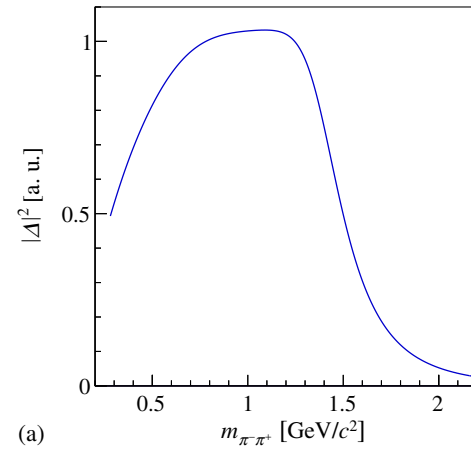
$$\Gamma(m) = \Gamma_0. \quad (42)$$

The Breit-Wigner amplitude is not able to describe the  $f_0(980)$  well as it peaks close to the  $K\bar{K}$  threshold. Therefore, this isobar is described by a Flatté parametrization [48] that takes into account the coupling to the  $\pi\pi$  and  $K\bar{K}$  decay channels:

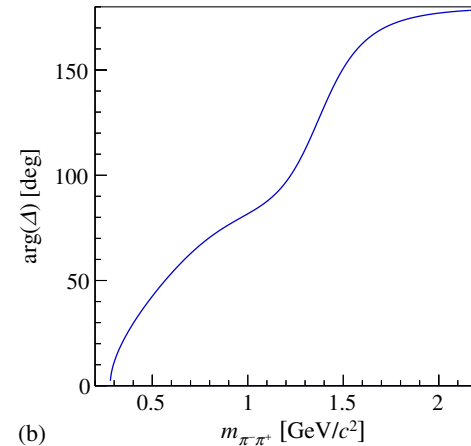
$$\Delta_{\text{Flatté}}(m; m_0, g_{\pi\pi}, g_{K\bar{K}}) = \frac{1}{m_0^2 - m^2 - i(\varphi_2^{\pi\pi} g_{\pi\pi} + \varphi_2^{K\bar{K}} g_{K\bar{K}})}. \quad (43)$$

Here,  $\varphi_2^i = 2q_i/m$  is the two-body phase space for the two decay channels  $i = \pi\pi, K\bar{K}$  with the respective breakup momenta  $q_i(m)$ , which become complex-valued below threshold. The values for the couplings  $g_{\pi\pi}$  and  $g_{K\bar{K}}$  as well as that for the mass  $m_0$  are given in Table III as determined by the BES experiment from a partial-wave analysis of  $J/\psi$  decays into  $\phi\pi^-\pi^+$  and  $\phi K^-K^+$  [42].

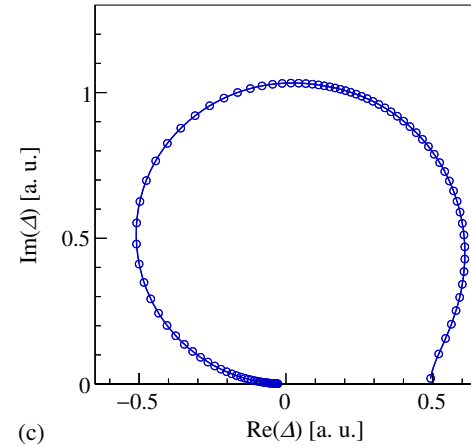
The parametrization of the broad  $\pi\pi$  S-wave component is the most complicated one. It is based on the parametrization of the  $\pi\pi$  S-wave from Ref. [41], which was extracted from  $\pi\pi$  elastic scattering data. We modify the so-called  $M$  solution (see Table 1 in Ref. [41]) as suggested by the VES collaboration [49]. In order to remove the  $f_0(980)$  from the amplitude, the parameters  $f_1^1, f_2^1, f_3^1, c_{11}^4$ , and  $c_{22}^4$  as well as the diagonal elements of the  $M$  matrix in



(a)



(b)



(c)

FIG. 10. Parametrization of the  $[\pi\pi]_S$  isobar amplitude based on the  $M$  solution described in Ref. [41]. Panel (a) shows the intensity, (b) the phase, and (c) the corresponding Argand diagram. The open circles in the latter are evenly spaced in  $m_{\pi^-\pi^+}$  in 20 MeV/ $c^2$  intervals. Arbitrary units are denoted by “a. u.”.

Eq. (3.20) of Ref. [41] are set to zero. Figure 10 shows the resulting  $[\pi\pi]_S$  amplitude ( $\mathcal{T}_{11}$  of Eq. (3.15) in Ref. [41]). It has a broad intensity distribution that extends to two-pion masses of about 1.5 GeV/ $c^2$  accompanied by a slow phase motion.

TABLE IV. Borders of the eleven nonequidistant  $t'$  bins, in which the partial-wave analysis is performed (see Fig. 11). The intervals are chosen such that each bin contains approximately  $4.6 \times 10^6$  events. Only the last range from 0.449 to 1.000  $(\text{GeV}/c)^2$  is subdivided further into two bins.

Bin	1	2	3	4	5	6
$t'[(\text{GeV}/c)^2]$	0.100	0.113	0.127	0.144	0.164	0.189
Bin	7	8	9	10	11	
$t'[(\text{GeV}/c)^2]$	0.220	0.262	0.326	0.449	0.724	1.000

### B. Fit model

When using the isobar model, we have in principle to take into account all observed  $\pi^-\pi^+$  correlations. In accordance with the  $\pi^-\pi^+$  invariant mass spectrum shown in Fig. 5(b) and with analyses by previous experiments, we include  $[\pi\pi]_S$ ,  $\rho(770)$ ,  $f_0(980)$ ,  $f_2(1270)$ ,  $f_0(1500)$ , and  $\rho_3(1690)$  as isobars into the fit model. Based on these six isobars, we have constructed a set of partial waves that consists of 88 waves in total, i.e. 80 waves with reflectivity  $\varepsilon = +1$ , seven waves with  $\varepsilon = -1$ , and one noninterfering flat wave representing three uncorrelated pions. This wave set has been derived from a larger set of 128 waves, which includes mainly positive-reflectivity partial waves with spin  $J \leq 6$ , orbital angular momentum  $L \leq 6$ , and spin projection  $M = 0, 1, \text{ and } 2$ . Omission of structureless waves with relative intensities below approximately  $10^{-3}$  yields the 88 partial waves that are used in this analysis and given in Table IX in Appendix A.

The wave set includes waves with spin-exotic  $J^{PC} = 1^{-+}$  and  $3^{-+}$ . These waves have intensities significantly different from zero. They contribute 1.8% and 0.1%, respectively, to the observed intensity. Removing the three  $1^{-+}$  waves from the fit model<sup>6</sup> decreases the log-likelihood value, summed over the 11  $t'$  bins, by more than 4000 units in the  $3\pi$  mass range from 1.1 to 1.7  $\text{GeV}/c^2$ . If instead the two  $3^{-+}$  waves are removed,<sup>7</sup> the log-likelihood value, summed over the 11  $t'$  bins, decreases by 200 units in the  $3\pi$  mass range from 1.1 to 1.7  $\text{GeV}/c^2$ . The spin-exotic waves will not be discussed any further in this paper.

In the construction of the wave set, problems may arise when more than one isobar with the same  $J^{PC}$  quantum numbers and a broad overlap of their mass functions are used simultaneously, causing considerable overlap between the corresponding decay amplitudes. Such cases have to be treated with great care as the fit tends to become unstable. In our fit model, this applies to the  $0^{++}$  isobars. Here, the broad  $[\pi\pi]_S$ , the narrow  $f_0(980)$ , and the  $f_0(1500)$  do have considerable overlap. Because of the narrowness of the  $f_0(980)$ , the fit is able to separate it well from the broad

$[\pi\pi]_S$ , as it is demonstrated in Sec. VI. In contrast, the inclusion of several waves with  $f_0(1500)$   $\pi$  decay modes tends to destabilize the fit. Therefore, the 88-wave model includes only one  $f_0(1500)$   $\pi$  wave. We decided to include the  $0^{-+}0^+ f_0(1500)\pi S$  wave for  $m_{3\pi} > 1.7 \text{ GeV}/c^2$  in order to study a potential signal for the decay  $\pi(1800) \rightarrow f_0(1500) + \pi$ . The parametrizations used for the line shapes of the isobars are based on prior knowledge and were described in Sec. IV A. The effect of isobars with uncertain line shapes may lead to spurious results and is addressed by systematic studies discussed in Sec. IV F and Appendix B 3. We also apply an extended analysis method, which partly removes the model bias due to the isobar parametrizations. Results are presented in Sec. VI.

The likelihood function to be maximized in the fit with the production amplitudes as free parameters is built according to Eq. (27). Using such a large wave set to fit the three-pion system, we have to be concerned about stability of the results, which in turn may be influenced by correlations and cross talk of partial waves. In order to reduce such effects, different subsets of the 88 waves are used, which grow in size with increasing three-pion mass. High-spin waves and waves with heavy isobars are typically omitted from the wave set in the region of low  $m_{3\pi}$ . This has two reasons: first, the intensity of such waves is expected to vanish at low  $m_{3\pi}$ , and second, they would artificially contribute to ambiguities since the phase space at low masses appears to be too small to find a unique solution. A disadvantage of introducing the mass thresholds for particular waves are possible discontinuities induced in the mass dependence of other partial waves. Therefore, such thresholds have to be placed as low as possible. In our analysis, thresholds were applied to 27 of the 88 partial waves. The threshold values, which were carefully tuned in order to reduce artificial structures, are listed in Table IX in Appendix A.

The partial-wave analysis is performed independently in 100 equidistant  $m_{3\pi}$  bins with a width of 20  $\text{MeV}/c^2$ , each of which is subdivided into eleven nonequidistant  $t'$  bins (see Table IV). The  $t'$  bins are chosen such that, except for the two highest  $t'$  bins, each bin contains approximately the same number of events. Within each of these 1100 bins, the transition amplitudes  $\mathcal{T}_\alpha^{re}(m_{3\pi}, t')$  in Eq. (24) are assumed to be constant. Figure 11 illustrates the correlation of  $t'$  and

<sup>6</sup>This reduces the number of free parameters in the PWA fit by 6.

<sup>7</sup>This reduces the number of free parameters in the PWA fit by 4.

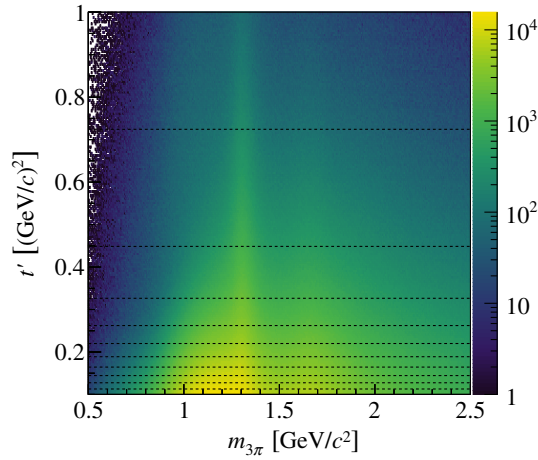


FIG. 11. Correlation of the reduced four-momentum transfer squared  $t'$  and the invariant mass  $m_{3\pi}$  of the  $3\pi$  system in the analyzed kinematic region. The partial-wave analysis is performed independently in 100 equidistant  $m_{3\pi}$  bins with a width of 20 MeV/ $c^2$ , each of which is subdivided into eleven nonequidistant  $t'$  bins. The latter are indicated by the dashed horizontal lines. The numerical values for the  $t'$  bins are listed in Table IV.

$m_{3\pi}$ , where the subdivision into bins of  $t'$  is indicated by horizontal lines.

In the present analysis, we have limited ourselves to a rank-1 spin-density matrix for the waves in the

positive-reflectivity sector, which is dominated by Pomeron exchange (see also discussion in Sec. III C). The smallest rank,  $N_r^{(\epsilon=+1)} = 1$ , is sufficient mainly because the analysis is performed in narrow bins of  $t'$ , where the relative phases of the partial waves do not vary significantly. As part of the systematic studies, a fit with rank 2 was investigated, which shows enhanced artificial structures as well as increased instabilities (see Sec. IV F and Appendix B 1). For the negative-reflectivity waves, which can be produced by the exchange of various Reggeons [e.g.  $b_1(1235)$ ], we use  $N_r^{(\epsilon=-1)} = 2$ .

### C. Selected partial waves with spin projections $M=0, 1$ , and 2

In this section, we present the result of the fit in bins of  $m_{3\pi}$  and  $t'$  for 18 selected waves with positive reflectivity as listed in Table V. The waves are selected partly in view of the *mass-dependent* fit that will be described in a forthcoming paper, in which all resonance parameters determined by the fit will be presented [33]. This selection includes waves with spin projections  $M = 0, 1$ , and 2 that either have large intensities or exhibit clear signals of well-established resonances or even unexpected signals. In addition, we have selected large waves with  $[\pi\pi]_S$  and  $f_0(980)$  isobars, which are related to the detailed study of

TABLE V. Waves selected for presentation in this paper out of the much larger pool of 88 waves used in the *mass-independent* fit (see Table IX in Appendix A). The partial waves with  $[\pi\pi]_S$  and  $f_0(980)$  isobars at the bottom of the table will be discussed in Sec. VI. The intensities are evaluated as a sum over the 11  $t'$  bins and are normalized to the total number of acceptance-corrected events. They do not include interference effects between the waves.

$J^{PC}$	$M^\epsilon$	Isobaric decay	Relative intensity [%]	Shown in
$1^{++}$	$0^+$	$\rho(770)\pi S$	32.7	Figs. 14(a), 17(a), and 17(c)
$1^{++}$	$1^+$	$\rho(770)\pi S$	4.1	Fig. 15(a)
$1^{++}$	$0^+$	$f_2(1270)\pi P$	0.4	Figs. 16(b), 20(a), and 20(c)
$2^{++}$	$1^+$	$\rho(770)\pi D$	7.7	Figs. 15(b), 17(b), and 17(d)
$2^{++}$	$2^+$	$\rho(770)\pi D$	0.3	Fig. 16(a)
$2^{++}$	$1^+$	$f_2(1270)\pi P$	0.5	Figs. 15(c), 20(b), and 20(d)
$2^{-+}$	$0^+$	$\rho(770)\pi F$	2.2	Figs. 21(a), 21(c), and 22(d)
$2^{-+}$	$0^+$	$f_2(1270)\pi S$	6.7	Figs. 14(b), 18(a), 18(c), and 22(a)
$2^{-+}$	$1^+$	$f_2(1270)\pi S$	0.9	Figs. 15(d) and 22(c)
$2^{-+}$	$0^+$	$f_2(1270)\pi D$	0.9	Fig. 22(b)
$4^{++}$	$1^+$	$\rho(770)\pi G$	0.8	Figs. 15(e), 18(b), and 18(d)
$4^{++}$	$1^+$	$f_2(1270)\pi F$	0.2	Figs. 15(f), 21(b), and 21(d)
$0^{-+}$	$0^+$	$[\pi\pi]_S \pi S$	8.0	Figs. 24(a), 24(b), and 25(b)
$0^{-+}$	$0^+$	$f_0(980)\pi S$	2.4	Fig. 25(a)
$1^{++}$	$0^+$	$[\pi\pi]_S \pi P$	4.1	Fig. 25(f)
$1^{++}$	$0^+$	$f_0(980)\pi P$	0.3	Fig. 25(e)
$2^{-+}$	$0^+$	$[\pi\pi]_S \pi D$	3.0	Fig. 25(d)
$2^{-+}$	$0^+$	$f_0(980)\pi D$	0.6	Fig. 25(c)
Intensity Sum			75.8	

the  $\pi^-\pi^+$  subsystem with  $J^{PC} = 0^{++}$  presented in Sec. VI. The amplitudes of 17 out of the 18 selected waves are found to be practically insensitive to systematic effects arising from the remaining waves, in particular to the truncation of the partial-wave expansion series in Eq. (24) (see Sec. IV F and Appendix B). The intensity distributions of the remaining 69 waves are shown in the Supplemental Material [50].

The *total intensity* of all partial waves is defined as the total number of acceptance-corrected events as given by Eq. (30). The *relative intensity* of a given partial wave, as listed in Table V, is defined as the ratio of its intensity integral over the analyzed mass range to the integral of the total intensity. This value is in general different from the contribution of a wave to the total intensity, owing to interference effects between the waves. Therefore, the relative intensities of all 88 partial waves add up to 105.3% instead of 100%. However, self-interference due to Bose symmetrization is included via Eq. (12).

If not indicated otherwise, the wave intensities shown in the figures below are the sum of the intensities over the individual  $t'$  bins. They will be referred to as  $t'$ -summed intensities in the text that follows. The percent numbers given in the mass spectra are the relative intensities of the particular partial wave shown. In addition, we show for some waves the intensity distribution in individual  $t'$  bins. While mass and width of resonances do not depend on the production kinematics, coherent nonresonant contributions may vary in shape and phase with  $t'$ . This may lead to significant  $t'$ -dependent shifts of mass peaks. Examples of such effects are discussed below.

As shown in Fig. 12, waves with negative reflectivity, which correspond to unnatural-parity exchange processes, contribute only 2.2% to the total intensity. The dominance of natural-parity exchange processes is expected at COMPASS energies because the Pomeron contribution is considered to be dominant. Therefore, we are only taking into account positive-reflectivity partial waves in the following.

The incoherent isotropic flat wave turns out to contribute about 3.1% to the total observed intensity (see Fig. 13). This magnitude is roughly consistent with the background level that one expects from extrapolating the nonexclusive background component visible in Fig. 3 into the signal region.

Figure 14 shows the  $t'$ -summed intensities of two major waves with spin projection  $M = 0$ , i.e. the  $1^{++}0^+\rho(770)\pi S$  and  $2^{-+}0^+f_2(1270)\pi S$  waves. Both exhibit clear peaks corresponding to the  $a_1(1260)$  and the  $\pi_2(1670)$  resonances.

Selecting spin projection  $M = 1$ , we have access to the  $1^{++}1^+\rho(770)\pi S$ ,  $2^{++}1^+\rho(770)\pi D$ ,  $2^{++}1^+f_2(1270)\pi P$ ,  $2^{-+}1^+f_2(1270)\pi S$ , as well as to the  $4^{++}1^+\rho(770)\pi G$  and  $4^{++}1^+f_2(1270)\pi F$  waves, as shown in Fig. 15. The intensity maxima can be identified with the well-known

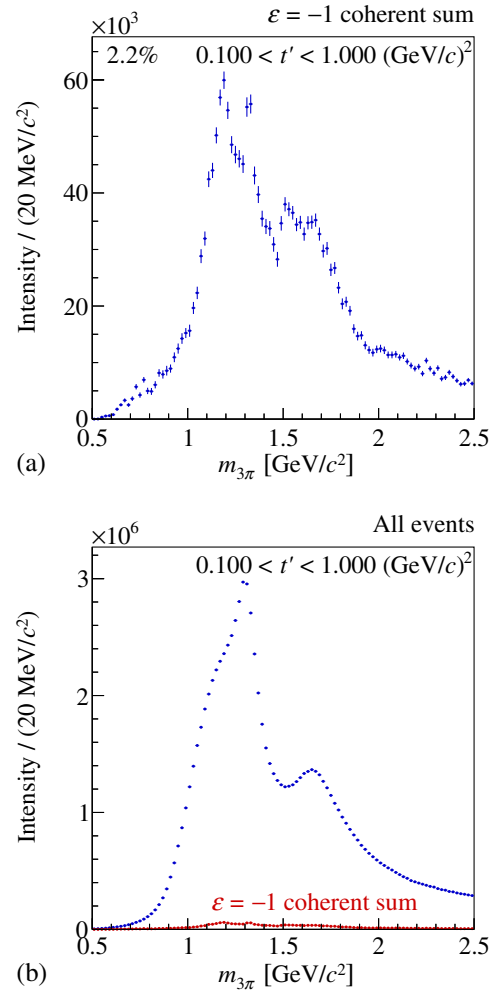


FIG. 12. The  $t'$ -summed intensity of the coherent sum of all negative-reflectivity waves (a) and, for comparison, together with the total intensity of all partial waves (b).

resonances  $a_1(1260)$ ,  $a_2(1320)$ ,  $\pi_2(1670)$ , and  $a_4(2040)$ . Comparing Figs. 15(a) and 15(d) to Figs. 14(a) and 14(b), respectively, a suppression of intensities for waves with  $M = 1$  by about one order of magnitude as compared to  $M = 0$  can clearly be observed.

Clear evidence is obtained for an  $M = 2$  component of the  $2^{++}\rho(770)\pi D$  wave [Fig. 16(a)]. Its relative intensity with respect to the  $M = 1$  wave [Fig. 15(b)] is about 5%. This is in good agreement with our result for the  $2^{++}$  wave in the  $\eta\pi$  final state, which is dominated by the  $a_2(1320)$  [51]. In the analyzed range of  $0.1 < t' < 1.0(\text{GeV}/c)^2$ , the observed suppression is twice as large as the suppression of  $M = 1$  versus  $M = 0$  waves.

Nonresonant and resonant contributions are expected to follow different production paths with possibly different dependences on  $t'$ . In order to investigate possible nonresonant contributions, we show in Figs. 17 and 18 the intensities of four selected waves for two intervals of  $t'$ , i.e.  $0.100 < t' < 0.113(\text{GeV}/c)^2$  and  $0.449 < t' < 0.724(\text{GeV}/c)^2$ , which represent regions

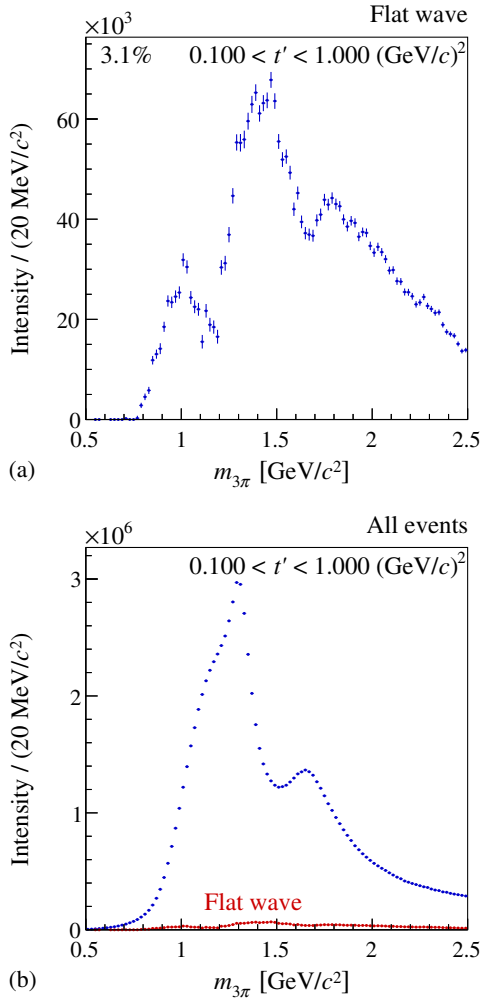


FIG. 13. The  $t'$ -summed intensity of the flat wave (a) and, for comparison, together with the total intensity of all partial waves (b).

of low and high  $t'$  in this analysis. When comparing these two regions, the shapes of the  $a_2(1320)$  and  $a_4(2040)$  resonances in the  $2^{++}1^+\rho(770)\pi D$  and  $4^{++}1^+\rho(770)\pi G$  waves, respectively, stay largely unaltered. In contrast, we observe that the peak in the  $1^{++}0^+\rho(770)\pi S$  wave, which presumably contains the  $a_1(1260)$ , significantly shifts toward higher masses with increasing  $t'$ . A similar but less strong effect is observed for the  $\pi_2(1670)$  peak in the  $2^{-+}0^+f_2(1270)\pi S$  wave. This shows that the peak structures in the latter two partial waves are not only due to ordinary resonances but are distorted by nonresonant contributions. The Deck process proposed in Ref. [25] and illustrated in Fig. 19 may provide an explanation for the  $t'$ -dependent nonresonant contributions observed in the  $1^{++}$  and  $2^{-+}$  waves. The  $t'$  dependence of the shape of the  $1^{++}0^+\rho(770)\pi S$  mass spectrum was already observed by the ACCMOR collaboration [14,16] and our results confirm their findings.

We show in Figs. 20 and 21 the same  $t'$  regions for the small-intensity waves  $1^{++}0^+f_2(1270)\pi P$ ,  $2^{++}1^+f_2(1270)\pi P$ ,

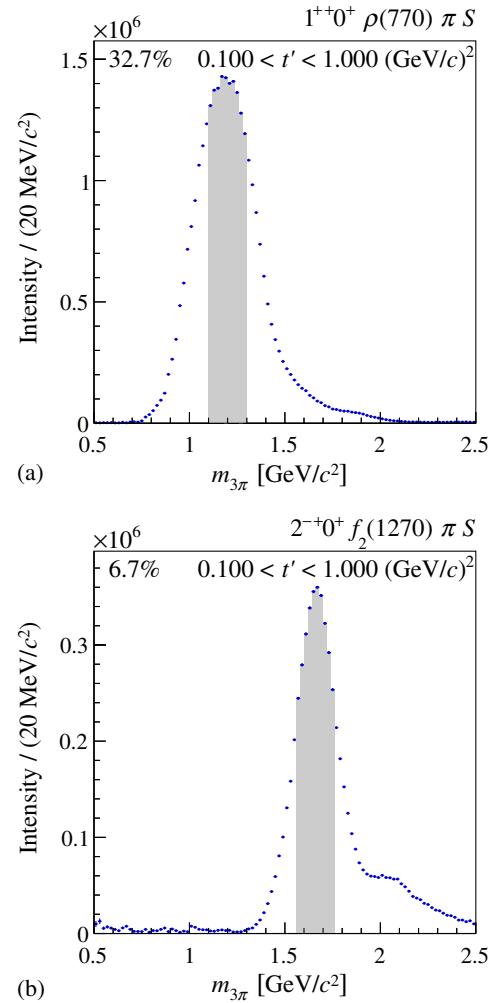


FIG. 14. The  $t'$ -summed intensities of major waves with spin projection  $M = 0$  showing in (a) the  $a_1(1260)$  and in (b) the  $\pi_2(1670)$ . The shaded regions indicate the mass intervals that are integrated over to generate the  $t'$  spectra [see Fig. 32(a)].

$2^{-+}0^+\rho(770)\pi F$ , and  $4^{++}1^+f_2(1270)\pi F$ . All waves show a pronounced dependence of the mass spectrum on  $t'$ . In contrast to the  $1^{++}\rho(770)\pi S$  wave, the  $a_1(1260)$  cannot be clearly identified in the  $f_2(1270)\pi P$  wave. Instead, the latter wave shows a broad enhancement around 1.8 GeV/c<sup>2</sup> [see also Fig. 16(b)]. In the  $2^{++}f_2(1270)\pi P$  wave, the  $a_2(1320)$  exhibits a high-mass shoulder, which is particularly pronounced at large values of  $t'$ , although it is clearly identifiable also at low  $t'$ . Such a high-mass shoulder also becomes prominent for the  $\pi_2(1670)$  in the  $\rho(770)\pi F$  wave, for which the spectrum exhibits a richer structure than for the  $2^{-+}0^+f_2(1270)\pi S$  wave.

The selective effect of the orbital angular momentum  $L$  in the decay is clearly demonstrated in Figs. 22(a) and 22(b), which show the  $2^{-+}0^+f_2(1270)\pi$  waves with  $L = 0$  and  $L = 2$ . The  $\pi_2(1670)$  dominates the  $S$ -wave, while the  $\pi_2(1880)$  favors the  $D$ -wave. The  $\pi_2(1880)$  is considerably lighter than the expected radial excitation of the  $\pi_2(1670)$  ground state and has been rated as a viable hybrid-meson

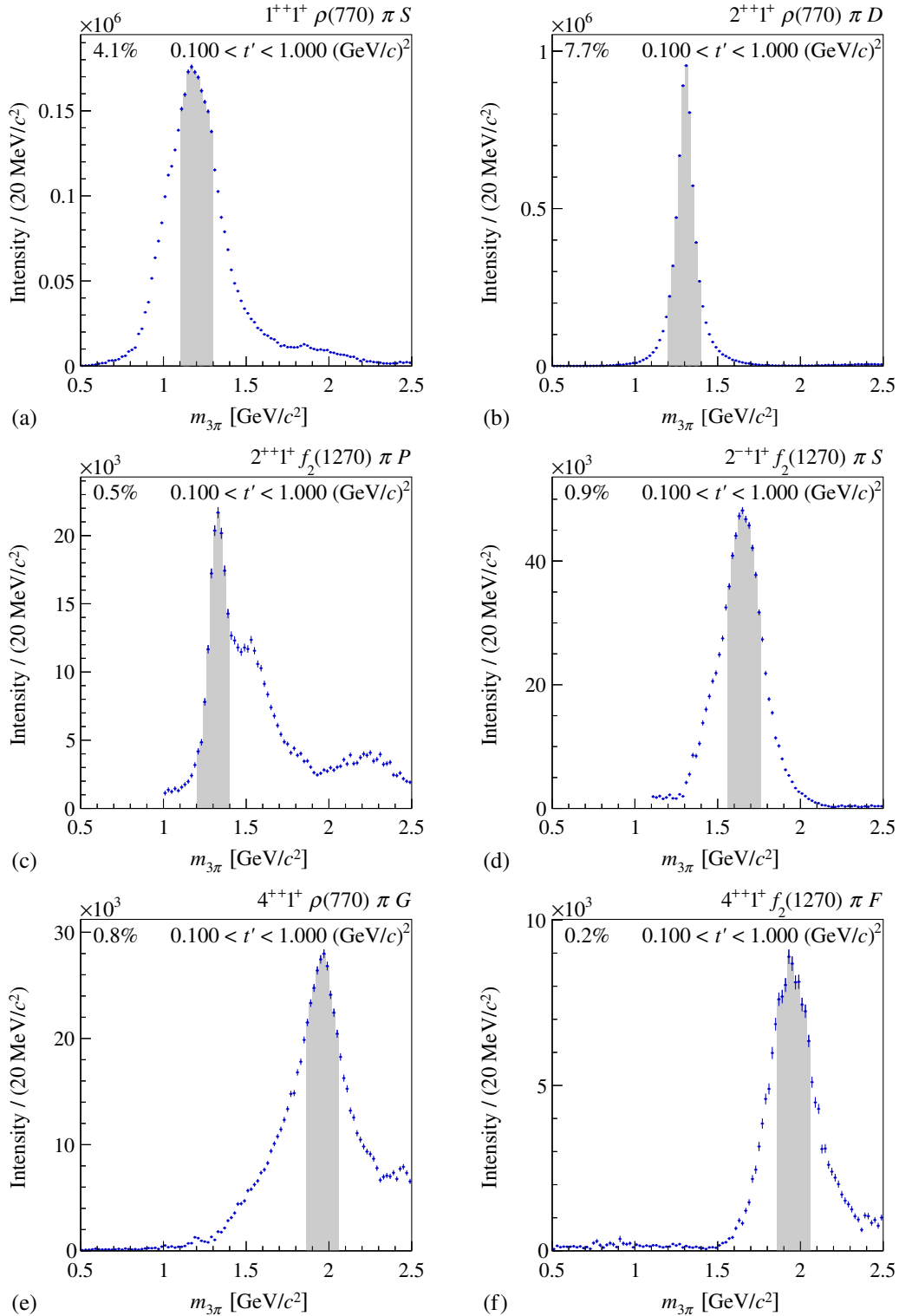


FIG. 15. The  $t'$ -summed intensity of waves with spin projection  $M = 1$  showing in (a) the  $a_1(1260)$ , in (b) and (c) the  $a_2(1320)$ , in (d) the  $\pi_2(1670)$ , and in (e) and (f) the  $a_4(2040)$ . The shaded regions indicate the mass intervals that are integrated over to generate the  $t'$  spectra [see Figs. 32(b), 33(a), 33(b), and 34].

candidate [1,52]. However, a dominance of  $S$  over  $D$ -wave  $f_2(1270)\pi$  decay modes was predicted for hybrid mesons by model calculations [53,54]. This is at variance with the present observation of a prevailing  $D$ -wave decay of the

$\pi_2(1880)$ . The existence of the  $\pi_2(1880)$  was questioned by Ref. [55], which explains it as an interference of the  $\pi_2(1670)$  ground state with the nonresonant Deck process causing an apparent shift of the peak position. This might

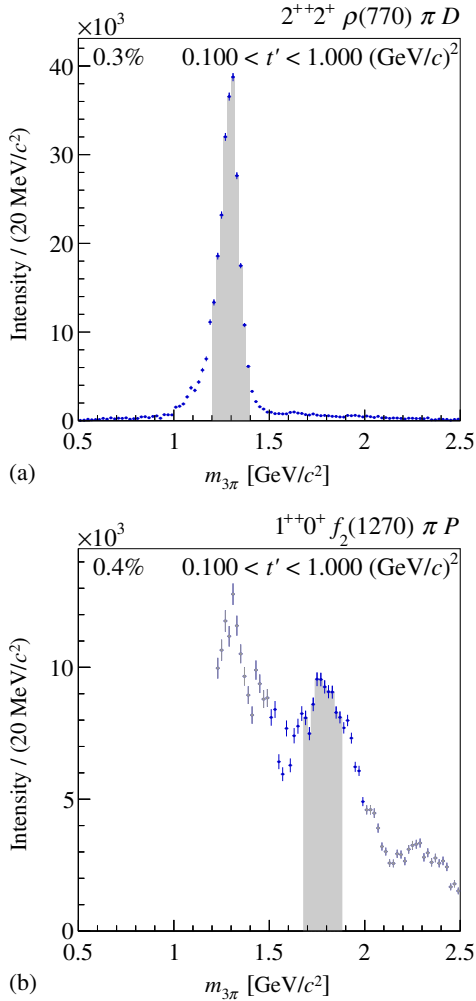


FIG. 16. Panel (a):  $t'$ -summed intensity of  $2^{++}2^+ \rho(770) \pi D$  wave with spin projection  $M = 2$  and the  $a_2(1320)$  peak. Panel (b):  $t'$ -summed intensity of  $1^{++}0^+ f_2(1270) \pi P$  wave with spin projection  $M = 0$ . In this wave, the mass regions below  $1.5$  GeV/c<sup>2</sup> and above  $2.0$  GeV/c<sup>2</sup> (shown by gray points) are sensitive to the truncation of the partial-wave expansion series (see Sec. IV F). In both waves, the shaded regions indicate the mass intervals that are integrated over to generate the  $t'$  spectra [see Fig. 33(c)].

be counterargued by the observation of two peaks in the  $2^{-+}0^+ \rho(770) \pi F$  wave [see Figs. 21(a), 21(c), and 22(d)]. Studying additional decay modes and the  $t'$  dependence of the mass spectra should resolve this issue.

#### D. Partial waves with $f_0(980)$ and broad $\pi\pi$ S-wave isobars

As discussed in the previous section, the shape of the peak in the  $a_1(1260)$  region in the  $1^{++}0^+ \rho(770) \pi S$  wave and that in the  $\pi_2(1670)$  region in the  $2^{-+}$  waves change as a function of  $t'$  [see Figs. 17(a), 17(c), 18(a), and 18(c)]. A possible explanation for this behavior is the Deck process. We have therefore investigated partial waves that are

expected to have small contributions from the Deck process. Owing to the nature and small width of the  $f_0(980)$ , this is in particular true for  $f_0(980) \pi$  partial waves. Only a few meson resonances have been observed to decay via  $f_0(980)$ , such as  $\pi(1800) \rightarrow f_0(980)\pi$ ,  $\phi(1020) \rightarrow f_0(980)\gamma$ ,  $\phi(2170) \rightarrow f_0(980)\phi$ , and  $\eta(1405) \rightarrow f_0(980)\eta$ , where the latter is a subthreshold decay. Among these, the  $\pi(1800)$  is the only isovector state and thus accessible in the  $3\pi$  final state. Because of its small width, the  $f_0(980)$  accounts for only a small fraction of the full  $\pi\pi$  S-wave. It is easily separated from the broad  $\pi\pi$  S-wave structure, which is shown in Fig. 10. Compared to the positive-reflectivity waves containing the  $\rho(770)$  isobar, those with the  $f_0(980)$  are suppressed by a factor of approximately 20. Figure 23 shows the  $t'$ -summed intensity of the coherent sum of all partial waves with an  $f_0(980)$  isobar and positive reflectivity, which amounts to a relative intensity of 3.3%.

The intensity distribution of the  $0^{-+}0^+ f_0(980) \pi S$  wave is dominated by the  $\pi(1800)$  peak [see Fig. 25(a)]. The more complicated mass spectrum of the  $2^{-+}0^+ f_0(980) \pi D$  wave is shown in Fig. 25(c). This wave, which should contain signals of  $\pi_2(1670)$  and  $\pi_2(1880)$ , is characterized by pronounced destructive interference around  $m_{3\pi} = 1.8$  GeV/c<sup>2</sup>.

The  $1^{++}0^+ f_0(980) \pi P$  wave is shown in Fig. 25(e). It exhibits the new axial-vector meson  $a_1(1420)$ . The resonance features of this signal were presented in Ref. [56]. It should be noted that the intensity of this wave corresponds to only about 0.3% of the total number of events. Since the signal is very small, we conducted several systematic studies that will be discussed in Sec. IV F.

The same partial waves discussed above are shown in the right column of Fig. 25 for the broad component of the  $\pi\pi$  S-wave as isobar, which is parametrized as described in Sec. IV A and denoted by  $[\pi\pi]_S$ . The intensity spectrum of the  $0^{-+}0^+ [\pi\pi]_S \pi S$  wave [see Fig. 25(b)] exhibits two pronounced maxima and differs considerably from that of the corresponding  $f_0(980) \pi$  wave in Fig. 25(a). The maximum at  $1.8$  GeV/c<sup>2</sup> corresponds to the  $\pi(1800)$ , but we also observe a broad structure around  $1.2$  GeV/c<sup>2</sup>, which could contain the  $\pi(1300)$ . As it will be discussed in Sec. V B, the latter structure has a very distinct dependence on  $t'$  with a minimum around  $t' \approx 0.35$  (GeV/c)<sup>2</sup>. Figure 24 shows as an example the intensity spectrum in two  $t'$  bins. At high  $t'$ , the  $\pi(1800)$  peak nearly vanishes and the structure around  $1.2$  GeV/c<sup>2</sup> is shifted toward lower  $m_{3\pi}$ . A more detailed analysis discussed in Sec. VI C indicates that in addition to interference effects with the  $\pi(1800)$  also nonresonant processes seem to contribute to the  $1.2$  GeV/c<sup>2</sup> mass region.

Another resonance that was observed to couple to the  $[\pi\pi]_S$  isobar is the  $\pi_2(1670)$  [9], whose main decay mode into  $f_2(1270)\pi$  is discussed above in Sec. IV C. The mass spectrum of the  $2^{-+}0^+ [\pi\pi]_S \pi D$  wave is shown in Fig. 25(d) and exhibits marked destructive interference effects at

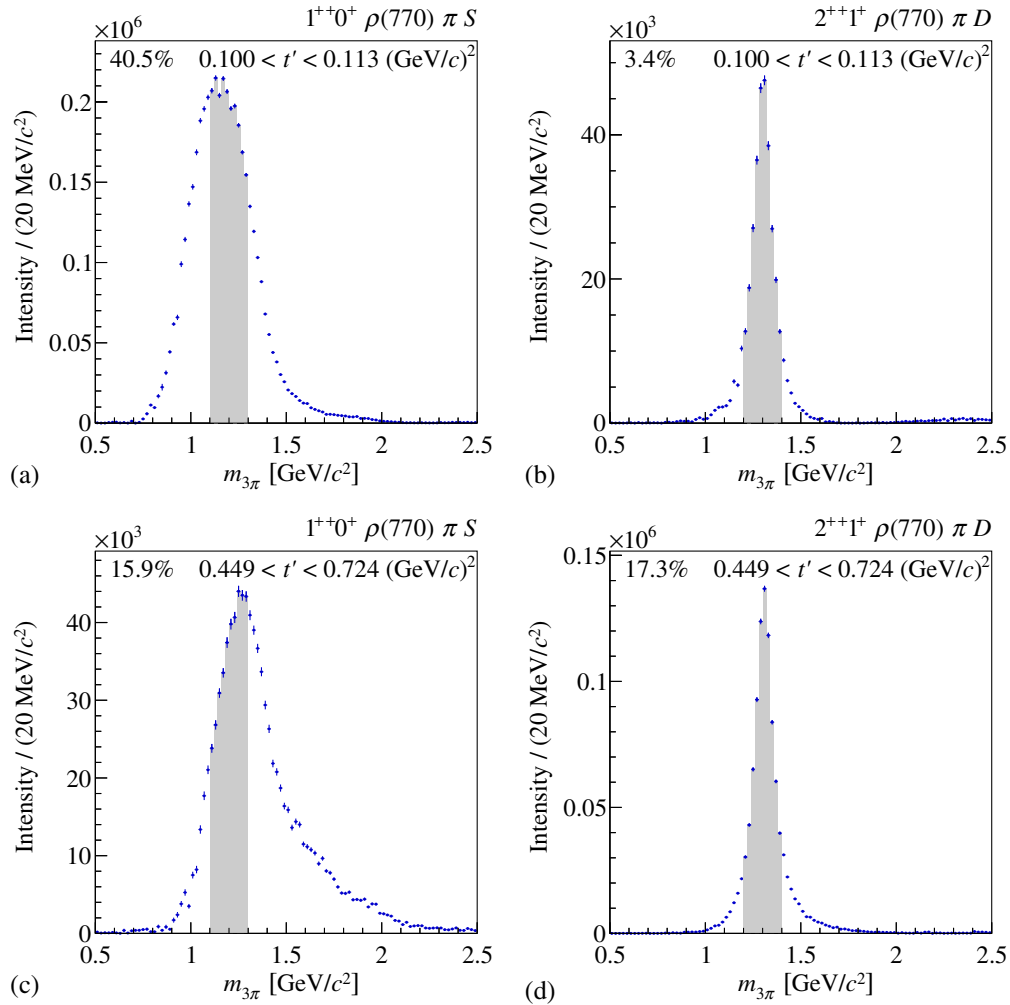


FIG. 17. The intensities of the  $1^{++}0^+\rho(770)\pi S$  and  $2^{++}1^+\rho(770)\pi D$  waves in two different  $t'$  regions. Upper row: low  $t'$ ; Lower row: high  $t'$ . The shaded regions indicate the mass intervals that are integrated over to generate the  $t'$  spectra.

masses around  $1.8 \text{ GeV}/c^2$ , similar to the ones observed in the corresponding wave with the  $f_0(980)$  decay mode in Fig. 25(c).

The  $1^{++}0^+[\pi\pi]_S\pi P$  wave is even more difficult to interpret [see Fig. 25(f)]. A significant signal is observed in the region of  $a_1(1260)$ . However, as it will be shown in Sec. VB and Sec. VI, this structure exhibits a strong  $t'$  dependence, which is a signature for significant nonresonant contributions.

Comparing the  $f_0(980)\pi$  and  $[\pi\pi]_S\pi$  decay modes, the latter are obviously more affected by nonresonant contributions. We will discuss the sector of partial waves with  $\pi\pi S$ -wave isobars again in Sec. VI in the context of an extended analysis.

### E. Comparison of fit result and real data

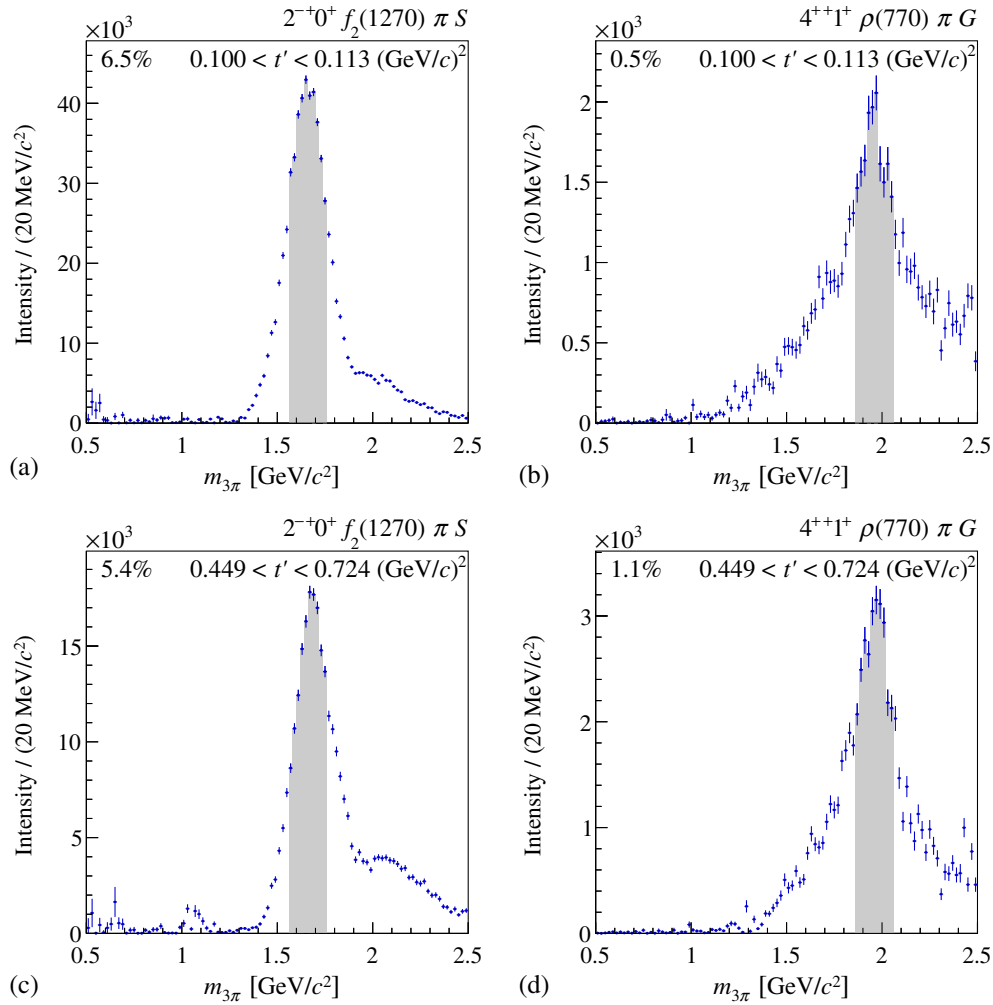
In order to estimate the goodness of the *mass-independent* fit, three-pion phase-space Monte Carlo events, which were processed through the detector simulation and reconstruction chain and satisfied the selection

criteria, were weighted with the intensity distribution of the fit model [see Eq. (24)]. For a good fit, distributions obtained from these weighted Monte Carlo events are expected to approximate the real data.

For fixed values of  $m_{3\pi}$  and  $t'$ , the phase space of the three final-state particles is five-dimensional. Therefore, we can show only projections in certain kinematic regions. For the comparison we use the same five kinematic variables that also enter in the decay amplitudes (see Sec. III B), i.e.  $\cos\vartheta_{\text{GJ}}$  and  $\phi_{\text{TY}}$  of the isobar in the Gottfried-Jackson frame, the isobar mass  $m_\varepsilon = m_{\pi^-\pi^+}$ , and  $\cos\vartheta_{\text{HF}}$  and  $\phi_{\text{HF}}$  of the  $\pi^-$  in the helicity frame.

Figures 26–29 show as examples the distributions of the kinematic variables in various regions of  $m_{3\pi}$  and  $t'$ . These kinematic regions contain different resonant and nonresonant contributions leading to different shapes of the angular distributions and the isobar mass spectrum.

In general, the agreement between the weighted Monte Carlo and the real-data events is very good, in particular at intermediate  $3\pi$  masses. At larger  $m_{3\pi}$ , we


 FIG. 18. Same as Fig. 17, but for the  $2^{-+}0^{+}f_2(1270)\pi S$  and  $4^{++}1^{+}\rho(770)\pi G$  waves.

observe small deviations concerning the description of the  $f_0(980)$  and  $f_2(1270)$  isobars [see Fig. 27(b)] as well as small localized differences in the angular distribution in the Gottfried-Jackson frame [see Figs. 27(e) and 29(e)].

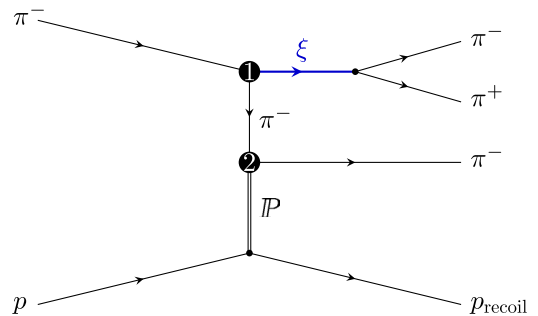
### F. Systematic studies

Given the high precision of the data, statistical uncertainties are negligibly small in most cases, i.e. systematic uncertainties are dominant. We have performed several tests to assess the stability of the result of the mass-independent fit. Here, we summarize the findings of these studies; more details can be found in Appendix B.

Possible effects from processes, in which the target proton is excited, are expected to be negligible. Due to Pomeron dominance, target excitations will be mostly  $N^*$ . The recoil-proton trigger and the momentum-conservation criterion applied in the event selection (see Secs. II B and II C) suppress such events on average by about an order of magnitude. The remaining contributions consist predominantly of low-mass  $N^*$  produced at large  $t'$ . In diffractive reactions, target and beam vertex factorize, so that these

events are expected to have only little effect on the production of the three-pion final state. As we assume for these events the proton mass for the mass of the recoiling particle, the calculated values of  $t'$  would be slightly shifted by values comparable to the  $t'$  resolution. The same is true for the reconstructed beam energy  $E_{\text{beam}}$ .

In order to reduce the probability for the fit to converge to a local maximum, the likelihood fit is repeated in each kinematic bin in  $m_{3\pi}$  and  $t'$  30 times with random starting


 FIG. 19. Example for a nonresonant production process for the  $3\pi$  final state as proposed by Deck [25].

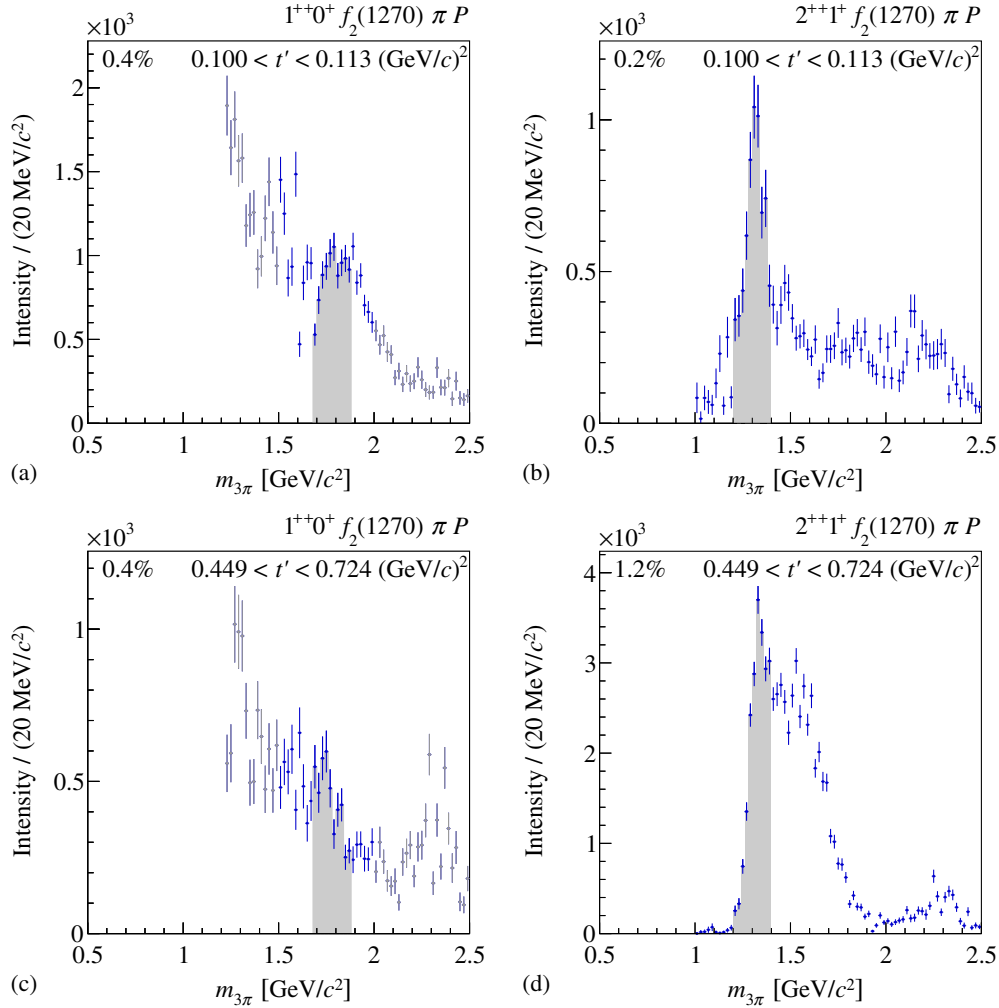


FIG. 20. Same as Fig. 17, but for the  $1^{++}0^+ f_2(1270) \pi P$  and  $2^{++}1^+ f_2(1270) \pi P$  waves. In the former wave, the mass regions below  $1.5 \text{ GeV}/c^2$  and above  $2.0 \text{ GeV}/c^2$  (shown by gray points) are sensitive to the truncation of the partial-wave expansion series (see Sec. IV F).

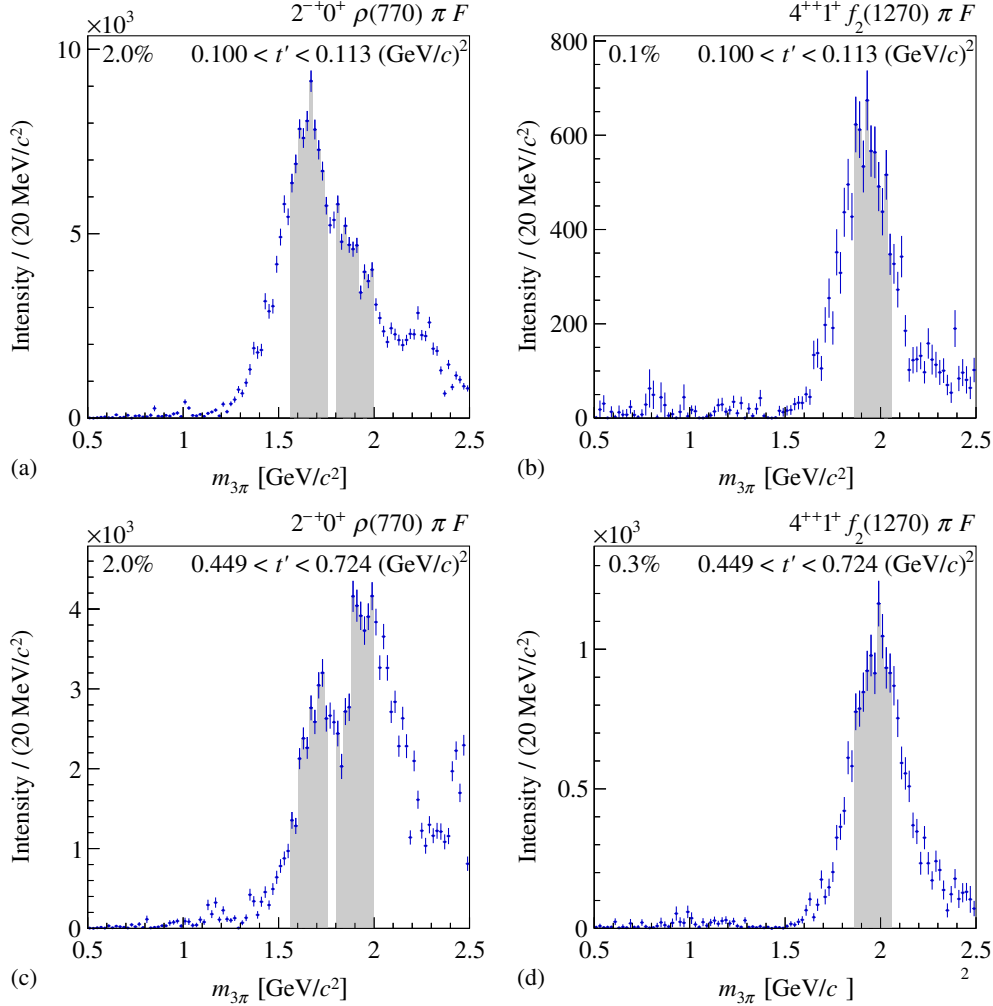
values for the transition amplitudes  $T_a^{re}$  in Eq. (27). From these 30 fits, the one with the highest likelihood is selected in order to generate the results presented in Secs. IV C and IV D. In the  $3\pi$  mass range above about  $1 \text{ GeV}/c^2$ , the fits reliably yield a single solution. Only a few fits are trapped in local maxima with significantly lower likelihood. In contrast, for mass bins below about  $1 \text{ GeV}/c^2$ , the fits find multiple local maxima that deviate from each other only by a few units of log-likelihood. We attribute this behavior to the fact that, due to the smaller phase-space volume at low  $m_{3\pi}$ , mainly the low-mass tails of the isobars contribute to the decay amplitudes. Therefore, it is harder to distinguish partial waves with different isobars. Since we do not expect any  $3\pi$  resonances below  $1 \text{ GeV}/c^2$ , no efforts were made to resolve these ambiguous solutions.

We have studied how the truncation of the partial-wave expansion series in Eq. (24) influences the intensities of the 18 partial waves discussed in this paper (see Table V) by comparing to a fit with a reduced set of only 53 partial waves [57]. Except for one wave, the intensities exhibit

only relatively small changes, which typically affect the high-mass regions. The intensity of the  $1^{++}0^+ f_2(1270) \pi P$  wave changes significantly in the mass regions above  $2.0 \text{ GeV}/c^2$  and below  $1.5 \text{ GeV}/c^2$ , the latter of which is attributed to model leakage from the  $\rho(770) \pi S$ -wave decay of the  $a_1(1260)$ . However, the region around the enhancement at  $1.8 \text{ GeV}/c^2$  [marked by the shaded region in Fig. 16(b)] is only slightly affected.

As mentioned in Sec. III B, we do not apply relativistic corrections to the decay amplitudes in the partial-wave analysis. First studies show that the effect on the shapes of the selected 18 waves is small.

In order to study the effect of the rank of the spin-density matrix, the data are fit with a rank-2 spin-density matrix instead of the rank-1 for the positive-reflectivity sector. The most striking feature of the rank-2 fit, which has nearly twice the number of free parameters, is that the flat wave practically disappears. In addition, intensity is shifted from the negative into the positive-reflectivity sector. However, the fit shows substantial instabilities and artificial structures


 FIG. 21. Same as Fig. 17, but for the  $2^{-+}0^+\rho(770)\pi F$  and  $4^{++}1^+f_2(1270)\pi F$  waves.

in the  $m_{3\pi}$  region between 1.0 and 1.3  $\text{GeV}/c^2$  in some partial waves. We therefore conclude that the rank-1 fit offers a better description of the data using significantly less parameters. For more details see Appendix B 1.

Omitting the waves with negative reflectivity from the wave set feeds intensity mostly into the flat wave, but causes little change of positive-reflectivity waves (see Appendix B 2). This means that in the given range of four-momentum transfer, the positive and negative-reflectivity sectors do not mutually influence each other and are well-separated by the fit as opposed to the case of very small  $t' < 10^{-3} (\text{GeV}/c)^2$  [7].

The isobar parametrizations (see Sec. IV A) are an important input for the PWA model. The  $\rho(770)$  is the dominant isobar. For most of the waves in Table V, the intensity distribution is not sensitive to the details of the  $\rho(770)$  parametrization or to small changes of the used parameter values. In contrast, the region around the  $a_1(1260)$  mass in the  $1^{++}0^+[\pi\pi]_S\pi P$  wave and the  $a_2(1320)$  signal in the  $2^{++}1^+f_2(1270)\pi P$  wave change significantly (see Sec. B 3). Both seem to be contaminated

by model leakage due to the imperfect description of the  $\rho(770)$ . The dependence of the PWA result on the parametrization of the  $f_0(980)$  and that of the broad  $\pi\pi$  S-wave component is studied as well. Using a simple S-wave Breit-Wigner amplitude [Eq. (31) with Eq. (42)] instead of the Flatté parametrization [Eq. (43)] for the  $f_0(980)$  reduces the height of the intensity peaks of the resonances decaying into  $f_0(980)\pi$  by about a factor of two (see Appendix B 3). However, the shapes of the peaks in these partial waves remain unchanged. In the mass region above 1.3  $\text{GeV}/c^2$ , the fit with the  $f_0(980)$  Flatté parametrization has a significantly higher likelihood than the one with the S-wave Breit-Wigner amplitude. This indicates that the data are better described by the Flatté parametrization.

The influence of the parametrization used for the broad component of the  $\pi\pi$  S-wave on the PWA result is studied by performing a fit with an alternative description of the mass-dependence of the isobar amplitude. Instead of the modified  $M$  solution from Ref. [41] (see Sec. IV A), the  $K_1$  solution from Ref. [41] with the  $f_0(980)$  pole subtracted using a simple S-wave Breit-Wigner amplitude is used.

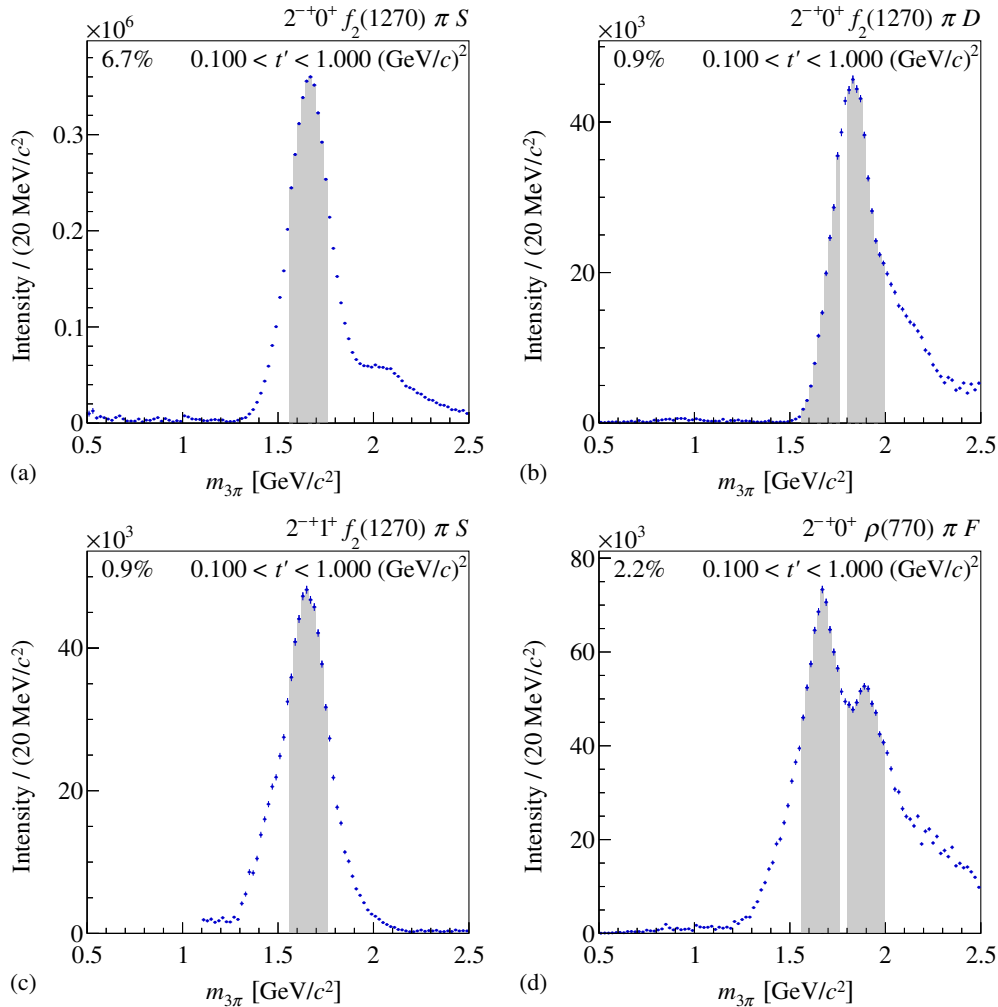


FIG. 22. The  $t'$ -summed intensities of  $2^{-+}M^+f_2(1270)\pi L$  waves in panels (a), (b), and (c) and of  $2^{-+0^+}\rho(770)\pi F$  wave in panel (d). The  $\pi_2(1670)$  dominates the waves shown in (a) and (c), the  $\pi_2(1880)$  the one shown in (b). Both resonances appear in the wave shown in (d). Upper row: comparison of same decay mode but different orbital angular momenta  $L = 0$  and  $2$  in the decay; Left column: comparison of same decay mode but different spin projections  $M = 0$  and  $1$ . The shaded regions indicate the mass intervals that are integrated over to generate the  $t'$  spectra discussed in Sec. V B.

This parametrization was originally used by the VES experiment [20]. The Breit-Wigner for the  $f_0(980)$  is similar to the one employed in the  $f_0(980)$  study described above. In order to be consistent, the Breit-Wigner amplitude is also used for all waves with the  $f_0(980)$  isobar. The observed variations in the fit result are small.

Performing the PWA on a data sample without the CEDAR, RICH, and central-production vetos described in Sec. II C shows that the result is not very sensitive to backgrounds from kaon diffraction, kaon pairs in the final state, and central-production reactions (see Appendix B 4). The partial-wave intensities scale approximately with the number of events, only the relative intensity of the flat wave increases. It is very unlikely that the peak around  $m_{3\pi} = 1.4 \text{ GeV}/c^2$  in the  $1^{++0^+}f_0(980)\pi P$  wave is caused by kaon-induced reactions or that it stems from kaonic final states misinterpreted as pionic ones. The CEDAR and RICH vetos applied in the event selection reduce such

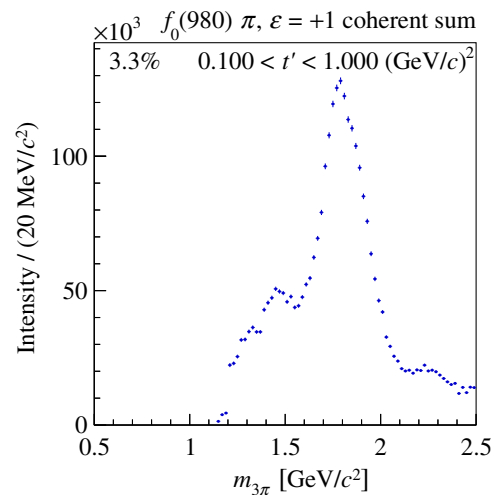


FIG. 23. Intensity of the coherent sum of all  $f_0(980)\pi$  waves with positive reflectivity, summed over all  $t'$  bins.

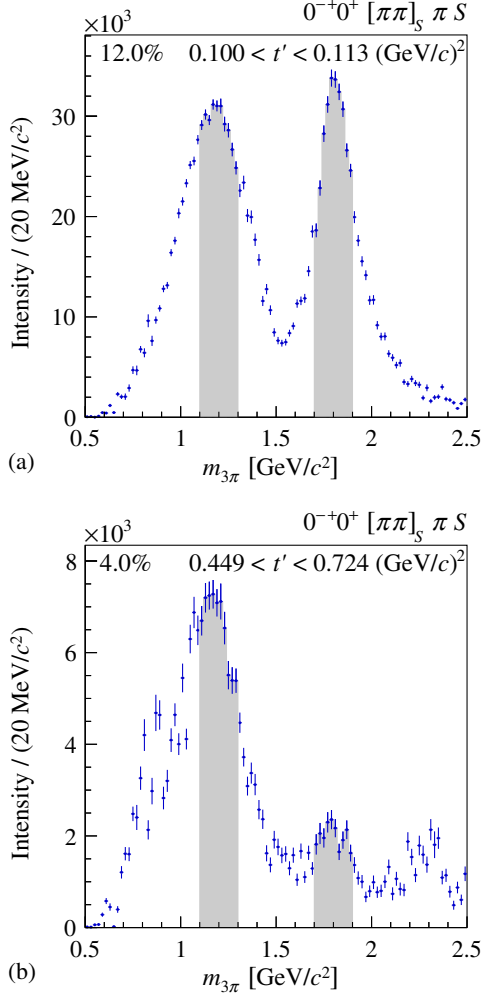


FIG. 24. Intensity of the  $0^{-+}0^{+}[\pi\pi]_S\pi S$  wave in two different  $t'$  regions. (a) low  $t'$ ; (b) high  $t'$ . The shaded regions indicate the mass intervals that are integrated over to generate the  $t'$  spectra.

contaminations considerably. Further studies show that the signal is not correlated with these cuts.

In summary, the PWA fits converge reliably for  $3\pi$  masses above about  $1 \text{ GeV}/c^2$ . The shapes of clear resonance peaks are stable with respect to changes of the PWA model. However, in some cases the height of the intensity peaks is sensitive to the isobar parametrization. This issue will mostly be resolved for the  $\pi\pi$  S-wave isobars by applying a method introduced in Sec. VI, by which the isobar amplitudes are extracted from the data.

## V. $t'$ DEPENDENCES

Figures 30(a) and 30(b) illustrate how the shape of the measured three-pion invariant mass spectrum changes with  $t'$ , while Figs. 30(c) and 30(d) show the change of the measured  $t'$  distribution with  $3\pi$  mass. It is apparent that the  $t'$  spectrum strongly depends on  $m_{3\pi}$ . This observation has motivated us to perform the PWA in bins of  $t'$  instead of weighting the partial waves with  $t'$ -dependent model functions, which has been the conventional approach.

In this chapter, we will elaborate on the details of the observed  $t'$  distributions. We will start with global spectra, from which we determine the  $t'$  dependence as a function of  $m_{3\pi}$ . Such an analysis comes closest to the traditional description of high-energy reactions in terms of Regge exchange. Using the results from the *mass-independent* fit outlined in Sec. IV, we can in addition separate the contributions of various partial waves to the  $t'$  spectrum. Comparing different  $3\pi$  mass regions that are either dominated by well-established resonances or by nonresonant contributions, various patterns become apparent.

### A. Overall $t'$ dependence

The first extensive study of the  $3\pi$  mass dependence of the  $t'$  spectrum was performed by the ACCMOR collaboration [13,16]. They investigated the reaction  $\pi^{-} + p \rightarrow \pi^{-}\pi^{-}\pi^{+} + p$  at 63 and 94 GeV/c incoming pion momentum and determined the  $t'$  dependence as a function of  $m_{3\pi}$  in the range  $t' < 1.0$  (GeV/c)<sup>2</sup>. The  $t'$  dependence was parametrized for each 50 MeV/c<sup>2</sup> wide  $3\pi$  mass bin by two exponentials:

$$\frac{dN}{dt'}(t'; m_{3\pi}) = A_1(m_{3\pi})e^{-b_1(m_{3\pi})t'} + A_2(m_{3\pi})e^{-b_2(m_{3\pi})t'}, \quad (44)$$

with real-valued parameters  $A_i$ . The ACCMOR collaboration observed that the two slope parameters  $b_{1,2}$  are different at small values of  $m_{3\pi}$  and that they vary significantly up to values of  $m_{3\pi}$  of about  $1.2 \text{ GeV}/c^2$ . This marks the onset of resonance production. Beyond this mass value, the slope values of  $b_1 \approx 12$  (GeV/c)<sup>-2</sup> and  $b_2 \approx 5$  (GeV/c)<sup>-2</sup> stay almost constant [see open circles in Fig. 31(a)].

We perform the same study on the present data in a wider  $3\pi$  mass range and using finer  $m_{3\pi}$  bins of  $20 \text{ MeV}/c^2$  width. In each mass bin, the acceptance-corrected  $t'$  spectrum, which is obtained from the mass-independent fit in 11  $t'$  bins, is fit by Eq. (44). The result is shown as filled circles in Fig. 31(a). The general pattern and also the absolute values for the slope parameters agree nicely with the ACCMOR results. We observe a strong dependence of both slope parameters on  $m_{3\pi}$ . In the region  $m_{3\pi} < 1.0 \text{ GeV}/c^2$  below the resonances, only a few partial waves contribute significantly to the spectrum, i.e. the  $1^{++}0^{+}\rho(770)\pi S$  (57.1%),  $0^{-+}0^{+}[\pi\pi]_S\pi S$  (12.8%),  $1^{++}1^{+}\rho(770)\pi S$  (8.3%),  $1^{++}0^{+}[\pi\pi]_S\pi P$  (4.2%), and  $0^{-+}0^{+}\rho(770)\pi P$  (4.1%) waves. In this region, the parameter  $b_1$  representing the steeper component shows a rapid drop with increasing three-pion mass. The parameter  $b_2$  representing the shallower component exhibits less variation. Its mass dependence shows a dip by  $2$  (GeV/c)<sup>-2</sup> at around  $m_{3\pi} = 1.0 \text{ GeV}/c^2$ . Approaching the mass region of  $a_1(1260)$  and  $a_2(1320)$ , above

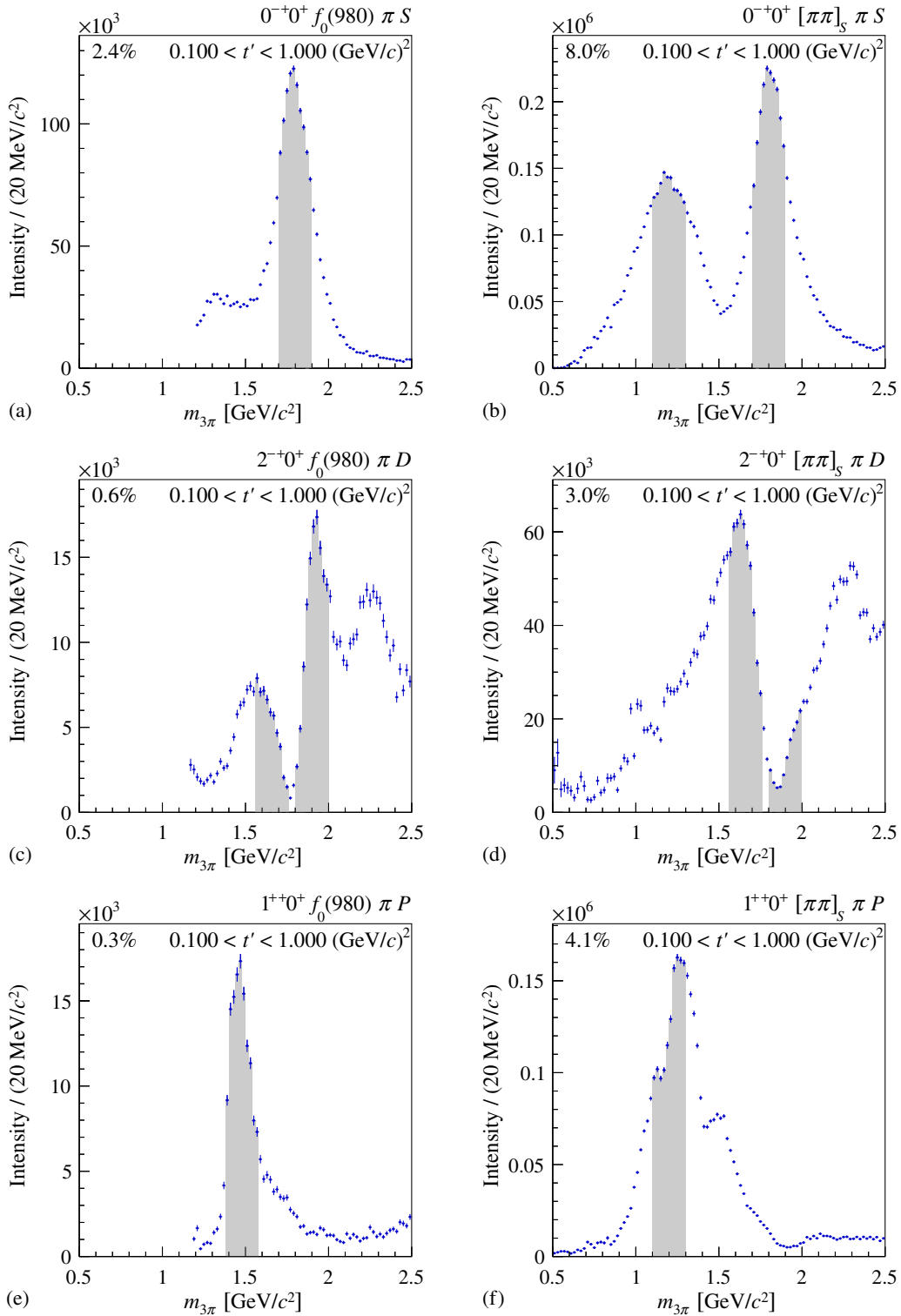


FIG. 25. The  $t'$ -summed intensity for selected waves with  $\pi\pi$   $S$ -wave isobars. Left column: waves with the narrow  $f_0(980)$  isobar; Right column: waves with the broad  $[\pi\pi]_S$  isobar. The  $J^{PC} = 0^{-+}$  waves in the top row show the  $\pi(1800)$ . The structure at 1.2  $\text{GeV}/c^2$  is probably mainly of nonresonant origin. The  $2^{-+}$  intensities in the center row exhibit a complicated destructive interference pattern around 1.8  $\text{GeV}/c^2$ . The bottom row shows an enhancement in the region of the  $a_1(1260)$  in the  $1^{++}0^{+}[\pi\pi]_S \pi P$  wave and a new state, the  $a_1(1420)$ , in  $1^{++}0^{+}f_0(980) \pi P$ . The shaded regions indicate the mass intervals that are integrated over to generate the  $t'$  spectra (see Figs. 35 and 36).

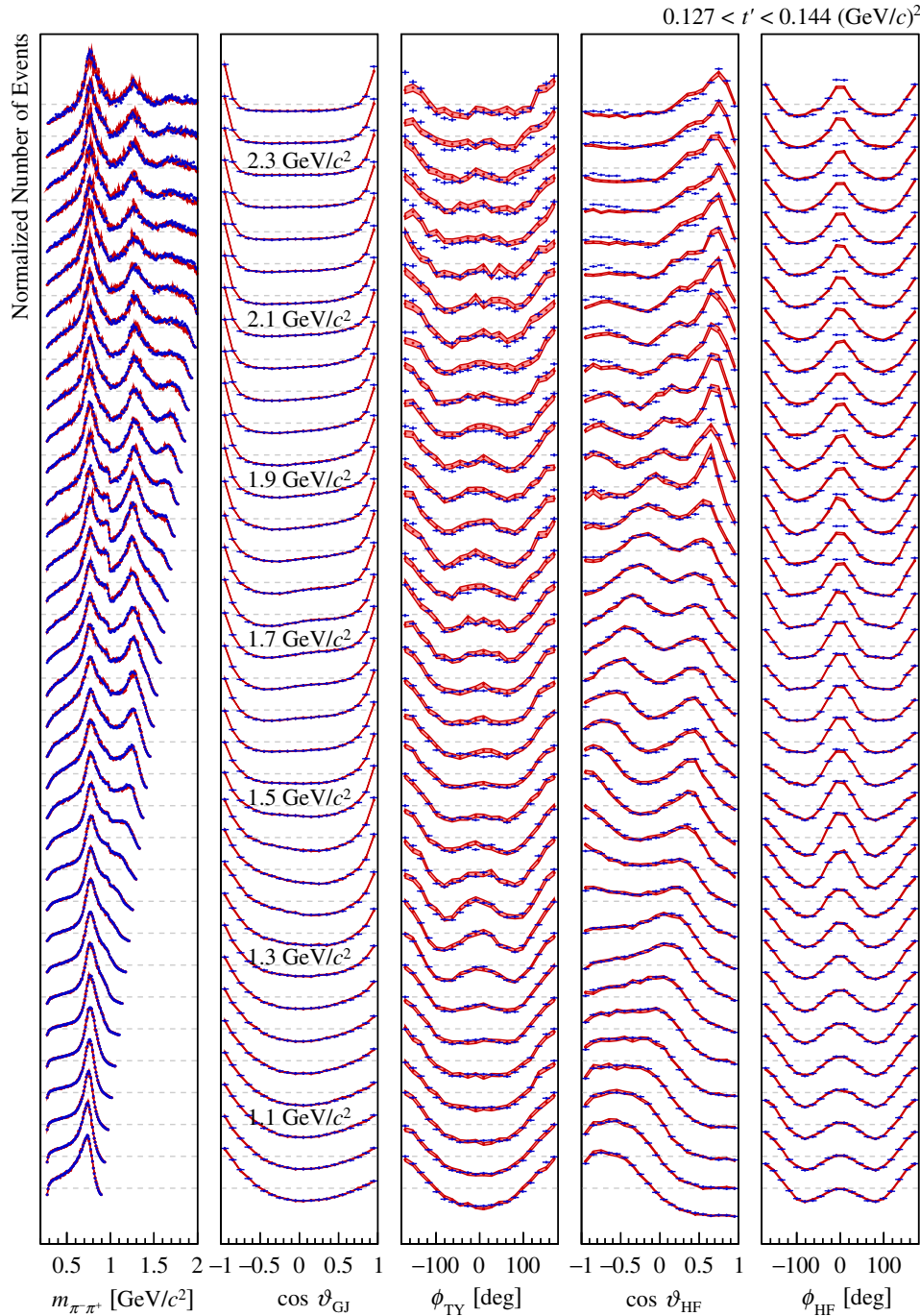


FIG. 26. Distributions of the five phase-space variables used to calculate the decay amplitudes shown for different  $3\pi$  mass bins in the region  $0.127 < t' < 0.144$   $(\text{GeV}/c)^2$ . Each distribution is shown for real data (blue points) and for weighted Monte Carlo events (red bands), which are generated according to the fit result. Each distribution is normalized to its maximum deviation from its average  $y$  value. Along the ordinate, the average  $y$  values for the distributions (indicated by gray lines) are shifted equidistantly with respect to one another. The  $3\pi$  mass ranges from 1.0 to 2.4  $\text{GeV}/c^2$  and is subdivided into 40  $\text{MeV}/c^2$  wide bins. The central values of selected  $3\pi$  mass bins are given as labels in the  $\cos \vartheta_{GJ}$  distribution.

approximately  $1.3 \text{ GeV}/c^2$ , the  $m_{3\pi}$  dependence of  $b_1$  and  $b_2$  changes abruptly:  $b_1$  drops much slower, decreasing from about  $12 (\text{GeV}/c)^{-2}$  at  $1.3 \text{ GeV}/c^2$  to  $8 (\text{GeV}/c)^{-2}$  at  $2.5 \text{ GeV}/c^2$ , whereas  $b_2$  stays nearly constant at about  $4 (\text{GeV}/c)^{-2}$  over the same mass range.

Figure 31(b) shows the ratio of the contributions

$$I_1 \equiv A_1 \int_{t'_{\min}}^{t'_{\max}} dt' e^{-b_1 t'} \quad \text{and} \quad I_2 \equiv A_2 \int_{t'_{\min}}^{t'_{\max}} dt' e^{-b_2 t'} \quad (45)$$

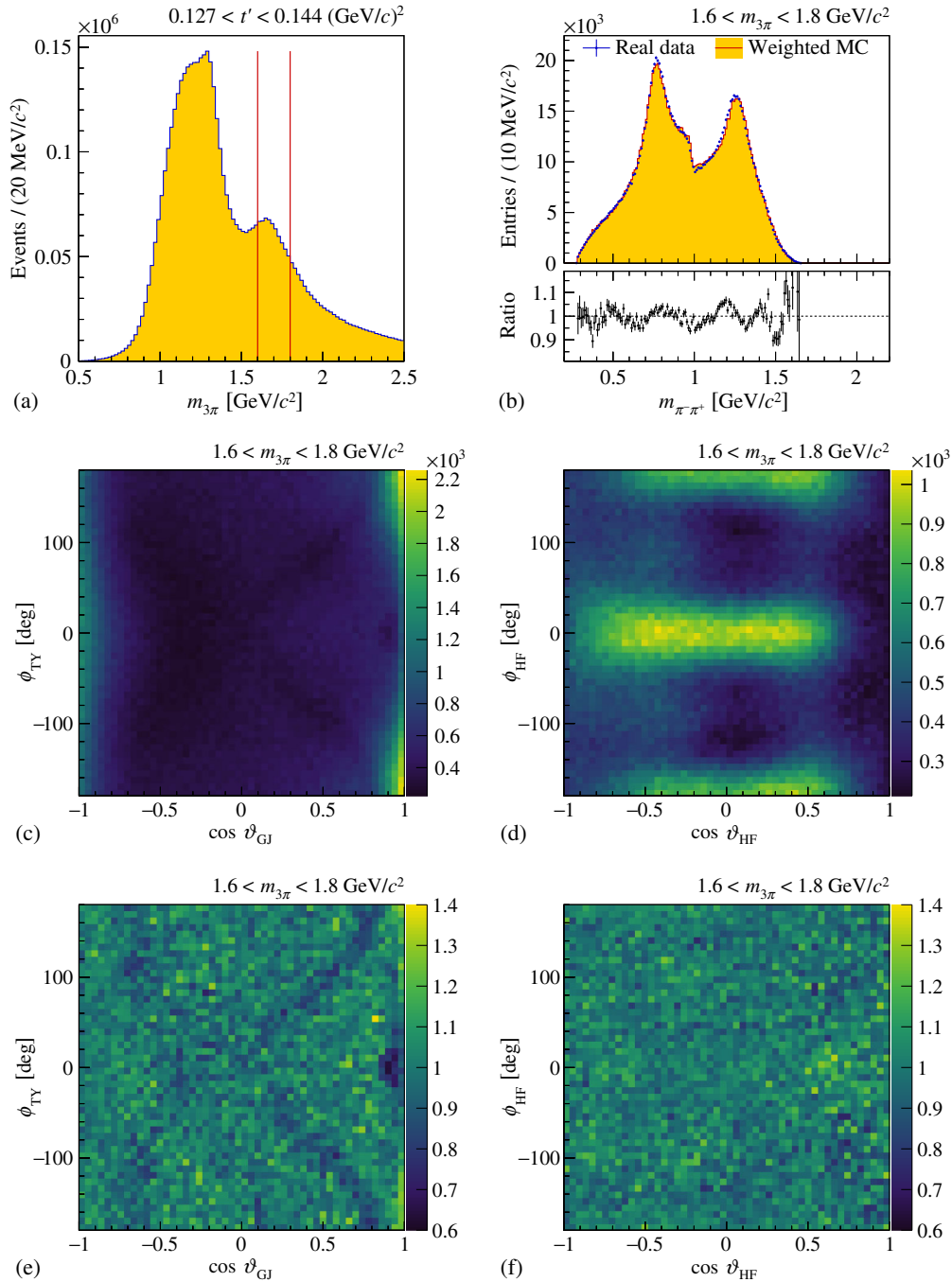


FIG. 27. Comparison of kinematic distributions of weighted Monte Carlo events, generated according to the fit result, with the corresponding real-data distributions in the low- $t'$  region  $0.127 < t' < 0.144$  ( $\text{GeV}/c^2$ )<sup>2</sup>. Panel (a) shows the acceptance-corrected  $3\pi$  invariant mass distribution. The other panels show kinematic distributions in the mass interval  $1.6 < m_{3\pi} < 1.8$   $\text{GeV}/c^2$  around the  $\pi_2(1670)$ , which is indicated by vertical red lines in (a). (b) invariant mass spectrum of the  $\pi^-\pi^+$  subsystem; (c) distribution of the Gottfried-Jackson angles for real data; (e) ratio of the real-data distribution in (c) and that of the weighted Monte Carlo. Panels (d) and (f) show the respective distributions for the helicity angles. Note that (b), (c), and (d) have two entries per event.

of the two exponentials from Eq. (44), integrated from  $t'_{\min} = 0.1$  ( $\text{GeV}/c^2$ )<sup>2</sup> to  $t'_{\max} = 1.0$  ( $\text{GeV}/c^2$ )<sup>2</sup>. As observed for the slope parameters, the regions below and above the resonance show very different behavior. Below the resonance region, the component with the steep slope  $b_1$  dominates and its contribution reaches a maximum at

$3\pi$  masses of approximately  $1.0$   $\text{GeV}/c^2$ . From there, it drops quickly with a shallow minimum around  $m_{3\pi} = 1.3$   $\text{GeV}/c^2$ . This dip is presumably caused by the onset of the  $2^{++}$  waves with  $M = 1$ . Above about  $1.3$   $\text{GeV}/c^2$ , the relative contributions of the two exponentials only depend weakly on  $m_{3\pi}$  with almost equal relative weights for the

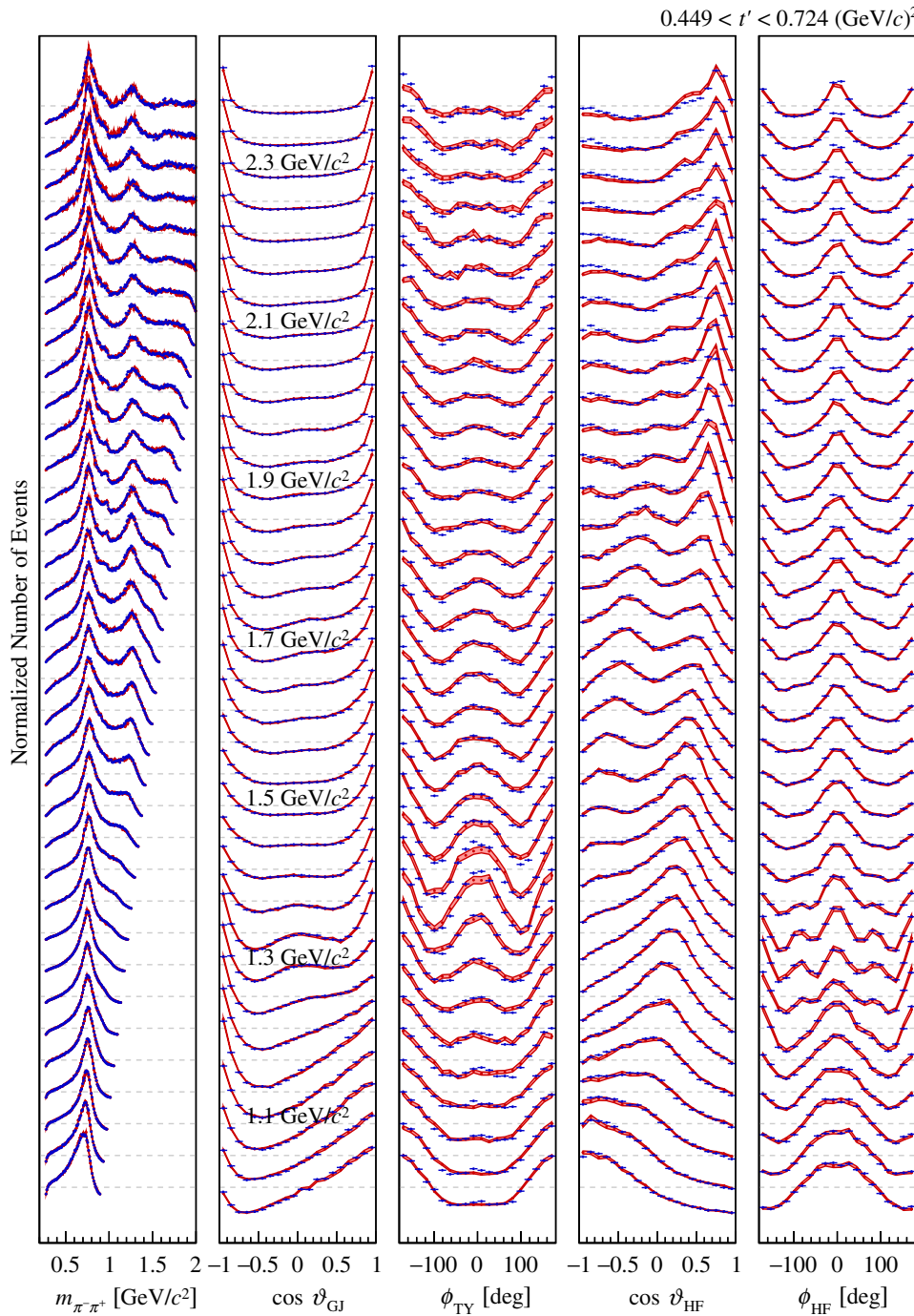


FIG. 28. Same as Fig. 26, but for the high- $t'$  region  $0.449 < t' < 0.724 \text{ (GeV}/c^2\text{)}^2$ .

two terms. The ACCMOR data show a qualitatively similar behavior. The agreement with the present data is, however, not as good as that observed for the slopes.

To our knowledge, the complicated mass dependence of the  $t'$  spectra described above is not well understood. In the region around  $1.3 \text{ GeV}/c^2$ , nonresonant processes are known to play an important role. Most available calculations describe these processes as the dissociation of the beam pion into the isobar  $\xi^0$  and the bachelor  $\pi^-$ , followed by diffractive scattering of one of the beam fragments (typically

the  $\pi^-$ ) off the target proton (see Fig. 19). These calculations focus mainly on the  $3\pi$  mass dependence and are based on  $\pi\pi$  and  $\pi p$  elastic-scattering data [16,25,55,58,59]. The more elaborate *three-component Deck model* [60–62] describes the reaction  $\pi^- + p \rightarrow \xi^0 \pi^- + p_{\text{recoil}}$  by including  $\xi$  as well as  $\pi$  exchanges in addition to direct production of  $\xi^0 \pi^-$  via Pomeron exchange. In general, such nonresonant processes exhibit a dependence on  $t'$  that is different from that of resonant production. Interferences between resonant and nonresonant processes may in addition modify the  $t'$  spectra.

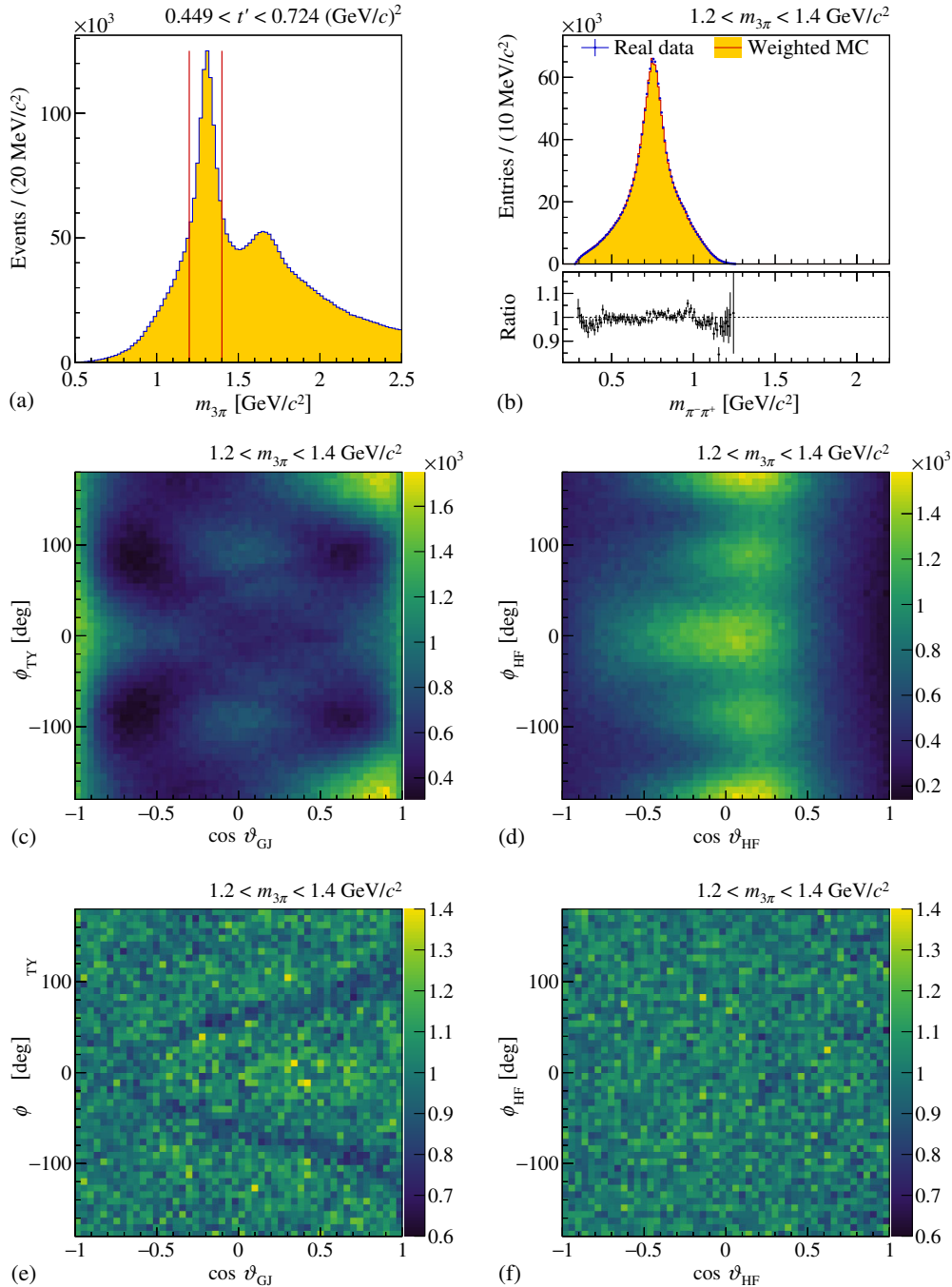


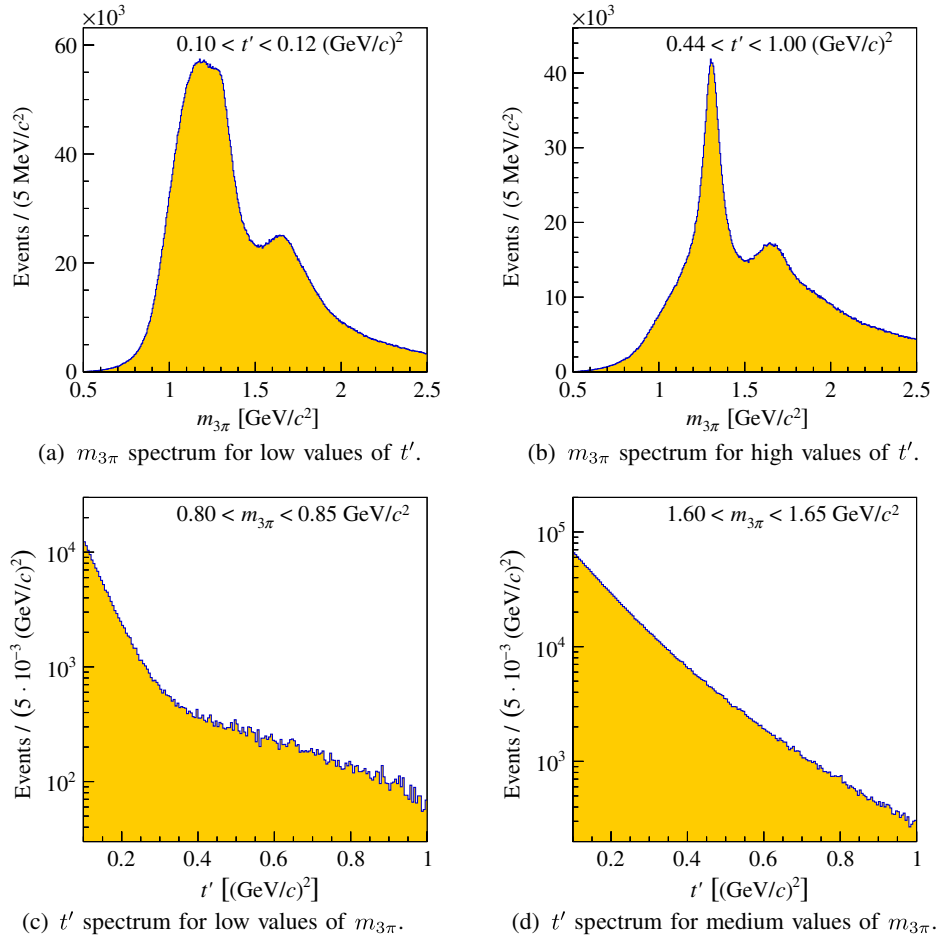
FIG. 29. Same as Fig. 27, but for the high- $t'$  region  $0.449 < t' < 0.724$  ( $\text{GeV}/c^2$ ) and the mass slice  $1.2 < m_{3\pi} < 1.4$   $\text{GeV}/c^2$  around the  $a_2(1320)$ .

The three-component Deck model describes the correlations between the  $\xi\pi$  invariant mass, the slope of the  $t'$  spectrum, and the  $\cos \vartheta_{GJ}$  distribution in detail and predicts the existence of interference minima in the  $t'$  spectra. As it will be shown in the following section, the  $t'$  spectra of some partial waves exhibit such kind of minima in certain  $3\pi$  mass regions.

### B. $t'$ dependences of individual partial waves

Using the partial-wave decomposition of the mass spectrum from the *mass-independent* fit as presented

in Sec. IV C, we can now study the  $t'$  dependence of the intensity of individual partial waves in different mass regions. The selected mass regions are indicated by shaded bands in the spectral distributions shown in Sec. IV. The corresponding  $t'$  spectra are obtained by integrating the partial wave intensities over those mass regions. The integrated intensities are presented using horizontal bars, the lengths of which represent the widths of the given  $t'$  bins. Blue horizontal lines represent the central values. The height of the gray


 FIG. 30. The  $t'$  dependence of the measured  $3\pi$  invariant mass spectrum and vice versa.

horizontal bars corresponds to the statistical uncertainty of the intensity.

We compare waves with the same isobars and angular momentum in the decay but with different spin projections  $M$ . Figure 32 gives an example for the  $1^{++}M^+\rho(770)\pi$   $S$  intensities with  $M = 0$  and 1 integrated over the range  $1.1 < m_{3\pi} < 1.3$   $\text{GeV}/c^2$ , which covers part of the  $a_1(1260)$ . Figures 33(a) and 33(c) show the analog comparison for  $2^{++}M^+\rho(770)\pi$   $D$  waves with  $M = 1$  and 2.

Alternatively, waves with same quantum numbers but different isobars can be compared, again keeping the mass interval fixed. Figure 33 shows this for the  $2^{++}1^+$  waves with the  $\rho(770)$  isobar and  $L = 2$  along with waves with the  $f_2(1270)$  isobar and  $L = 1$ , both in the mass region  $1.2 < m_{3\pi} < 1.4$   $\text{GeV}/c^2$  around the  $a_2(1320)$ . A comparison of the  $t'$  spectra of the  $4^{++}1^+\rho(770)\pi$   $G$  and  $f_2(1270)\pi F$  waves for  $1.86 < m_{3\pi} < 2.06$   $\text{GeV}/c^2$  is given by Fig. 34.

We may also compare the  $t'$  spectra of the same partial wave in different mass intervals. In Fig. 35, this is shown for the  $0^{-+}0^+[\pi\pi]_S\pi S$  wave using the peak regions  $1.1 < m_{3\pi} < 1.3$   $\text{GeV}/c^2$  and  $1.7 < m_{3\pi} < 1.9$   $\text{GeV}/c^2$ . These mass intervals contain the low-mass part of a

potential  $\pi(1300)$  contribution and the peak region of the  $\pi(1800)$ , respectively.

From the above figures, we can see that at low  $t'$ , all waves have a large single-exponential component. In addition, we can distinguish three characteristically different patterns in the  $t'$  spectra: (i) for about half the spectra, the single exponential dominates the full measured  $t'$  range; (ii) many waves show larger deviations at higher  $t'$ , suggesting additional components; (iii) a few waves exhibit a minimum in the  $t'$  region between 0.3 and 0.6  $(\text{GeV}/c)^2$  [see e.g. Figs. 32(b) and 35(a)]. The position of such minima is far below the diffractive minima observed in elastic  $\pi p$  scattering.

Our general ansatz for the description of the observed  $t'$  spectra is a sum of two terms, each containing an exponential function multiplied by an  $M$ -dependent term<sup>8</sup> of the form  $(t')^M$  with  $M \geq 0$ :

$$\frac{dN}{dt'}(t') = (t')^M [A_1 e^{-b_1 t'} + A_2 e^{-b_2 t'}]. \quad (46)$$

<sup>8</sup>Given by the forward limit of the Wigner  $D$ -functions (see Ref. [63]).

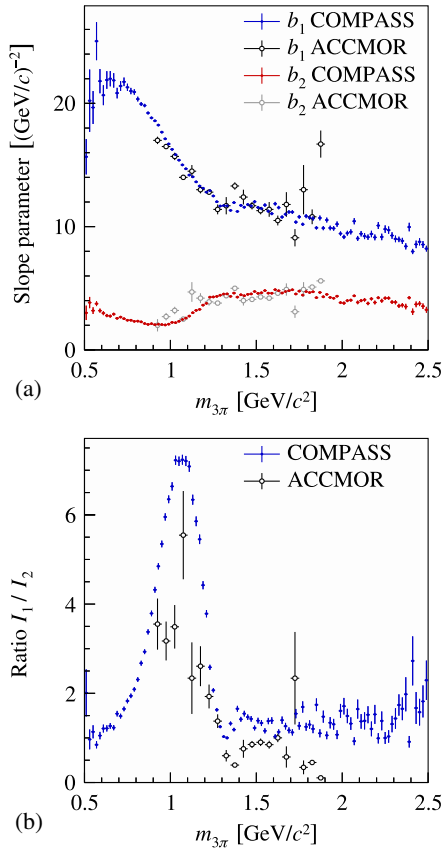


FIG. 31. Result of a fit to the  $t'$  dependence of events from the diffractive-dissociation reaction  $\pi^- + p \rightarrow \pi^- \pi^- \pi^+ + p$ , as measured by COMPASS (filled circles) and by the ACCMOR collaboration [16] (open circles). For each  $m_{3\pi}$  bin, the  $t'$  spectrum was fit using a double-exponential model [see Eq. (44)]. Panel (a) shows the mass dependence of the two slope parameters  $b_1$  (upper points) and  $b_2$  (lower points). Note the extended mass range of the present measurement as compared to the ACCMOR data. Panel (b) shows the ratio  $I_1/I_2$  of the integrated exponential contributions, see Eq. (45).

Here, the  $A_i$  are real-valued parameters. The above formula is not able to describe the behavior of waves that show minima in their  $t'$  distribution.

For each partial wave, one or two specific  $3\pi$  mass ranges are selected, which cover known resonances. However, the  $t'$  dependence of the intensity in these mass ranges still reflects the  $3\pi$  system as a whole in a given partial wave, with both resonant and nonresonant contributions. Bin migration effects due to the limited  $t'$  resolution of the apparatus are not corrected for. However, in the analyzed range the  $t'$  resolution is better than  $0.02$   $(\text{GeV}/c)^2$  (see Sec. II C), which renders the observed  $t'$  spectra only slightly shallower than the true ones.

We perform two kinds of fits: single-slope fits, where the parameter  $A_2$  in Eq. (46) is set to zero, and double-slope fits, where all four parameters are left free. For cases where the  $t'$  spectra exhibit more than one component, the range of the single-slope fits is limited to lower  $t'$  values. Since

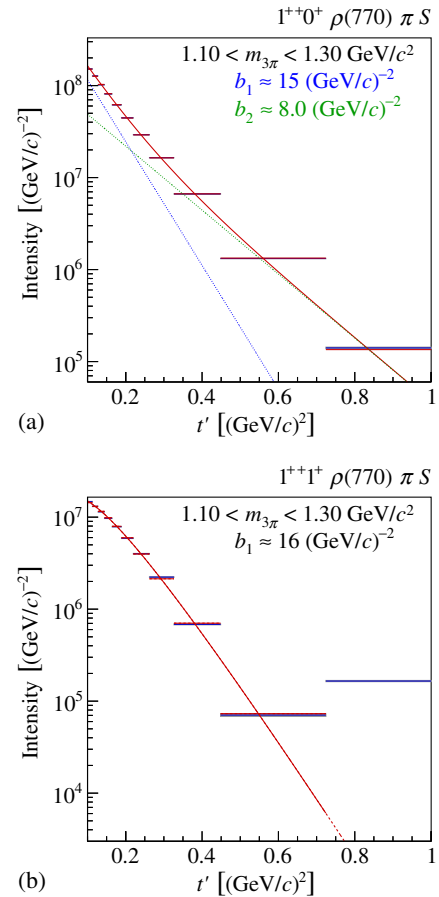


FIG. 32. The  $t'$  dependence of the intensity of the  $1^{++}M^+\rho(770)\pi S$  waves with spin projections  $M=0$  (a) and  $M=1$  (b), integrated over the mass region around the  $a_1(1260)$  as indicated by the shaded regions in Figs. 14(a) and 15(a). The solid red curve in (a) represents a double-exponential fit using Eq. (46), the one in (b) a single-exponential fit with parameter  $A_2=0$ . In (a), the two exponential components are shown by the dotted lines. In (b), the fitted  $t'$  range is indicated by the solid curve; the extrapolation is shown as dashed curve. See text for details.

Eq. (46) is not able to describe the dip structures appearing in some  $t'$  spectra, those distributions are fit only with a single exponential. Details on the fit results are summarized in Tables VI and VII that show the ranges in  $m_{3\pi}$ ,  $t'$  and the resulting slope parameters, the intensity ratio of the two components within the fit range, and the fit quality in terms of  $\chi^2/\text{ndf}$ . It should be noted that  $\chi^2$  is calculated using the integrals of the model function over the respective  $t'$  bins. About half of the spectra require a description with two slopes. For spectra that can be described by a single slope only, the double-slope fit results in a second component having a very small relative weight. For these cases, the values are omitted from Table VII.

Because of the high precision of the data, statistical uncertainties on the extracted slope parameters are negligible and therefore the uncertainties are mostly of

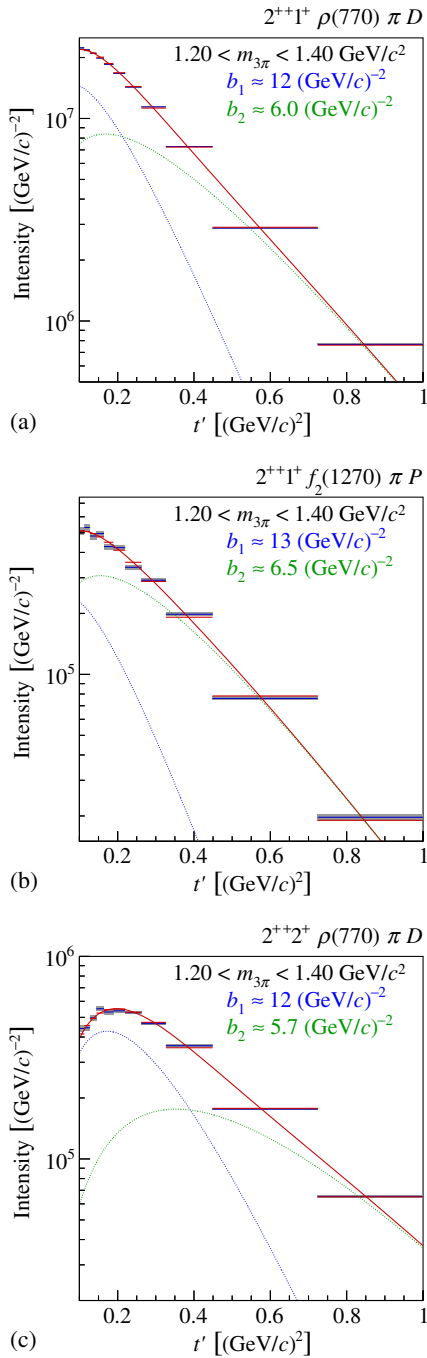


FIG. 33. The  $t'$  dependence of the intensity of three  $2^{++}$  waves with different isobars and different spin-projections  $M$ , integrated over the mass region around the  $a_2(1320)$  as indicated by the shaded regions in Figs. 15(b), 15(c), and 16(a). The solid red curves represent double-exponential fits using Eq. (46); the fit components are shown as dotted curves. See text for details.

systematic nature. The values of the slope parameters depend, among other things, on the choice of boundaries of the mass interval and the fit range in  $t'$ . Given the complex interplay between resonant and nonresonant components, which can only be disentangled later at the stage of the mass-dependent fit [33], we have not attempted

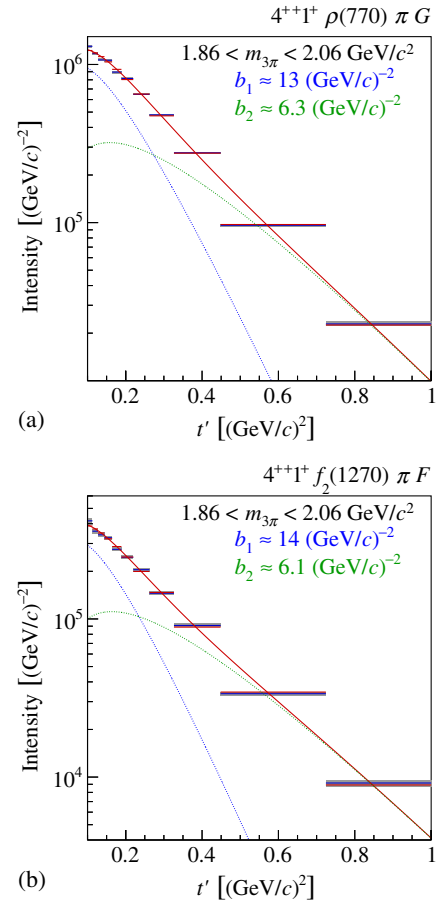


FIG. 34. The  $t'$  dependence of the intensity of the  $4^{++}1^+\rho(770)\pi G$  and  $f_2(1270)\pi F$  waves, integrated over the mass interval around the  $a_4(2040)$  as indicated by the shaded regions in Figs. 15(e) and 15(f). The solid red curves represent double-exponential fits using Eq. (46); the fit components are shown as dotted curves. See text for details.

to quantify the systematic uncertainties. We therefore quote the slope parameters rounded to two-digit precision and do not give the respective uncertainties. In the figures, the fit functions are represented by red curves. For the double-exponential fits, the full  $t'$  range from 0.1 to 1.0  $(\text{GeV}/c)^2$  is used. In contrast, the single-exponential fits are performed using narrower  $t'$  ranges, which are chosen individually for each partial wave and mass region (see Table VI). In this case, the fit ranges are indicated by solid red curves, while the extrapolations to the full  $t'$  range are shown as dashed red curves. In every  $t'$  bin, the integral of the fit function, which enters the  $\chi^2$  function to be minimized, is shown as a red horizontal line, while the blue line represents the data, so that their difference directly indicates the fit quality. For the double-exponential fits, the two components are shown in addition as dotted curves: blue for the steep component and green for the shallow one. In the following, we shall discuss the observed characteristics for each  $J^{PC}$  sector.

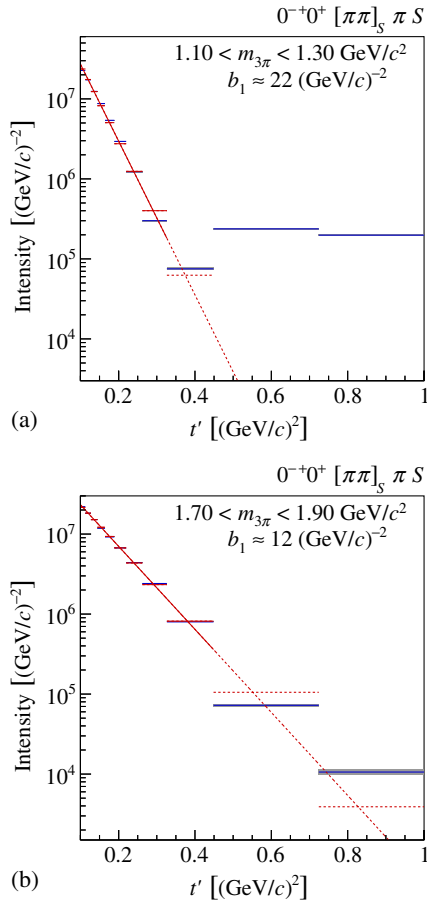


FIG. 35. The  $t'$  dependence of the intensity of the  $0^{-+}0^{+}[\pi\pi]_S\pi S$  wave in two different mass regions, which correspond to the two peaks that are indicated by the shaded bands in Fig. 25(b). The red curves represent single-exponential fits using Eq. (46) with  $A_2 = 0$ . The fitted  $t'$  ranges are indicated by the solid curves; the extrapolations are shown as dashed curves. See text for details.

a.  $J^{PC} = 0^{-+}$ : We study the  $0^{-+}$  waves containing  $f_0(980)$  and  $[\pi\pi]_S$  as isobars. The intensity spectrum of the  $0^{-+}0^{+}[\pi\pi]_S\pi S$  wave shown in Fig. 25(b) exhibits two pronounced maxima and differs strongly from the one for the corresponding wave with a  $f_0(980)$  isobar shown in Fig. 25(a). The higher-lying maximum in the  $[\pi\pi]_S\pi S$  decay mode corresponds to the  $\pi(1800)$  and exhibits a slope parameter of  $b \approx 12$   $(\text{GeV}/c)^{-2}$  [see Fig. 35(b)], similar to that for the  $f_0(980)\pi S$  decay mode. This is in agreement with the expectation that a resonance should have the same slope parameter independent of its decay mode. In both cases, the  $t'$  spectra are purely exponential. In contrast, the  $t'$  spectrum corresponding to the broad structure in the 1.1 to 1.3  $\text{GeV}/c^2$  mass range around the elusive  $\pi(1300)$  exhibits a pronounced intensity minimum around 0.35  $(\text{GeV}/c)^2$  and a second maximum around 0.6  $(\text{GeV}/c)^2$  [see Fig. 35(a)]. This behavior suggests that different production processes are interfering and is similar to predictions by the three-component Deck model [62]. The single-exponential

fit to the low- $t'$  region results in an exceptionally steep slope of  $b \approx 22$   $(\text{GeV}/c)^{-2}$ . The strikingly different  $t'$  dependences of the  $\pi(1300)$  and  $\pi(1800)$  mass regions are further illustrated by Fig. 24 and in Sec. VI C.

b.  $J^{PC} = 1^{++}$ : The mass region around the  $a_1(1260)$  peak contains both resonant and nonresonant contributions, the latter ones dominated by the Deck process. Using a single slope, we obtain  $b \approx 12$   $(\text{GeV}/c)^{-2}$  for the  $a_1(1260)$  region in the  $1^{++}0^{+}\rho(770)\pi S$  wave, a similar value of  $b \approx 13$   $(\text{GeV}/c)^{-2}$  in the  $1^{++}0^{+}[\pi\pi]_S\pi P$  wave [see Fig. 36(a)], and a steeper slope of  $b \approx 16$   $(\text{GeV}/c)^{-2}$  for the  $1^{++}1^{+}\rho(770)\pi S$  wave [Fig. 32(b)]. The  $t'$  distribution of the  $M = 0$  wave is much better described by two slopes with nearly equal intensity [Fig. 32(a)]. The one for the  $M = 1$  wave exhibits a dip at approximately 0.5  $(\text{GeV}/c)^2$ . However, the slope  $b_1$  of the steep component in the double-exponential fit of the  $M = 0$  wave is similar to that of the  $M = 1$  wave extracted using the single-exponential model in the region of lower  $t'$ . If we interpret the

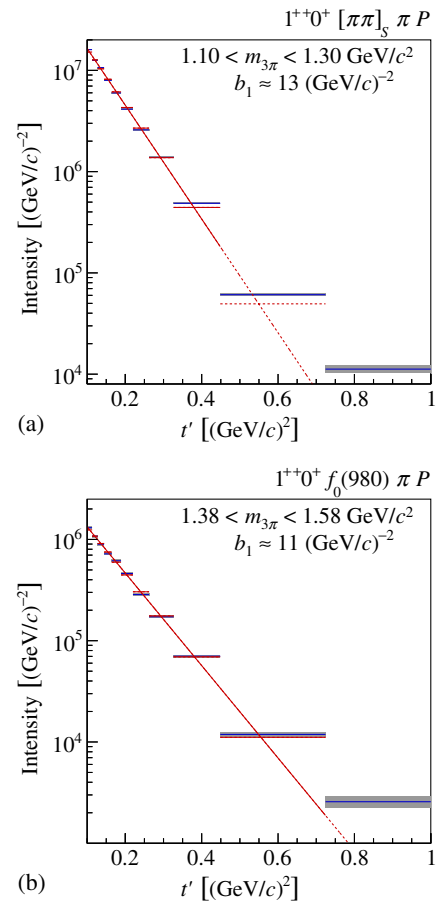


FIG. 36. The  $t'$  dependences of the intensities of the  $1^{++}0^{+}$  waves with  $[\pi\pi]_S$  (a) and  $f_0(980)$  (b) isobars taken around the peak region in the respective wave as indicated by the shaded bands in Figs. 25(e) and 25(f). The red curves represent single-exponential fits using Eq. (46) with  $A_2 = 0$ . The fitted  $t'$  ranges are indicated by the solid curves; the extrapolations are shown as dashed curves. See text for details.

components with the steep slopes to be of nonresonant origin, we would conclude that it contributes about 50% to the  $M = 0$  intensity and that it dominates the  $M = 1$  wave. The intensity around the peak in the  $1^{++}0^+f_2(1270)\pi P$  wave at  $1.8 \text{ GeV}/c^2$  exhibits a nearly single-exponential  $t'$  spectrum with a slope similar to that of the  $a_2(1320)$  and  $a_4(2040)$  regions in the respective  $2^{++}$  and  $4^{++}$  waves. The  $a_1(1420)$  peak in the  $1^{++}0^+f_0(980) \pi P$  wave is well described by a single exponential [see Fig. 36(b)] and has a slope parameter of  $b \approx 11 \text{ (GeV}/c)^{-2}$  similar to that of the  $\pi(1800)$  in the  $0^{-+}$  waves with  $f_0(980)$  and  $[\pi\pi]_S$  isobar. This finding is consistent with a slope parameter of  $b \approx 10 \text{ (GeV}/c)^{-2}$  that was extracted for the  $a_1(1420)$  in a mass-dependent fit [56].

c.  $J^{PC} = 2^{++}$ : The waves containing the  $a_2(1320)$  are best described using two exponentials and show similar behavior regardless of the type of the isobar and the orbital angular momentum  $L$  in the decay. A shallow component with  $b_2 \approx 6 \text{ (GeV}/c)^{-2}$  is accompanied by a steeper component of comparable magnitude with  $b_1 \approx 12 \text{ (GeV}/c)^{-2}$ . Different spin projections  $M$  are equally well described (see Fig. 33). In the  $2^{++}$  waves, the steep components cannot be directly identified with nonresonant contributions, because they are small. It cannot be excluded that the two components are caused by the interference of the low-mass tails of excited  $a_2$  states with the ground state, which may contribute to the  $t'$  spectra with different slopes.

d.  $J^{PC} = 2^{-+}$ : This  $J^{PC}$  is studied in four partial waves containing  $\rho(770)$  and  $f_2(1270)$  isobars and two waves containing  $[\pi\pi]_S$  and  $f_0(980)$  isobars. The latter two show striking interference effects and are discussed further in Sec. VI. The  $t'$  spectra are studied in two different mass intervals: one containing the  $\pi_2(1670)$ , the other the  $\pi_2(1880)$ . The observed pattern is rather irregular. Single-exponential fits yield slope values from about 6 to 11  $(\text{GeV}/c)^{-2}$ . For the mass region around  $\pi_2(1670)$ , the  $t'$  spectra fall into two classes: (i) distributions that are single-exponential or have only small contributions from a second slope [ $2^{-+}0^+\rho(770) \pi F$ ,  $2^{-+}1^+f_2(1270)\pi S$ ,  $2^{-+}0^+f_2(1270) \pi D$ , and  $2^{-+}0^+f_0(980) \pi D$  waves] and (ii) distributions that need two exponentials [ $2^{-+}0^+f_2(1270) \pi S$  and  $2^{-+}0^+[\pi\pi]_S\pi D$  waves]. The latter waves have a shallower component with a slope of around 7  $(\text{GeV}/c)^{-2}$  accompanied by a steep component of similar magnitude. The slopes of the single-exponential spectra vary considerably.

The pattern is different for the  $\pi_2(1880)$  mass region. Here, the  $2^{-+}0^+\rho(770)\pi F$ ,  $2^{-+}0^+f_0(980) \pi D$ , and  $2^{-+}0^+[\pi\pi]_S\pi D$  waves are nearly single-exponential. However, the latter has a steeper slope of 11  $(\text{GeV}/c)^{-2}$  compared to  $b_1 \approx 7 \text{ (GeV}/c)^{-2}$  for the former two. The  $2^{-+}0^+f_2(1270)\pi D$  wave requires two slopes, where the steep slope is about 11  $(\text{GeV}/c)^{-2}$  and the shallow one approximately 5.9  $(\text{GeV}/c)^{-2}$ .

e.  $J^{PC} = 4^{++}$ : The waves containing the  $a_4(2040)$  are studied in decays into two different isobars. The  $t'$  spectra follow the pattern observed for  $J^{PC} = 2^{++}$ , with one slope of  $b_2 \approx 6 \text{ (GeV}/c)^{-2}$  and a steeper component described by  $b_1 \approx 13$  to  $14 \text{ (GeV}/c)^{-2}$  of about equal strength.

In summary, for single-exponential fits of the  $t'$  spectra, we find a general trend of shallower slopes with increasing mass. Waves with dominant resonant contributions, like e.g. the  $2^{++}$  and  $4^{++}$  waves, have slopes in the range from 7 to 11  $(\text{GeV}/c)^{-2}$ , which are equal for different decay modes. In contrast, waves with large nonresonant contributions, like e.g. the  $1^{++}\rho(770)\pi$  waves, show typically steeper slopes in the range of 12 to 16  $(\text{GeV}/c)^{-2}$ . Many waves are better described by a two-exponential model. However, in general the two components do not seem to separate nonresonant from resonant contributions. This may be due to possible large interference effects or contributions from excited states. Signs of such interferences are observed in the  $t'$  spectra of some waves, which exhibit a dip around  $t' \approx 0.3$  to  $0.6 \text{ (GeV}/c)^{-2}$  and thus can be described by the single-exponential function only in a limited  $t'$  interval.

Our results of the fits using single exponentials can to some extent be compared to earlier analyses done on this topic. The single-slope parameters in the mass region around the  $a_2(1320)$  of 7.5 to 8.9  $(\text{GeV}/c)^{-2}$  agree well with the results obtained for the  $\eta\pi^-$  and  $\eta'\pi^-$  channels studied at the same incident energy. In the former channel, which is dominated by the  $a_2(1320)$ , the slope parameter is 8.45  $(\text{GeV}/c)^{-2}$  [51]. In the  $\eta'\pi^-$  channel, a slope parameter of 8.2  $(\text{GeV}/c)^{-2}$  is found in the  $a_2(1320)$  mass region [64]. As in the present case, natural-parity transfer ( $M = 1$ ) is strongly dominant. Hence, all  $a_2(1320)$  production characteristics are consistent with being independent on the decay channels, as required for true resonances. For  $a_4(2040)$  production, the  $3\pi$  and  $\eta'\pi^-$  results (see Table VI and Ref. [64], respectively) are consistent with this requirement as well.

The ACCMOR collaboration [13–16] has pioneered such  $t'$  fits for selected waves in the  $3\pi$  mass region between 0.8 and 1.9  $\text{GeV}/c^2$ , describing the  $t'$  spectra in the range  $t' < 1.0 \text{ (GeV}/c)^2$ . For the  $1^{++}0^+\rho(770)\pi S$  wave, which contains the  $a_1(1260)$ , the authors quote an overall slope parameter of  $b = (10.1 \pm 0.9) \text{ (GeV}/c)^{-2}$ , which is similar to our data. For the  $2^{++}1^+\rho(770) \pi D$  wave, they observe  $b = (7.3 \pm 0.1) \text{ (GeV}/c)^{-2}$  as compared to  $b \approx 8.9 \text{ (GeV}/c)^{-2}$  quoted in Table VI. Finally, for the waves  $2^{-+}0^+f_2(1270) \pi S$  and  $2^{-+}0^+[\pi\pi]_S\pi S$ , they have extracted values of  $b = (8.5 \pm 0.3) \text{ (GeV}/c)^{-2}$  and  $b = (10.7 \pm 1.1) \text{ (GeV}/c)^{-2}$ , respectively, while selecting a mass window from 1.6 to 1.7  $\text{GeV}/c^2$ . Both values are in good agreement with our findings (see Table VI). The authors concluded that owing to strong nonresonant effects, the true values for  $b$  in direct resonance production might be around  $b = 7.5 \text{ (GeV}/c)^{-2}$ . This value agrees with our findings of  $b$  being in the range of 7 to

TABLE VI. Slope parameters  $b_1$  from a single-exponential fit to the  $t'$  spectra in the given  $t'$  ranges. The listed  $m_{3\pi}$  intervals, over which the intensity is integrated, cover the peak regions of the different partial waves.

Partial Wave	$m_{3\pi}$ Range [GeV/ $c^2$ ]	$t'$ Range [(GeV/ $c$ ) $^2$ ]	$b_1$ [(GeV/ $c$ ) $^{-2}$ ]	$\chi^2/\text{ndf}$
$1^{++}0^+\rho(770)\pi S$	[1.10, 1.30]	[0.100, 0.326]	12	120
$1^{++}1^+\rho(770)\pi S$	[1.10, 1.30]	[0.100, 0.724]	16	6.6
$1^{++}0^+f_2(1270)\pi P$	[1.68, 1.88]	[0.100, 1.000]	8.4	4.3
$2^{++}1^+\rho(770)\pi D$	[1.20, 1.40]	[0.100, 0.326]	8.9	37
$2^{++}2^+\rho(770)\pi D$	[1.20, 1.40]	[0.164, 0.724]	8.5	18
$2^{++}1^+f_2(1270)\pi P$	[1.20, 1.40]	[0.127, 0.724]	7.5	5.3
$2^{-+}0^+\rho(770)\pi F$	[1.56, 1.76]	[0.113, 0.724]	9.2	5.1
$2^{-+}0^+f_2(1270)\pi S$	[1.56, 1.76]	[0.100, 0.326]	9.8	30
$2^{-+}1^+f_2(1270)\pi S$	[1.56, 1.76]	[0.113, 0.724]	6.3	3.5
$2^{-+}0^+f_2(1270)\pi D$	[1.56, 1.76]	[0.113, 1.000]	7.8	2.7
$2^{-+}0^+\rho(770)\pi F$	[1.80, 2.00]	[0.113, 0.724]	7.2	3.5
$2^{-+}0^+f_2(1270)\pi D$	[1.80, 2.00]	[0.113, 0.724]	8.4	14
$4^{++}1^+\rho(770)\pi G$	[1.86, 2.06]	[0.164, 0.724]	8.8	25
$4^{++}1^+f_2(1270)\pi F$	[1.86, 2.06]	[0.164, 0.724]	8.4	11
Waves with $f_0(980)$ isobar				
$0^{-+}0^+f_0(980)\pi S$	[1.70, 1.90]	[0.100, 0.724]	11	5.6
$1^{++}0^+f_0(980)\pi P$	[1.38, 1.58]	[0.100, 0.724]	11	2.1
$2^{-+}0^+f_0(980)\pi D$	[1.56, 1.76]	[0.100, 0.724]	8.4	4.2
$2^{-+}0^+f_0(980)\pi D$	[1.80, 2.00]	[0.100, 0.724]	7.3	4.9
Waves with $[\pi\pi]_S$ isobar				
$0^{-+}0^+[\pi\pi]_S\pi S$	[1.10, 1.30]	[0.100, 0.326]	22	55
$0^{-+}0^+[\pi\pi]_S\pi S$	[1.70, 1.90]	[0.100, 0.449]	12	4.1
$1^{++}0^+[\pi\pi]_S\pi P$	[1.10, 1.30]	[0.100, 0.449]	13	11
$2^{-+}0^+[\pi\pi]_S\pi D$	[1.56, 1.76]	[0.100, 0.724]	11	35
$2^{-+}0^+[\pi\pi]_S\pi D$	[1.80, 2.00]	[0.100, 0.724]	11	5.8

11 (GeV/ $c$ ) $^{-2}$  for the  $2^{++}$ ,  $4^{++}$ , as well as for the  $0^{-+}0^+f_0(980)\pi S$  and  $1^{++}0^+f_0(980)\pi P$  waves, which we also ascribe to resonant production.

Results from BNL E852 originate from a mass-independent fit in 12 bins of  $t'$  and are shown in Ref. [19] for the waves  $2^{-+}0^+f_2(1270)\pi S$ ,  $2^{++}1^+\rho(770)\pi D$ ,  $4^{++}1^+\rho(770)\pi G$ , and  $1^{-+}1^+\rho(770)\pi P$  for  $0.1 < t' < 0.5$  (GeV/ $c$ ) $^2$ , but without discussing a functional description of the  $t'$  dependence in detail.

## VI. DETERMINATION OF $\pi\pi S$ -WAVE AMPLITUDES

As shown in Sec. IV D, the  $J^{PC} = 0^{++}$  isobars decaying into  $\pi^-\pi^+$  in an  $S$ -wave are important intermediate states in  $3\pi$  meson decays. In the considered  $3\pi$  mass range, they consist of (i) a broad continuum, which is usually described by a parametrization extracted from  $\pi\pi S$ -wave elastic-scattering data, and (ii) at least two distinct resonances,  $f_0(980)$  and  $f_0(1500)$ . The much debated  $f_0(1370)$  was not included as a separate isobar in the analysis described in Sec. IV. The key issue is: to what extent the information extracted from  $\pi\pi$  elastic scattering can be used to describe spectral shapes and phases of the two-pion  $0^{++}$  isobars in many-body decay amplitudes?

As discussed above, the  $a_1(1420)$  appears only in the  $f_0(980)\pi P$ -wave and its strength (but not its shape) reveals

some dependence on the detailed parametrization used for the  $f_0(980)$ , i.e. a Breit-Wigner or a Flatté amplitude (see Sec. IV F and Appendix B 3). This section addresses in particular the question whether the observed  $a_1(1420)$  is truly related to the narrow  $f_0(980)$  or whether it is an artifact of the isobar parametrizations employed in the fit. This is relevant for the significance of the new observation as well as for the interpretation of the  $a_1(1420)$ .

### A. Method of extracting isobar amplitudes from data

The conventional isobar model uses fixed amplitudes for the description of the  $\pi^-\pi^+$  intermediate states  $\xi$  (see Sec. IV A). However, we cannot exclude that the fit results are biased by the isobar parametrizations used. This is particularly true for the  $0^{++}\pi^-\pi^+$  isobars, where we have separated a broad  $\pi\pi S$ -wave component from the  $f_0(980)$  and  $f_0(1500)$  resonances. In order to solve this problem, a novel method inspired by Ref. [65] was developed. It allows us to determine the overall amplitude of the  $0^{++}\pi^-\pi^+$  isobars directly from the data.

For selected isobars, the new method abandons the fixed description of the mass-dependent amplitudes  $\Delta_\xi(m_\xi)$ , which appear in the two-body isobar decay amplitude of Eq. (8) and are part of the full decay amplitude of the state  $X^-$  defined in Eqs. (11) and (21). The latter amplitude factorizes into a part,  $\mathcal{K}_a^\xi$ , which depends on the spherical angles

TABLE VII. Same as in Table VI, but for the double-exponential fit over the full  $t'$  range of  $0.1 < t' < 1.0$  (GeV/c)<sup>2</sup>. The given intensity ratio is the ratio of the integrals  $I_1/I_2$  of the exponentials with slopes  $b_{1,2}$ . Partial waves with  $t'$  spectra, which exhibit a clear dip structure (marked with †) or which are already well described by a single slope as shown in Table VI (marked by ‡) are not fit with the double-exponential model.

Partial Wave	$m_{3\pi}$ Range	$b_1$	$b_2$	Intensity ratio $I_1/I_2$	$\chi^2/\text{ndf}$
	[GeV/c <sup>2</sup> ]	[(GeV/c) <sup>-2</sup> ]	[(GeV/c) <sup>-2</sup> ]		
$1^{++}0^+\rho(770)\pi S$	[1.10, 1.30]	15	8.0	1.2	6.9
$1^{++}1^+\rho(770)\pi S^\dagger$	[1.10, 1.30]	—	—	—	—
$1^{++}0^+f_2(1270)\pi P^\ddagger$	[1.68, 1.88]	—	—	—	—
$2^{++}1^+\rho(770)\pi D$	[1.20, 1.40]	12	6.0	0.69	7.3
$2^{++}2^+\rho(770)\pi D$	[1.20, 1.40]	12	5.7	1.2	2.2
$2^{++}1^+f_2(1270)\pi P$	[1.20, 1.40]	13	6.5	0.27	3.1
$2^{-+}0^+\rho(770)\pi F^\ddagger$	[1.56, 1.76]	—	—	—	—
$2^{-+}0^+f_2(1270)\pi S$	[1.56, 1.76]	14	7.0	0.71	4.1
$2^{-+}1^+f_2(1270)\pi S^\ddagger$	[1.56, 1.76]	—	—	—	—
$2^{-+}0^+f_2(1270)\pi D^\ddagger$	[1.56, 1.76]	—	—	—	—
$2^{-+}0^+\rho(770)\pi F^\ddagger$	[1.80, 2.00]	—	—	—	—
$2^{-+}0^+f_2(1270)\pi D$	[1.80, 2.00]	11	5.9	1.5	0.47
$4^{++}1^+\rho(770)\pi G$	[1.86, 2.06]	13	6.3	1.1	4.1
$4^{++}1^+f_2(1270)\pi F$	[1.86, 2.06]	14	6.1	0.84	1.9
Waves with $f_0(980)$ isobar					
$0^{-+}0^+f_0(980)\pi S^\ddagger$	[1.70, 1.90]	—	—	—	—
$1^{++}0^+f_0(980)\pi P^\ddagger$	[1.38, 1.58]	—	—	—	—
$2^{-+}0^+f_0(980)\pi D^\ddagger$	[1.56, 1.76]	—	—	—	—
$2^{-+}0^+f_0(980)\pi D^\ddagger$	[1.80, 2.00]	—	—	—	—
Waves with $[\pi\pi]_S$ isobar					
$0^{-+}0^+[\pi\pi]_S\pi S^\dagger$	[1.10, 1.30]	—	—	—	—
$0^{-+}0^+[\pi\pi]_S\pi S^\ddagger$	[1.70, 1.90]	—	—	—	—
$1^{++}0^+[\pi\pi]_S\pi P^\ddagger$	[1.10, 1.30]	—	—	—	—
$2^{-+}0^+[\pi\pi]_S\pi D$	[1.56, 1.76]	16	7.3	1.2	2.5
$2^{-+}0^+[\pi\pi]_S\pi D^\ddagger$	[1.80, 2.00]	—	—	—	—

$\Omega_{\text{GJ}} \equiv (\cos \vartheta_{\text{GJ}}, \phi_{\text{TY}})$  in the Gottfried-Jackson frame as well as  $\Omega_{\text{HF}} \equiv (\cos \vartheta_{\text{HF}}, \phi_{\text{HF}})$  in the helicity frame, and a second part,  $\Delta_a$ , that is the mass-dependent isobar amplitude. Taking into account the Bose symmetrization according to Eq. (12), we write for a particular  $m_{3\pi}$  bin

$$\Psi_a^\epsilon(\tau_{13}, \tau_{23}) = \mathcal{K}_a^\epsilon(\Omega_{13}^{\text{GJ}}, \Omega_{13}^{\text{HF}})\Delta_a(m_{13}) + \mathcal{K}_a^\epsilon(\Omega_{23}^{\text{GJ}}, \Omega_{23}^{\text{HF}})\Delta_a(m_{23}). \quad (47)$$

The two terms represent the two possible  $\pi^-\pi^+$  combinations of the  $\pi_1^-\pi_2^-\pi_3^+$  system. The index  $a$  defined in Eq. (16) represents the quantum numbers of the  $3\pi$  partial wave. This includes the quantum numbers of the  $\pi^-\pi^+$  subsystem  $\xi$ .

In our new *freed-isobar* method, we replace the fixed parametrizations for  $\Delta_a(m_\xi)$  by a set of piecewise constant functions that fully cover the allowed mass range for  $m_\xi$ . The isobar line shape is rewritten as:

$$\Delta_a(m_\xi) = \sum_k \mathcal{F}_{a,k} \Pi_{k,\xi}(m_\xi), \quad (48)$$

where the index  $k$  runs over  $\pi^-\pi^+$  mass bins. These bins are defined by sets of window functions  $\{\Pi_{k,\xi}(m_\xi)\}$  that are nonzero only in a narrow  $m_\xi$  interval in the isobar spectrum given by the bin borders  $\{m_{k,\xi}\}$ :

$$\Pi_{k,\xi}(m_\xi) = \begin{cases} 1 & \text{if } m_{k,\xi} \leq m_\xi < m_{k+1,\xi}, \\ 0 & \text{otherwise.} \end{cases} \quad (49)$$

Here, the bin width  $\delta m_\xi = m_{k+1,\xi} - m_{k,\xi}$  may depend on the mass region of the  $\pi^-\pi^+$  system considered. The  $\mathcal{F}_{a,k}$  are unknown complex numbers that determine the *binned* amplitude  $\Delta_a(m_\xi)$ .

The intensity distribution in a given  $3\pi$  mass bin, as defined in Eq. (24), contains terms of the form

$$\begin{aligned} \mathcal{T}_a^\epsilon \Psi_a^\epsilon(\tau_{13}, \tau_{23}) &= \mathcal{T}_a^\epsilon \left[ \mathcal{K}_a^\epsilon(\Omega_{13}^{\text{GJ}}, \Omega_{13}^{\text{HF}}) \sum_k \mathcal{F}_{a,k} \Pi_{k,\xi}(m_{13}) \right. \\ &\quad \left. + \mathcal{K}_a^\epsilon(\Omega_{23}^{\text{GJ}}, \Omega_{23}^{\text{HF}}) \sum_k \mathcal{F}_{a,k} \Pi_{k,\xi}(m_{23}) \right]. \end{aligned} \quad (50)$$

TABLE VIII. Borders of the four nonequidistant  $t'$  bins, in which the partial-wave analysis with freed isobars is performed. The intervals are chosen such that each bin contains approximately  $11.5 \times 10^6$  events.

Bin	1	2	3	4	
$t'[(\text{GeV}/c)^2]$	0.100	0.141	0.194	0.326	1.000

Absorbing the unknown isobar amplitudes  $\mathcal{T}_{a,k}$  into the transition amplitude  $\mathcal{T}_a^e$  via

$$\mathcal{T}_{a,k}^e \equiv \mathcal{T}_a^e \mathcal{T}_{a,k}, \quad (51)$$

the  $m_\xi$  bins appear in the intensity via the index  $k$  that is summed over coherently, in the same way as the partial-wave index  $a$  is

$$\mathcal{I}(\tau) = \sum_{\varepsilon=\pm 1} \left| \sum_a \sum_k \mathcal{T}_{a,k}^e \Psi_{a,k}^e(\tau_{13}, \tau_{23}) \right|^2 + \mathcal{I}_{\text{flat}}, \quad (52)$$

where

$$\begin{aligned} \Psi_{a,k}^e(\tau_{13}, \tau_{23}) &= \mathcal{K}_a^e(\Omega_{13}^{\text{GJ}}, \Omega_{13}^{\text{HF}}) \Pi_{k,\xi}(m_{13}) \\ &+ \mathcal{K}_a^e(\Omega_{23}^{\text{GJ}}, \Omega_{23}^{\text{HF}}) \Pi_{k,\xi}(m_{23}). \end{aligned} \quad (53)$$

This means that each  $2\pi$  mass bin can be treated like an independent partial wave. In this way, the same procedure as for the standard mass-independent fit can be used. The fits in  $3\pi$  mass bins yield transition amplitudes  $\mathcal{T}_a^e$  that now depend on  $m_{3\pi}$  and  $m_{\pi^-\pi^+}$ . According to Eq. (51), these amplitudes contain information on the  $3\pi$  system as well as on the  $\pi^-\pi^+$  subsystem. It should be noted that the method is restricted to rank 1. Therefore, the rank index was omitted in the above formulas. It was discussed in Sec. IV B that rank 1 is sufficient for the positive-reflectivity waves.

In the ansatz for the decay amplitude in Eq. (47), the isobar mass-dependent amplitude  $\Delta_a(m_\xi)$  depends on the  $3\pi$  partial-wave index  $a$ , i.e. the model permits different isobar amplitudes for different intermediate states  $X^-$ . This is in contrast to the conventional approach, which uses the *same* isobar parametrization in different partial waves.

The reduced model dependence of the new method and the additional information about the  $\pi^-\pi^+$  subsystem lead to a considerable increase in the number of fit parameters in the mass-independent fit. Thus, even for large data sets, the freed-isobar approach can only be applied to a subset of partial waves. In the analysis presented here, we replace the fixed parametrizations of the set of  $J^{PC} = 0^{++}$  isobars, which consists of  $[\pi\pi]_S$ ,  $f_0(980)$ , and  $f_0(1500)$ , by a set of single piecewise constant functions representing the overall dynamical amplitude of all  $0^{++}$  isobars as defined in Eqs. (48) and (49). In the following, we shall denote the freed  $0^{++}$  isobar amplitude by  $[\pi\pi]_{0^{++}}$ .

We determine the  $[\pi\pi]_{0^{++}}$  amplitudes simultaneously for the waves  $0^{-+}0^+[\pi\pi]_{0^{++}}\pi S$ ,  $1^{++}0^+[\pi\pi]_{0^{++}}\pi P$ , and

$2^{-+}0^+[\pi\pi]_{0^{++}}\pi D$ , which are the dominant waves with  $0^{++}$  isobars. These partial waves replace a set of seven waves with conventional isobar parametrizations (see Table IX in Appendix A). For all other amplitudes, we keep the isobar parametrizations as discussed in Sec. IV A. The fits are performed in  $m_{3\pi}$  bins with 40 MeV/ $c^2$  width, i.e. twice as wide as used in the conventional analysis. Each fit results in an Argand diagram for the  $[\pi\pi]_{0^{++}}$  amplitude ranging in the two-pion mass from  $2m_\pi$  to  $m_{3\pi} - m_\pi$ . The bin width in the  $\pi^-\pi^+$  subsystem mass is 40 MeV/ $c^2$ , except for the region  $920 < m_{\pi^-\pi^+} < 1080$  MeV/ $c^2$  around the  $f_0(980)$ .<sup>9</sup> Here, finer bins of 10 MeV/ $c^2$  width are chosen in order to better resolve the resonance structure. In total, 62 two-pion mass bins are used. In order to obtain reasonable statistical accuracy, we perform this analysis in only four bins of  $t'$ , which are listed in Table VIII.

As in the conventional analysis, multiple fit attempts are performed with randomly chosen starting values for the decay amplitudes  $\mathcal{T}_{a,k}^e$  in Eq. (52). Here, the fit with the highest likelihood is selected from a set of 50 attempts. For  $3\pi$  masses below about 1 GeV/ $c^2$ , the fits tend to be trapped in local maxima that deviate from each other only by a few units of log-likelihood. Such a behavior is also observed in the fixed-isobar fits (see Sec. IV F).

## B. Comparison with the fixed-isobar method

In order to compare the new freed-isobar method with the conventional analysis scheme, the fixed-isobar fit was repeated with the coarse binning in  $3\pi$  mass and  $t'$ . Based on this fit, the amplitudes of partial waves with the same  $X^-$  quantum numbers but different  $0^{++}$  isobars, i.e.  $[\pi\pi]_S$ ,  $f_0(980)$ , and  $f_0(1500)$ , are added coherently. For  $J^{PC} = 0^{-+}$ ,  $1^{++}$ , and  $2^{-+}$  of the  $3\pi$  system, the resulting intensities are shown in Fig. 37 as blue data points in two  $t'$  regions chosen as examples. These spectra are related to those in Fig. 25, which show the intensity distributions separately for the  $[\pi\pi]_S$  and  $f_0(980)$  isobars, integrated over the full range of  $t'$ . The striking interference effects observed in the  $2^{-+}0^+ f_0(980) \pi$  and  $[\pi\pi]_S \pi$  isobaric waves are washed out in the coherent sum of the two.

In our novel approach, we do not separate the different  $0^{++}$  isobar components but obtain the overall  $0^{++}$  amplitude in bins of  $m_{\pi^-\pi^+}$  and  $m_{3\pi}$ . This also implies that the correlation of the relative phases between the components

<sup>9</sup>Also the first  $m_{\pi^-\pi^+}$  bin, which covers the mass range from  $2m_\pi$  to 320 MeV/ $c^2$ , has a slightly different width.

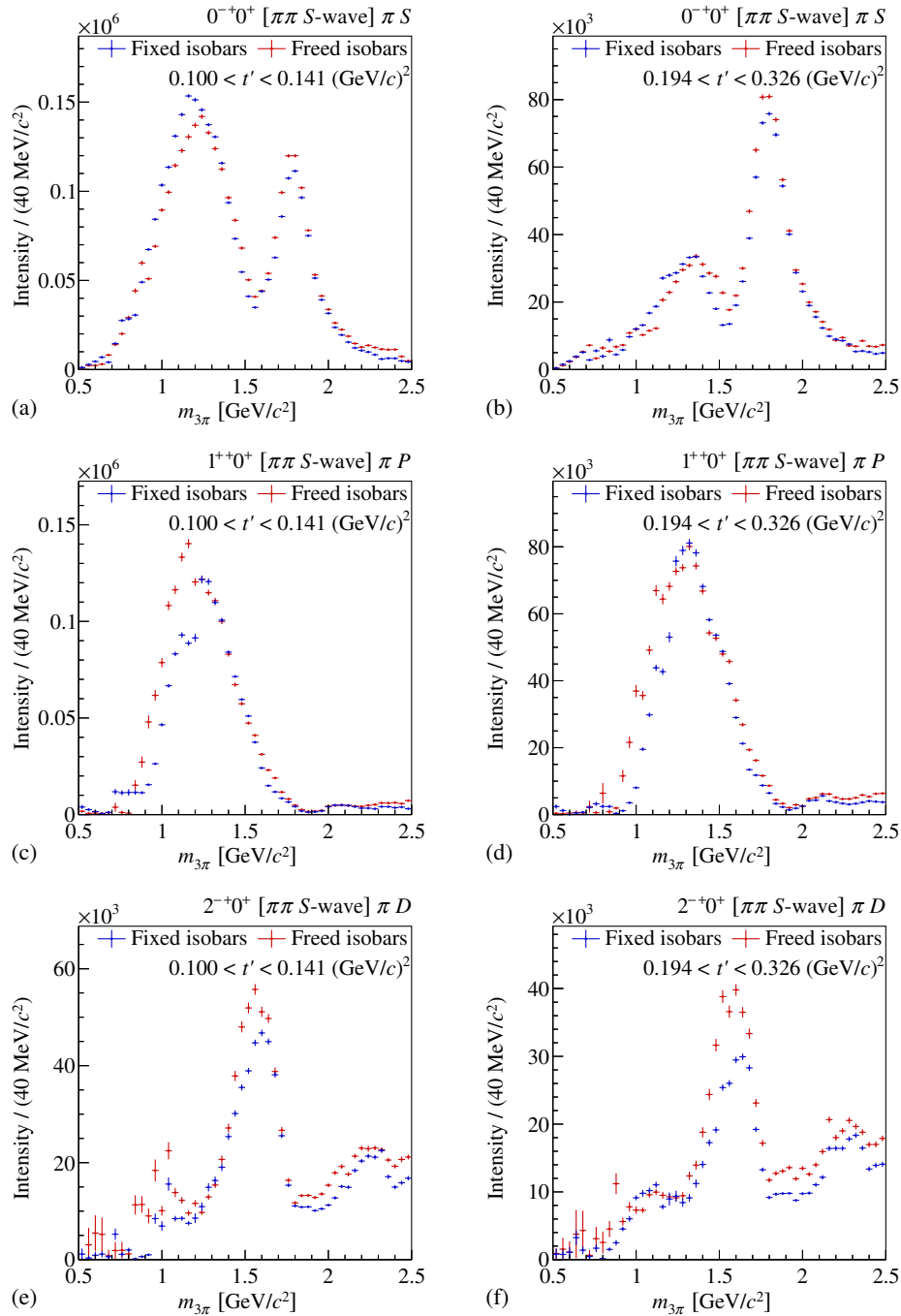


FIG. 37. Intensities of the coherent sum of partial waves with the same quantum numbers but different  $0^{++}$  isobars, as obtained in the conventional analysis scheme with fixed isobar amplitudes (blue), and the corresponding intensities obtained from the freed-isobar fit (red). Left column: low  $t'$ ; Right column: high  $t'$ .

across the  $m_{\pi^-\pi^+}$  spectrum is not predetermined. The red data points in Fig. 37 show the  $3\pi$  mass spectra for  $J^{PC} = 0^{-+}$ ,  $1^{++}$ , and  $2^{-+}$ , obtained by coherently summing over all two-pion mass slices [represented by index  $k$  in Eq. (48)] in the two chosen  $t'$  bins. These intensity distributions can be compared directly to those obtained by coherently summing over the  $0^{++}$  isobars using the conventional analysis method shown as blue data points

in Fig. 37. The agreement is good in general, in particular the  $\pi(1800)$  region in the  $0^{-+}$  wave matches well. In the  $1^{++}$  wave, the region  $m_{3\pi} < 1.2 \text{ GeV}/c^2$  is enhanced in the fit result for the freed isobars except for the highest  $t'$  bin. This is partly due to the fact that waves with freed isobars have no  $3\pi$  mass thresholds in the new fit, whereas in the conventional fit, the  $1^{++}0^+ f_0(980) \pi P$  wave was limited to the region of  $m_{3\pi} > 1180 \text{ MeV}/c^2$

(see Table IX in Appendix A). The largest differences appear in the  $2^{-+}$  wave, where we observe in the freed-isobar fit an increased intensity in the region around the  $\pi_2(1670)$  across all  $t'$  bins. Systematic studies indicate that imperfections in the description of the other isobars used in the PWA fit have an influence on the  $0^{++}$  sector. The agreement between the results of the two methods validates the parametrizations of the  $\pi\pi$   $S$ -wave isobars that are employed in the simpler fixed-isobar fit.

### C. Correlation of $2\pi$ and $3\pi$ mass spectra for freed $\pi\pi$ $S$ -wave isobars

It is instructive to look at the correlation of the  $[\pi\pi]_{0^{++}}$  mass spectrum with the  $3\pi$  mass spectrum in different partial waves. The examples shown in Figs. 38, 39, and 40 are extracted from the  $0^{-+}0^{+}[\pi\pi]_{0^{++}}\pi S$ ,  $1^{++}0^{+}[\pi\pi]_{0^{++}}\pi P$ , and  $2^{-+}0^{+}[\pi\pi]_{0^{++}}\pi D$  waves, respectively. The  $z$  axis of the two-dimensional representations (left columns) is given by  $|\mathcal{T}_a^e(m_{\pi^{-}\pi^{+}}, m_{3\pi})|^2$ , which is normalized such that it can be interpreted as the number of events per unit in  $m_{\pi^{-}\pi^{+}}$ . The apparent dependence of the shape of the  $2\pi$  mass distribution on  $m_{3\pi}$  and on  $J^{PC}$  of the  $3\pi$  system reveals the different coupling of  $3\pi$  resonances to the various  $0^{++}$  components of the  $2\pi$  subsystem. In the following, we will discuss the features for each three-pion  $J^{PC}$  in detail.

a.  $J^{PC} = 0^{-+}$ : In the conventional analysis, the coherent sum of the waves with fixed  $0^{++}$  isobars exhibits two peaks in the intensity that may be identified with the  $\pi(1300)$  and the  $\pi(1800)$ . These two peaks appear very similar in the fit with freed  $0^{++}$  isobars [see Figs. 37(a) and 37(b)]. Since all three pions are in a relative  $S$ -wave in the  $0^{-+}0^{+}[\pi\pi]_{0^{++}}\pi S$  wave, it is very sensitive to nonresonant  $3\pi$  contributions. In particular, in the wave with the fixed  $[\pi\pi]_S$  isobar, the region around  $m_{3\pi} = 1.3$  GeV/ $c^2$  seems to have nonresonant components [see Figs. 24, 25(b), and 35(a)]. Also in the freed-isobar fit, the shape of the  $[\pi\pi]_{0^{++}}$  intensity and its considerable  $t'$  dependence in the  $\pi(1300)$  region suggest this to be mostly nonresonant (see left column of Fig. 38). These observations are in accordance with quark-model calculations for the first radial excitation of the pion [52] which predict a strong suppression of the  $[\pi\pi]_S\pi$  decay mode as compared to  $\rho(770)\pi$ . Apparent enhancements of this wave in the  $\pi(1300)$  region, which were observed in diffractive pion scattering by the VES and BNL E852 experiments [18,20], are consistent with our observations and were attributed to the Deck mechanism [1,52].

In order to study the role of  $f_0(980)$  for the  $0^{-+}$  wave, we sum up the intensity in the mass region  $0.96 < m_{\pi^{-}\pi^{+}} < 1.00$  GeV/ $c^2$ , which contains almost the full  $f_0(980)$  and which is indicated by a pair of red horizontal lines in the left column of Fig. 38. The resulting  $m_{3\pi}$

intensity spectra are shown in the central column of Fig. 38 for the four  $t'$  bins. This simple method does not take into account the interference of the  $f_0(980)$  with the broad  $\pi\pi$   $S$ -wave component. The separation of amplitudes would only be possible by fitting the  $m_{\pi^{-}\pi^{+}}$  and  $m_{3\pi}$  dependences of the amplitudes. The  $m_{3\pi}$  intensity distributions exhibit a clear signal for the  $\pi(1800)$ . In contrast, no clear correlation with a possible  $\pi(1300)$  can be identified. We observe the low-mass structures in  $m_{3\pi}$  to vanish with growing  $t'$ . This indicates the existence of considerable nonresonant contributions in this  $3\pi$  mass region. In a similar way, the role of the  $f_0(1500)$  is investigated by summing the intensity over the range  $1.44 < m_{\pi^{-}\pi^{+}} < 1.56$  GeV/ $c^2$  as indicated by a pair of blue horizontal lines in the left column and shown in the right column of Fig. 38. Again, a clear correlation with the  $\pi(1800)$  is observed.

b.  $J^{PC} = 1^{++}$ : The intensity correlations shown in the left column of Fig. 39 are dominated by a broad maximum between 0.6 and 0.8 GeV/ $c^2$  in  $m_{\pi^{-}\pi^{+}}$ . For increasing  $t'$ , this structure shifts from  $m_{3\pi} = 1.2$  to 1.4 GeV/ $c^2$ , almost reaching the  $a_1(1420)$  region for the highest  $t'$  bin. This behavior suggests the existence of large nonresonant contributions, which obstruct the observation of a possible coupling of the  $a_1(1260)$  to the broad component of the  $\pi\pi$   $S$ -wave. The right column of Fig. 39 shows the intensity summed over the  $f_0(980)$  mass region of  $0.96 < m_{\pi^{-}\pi^{+}} < 1.00$  GeV/ $c^2$ . For all  $t'$  bins, the mass spectra show a clear  $a_1(1420)$  peak and no contribution of the  $a_1(1260)$ . This demonstrates that the observed  $a_1(1420)$  signal in the  $f_0(980)$   $\pi$  channel is not an artifact of the  $0^{++}$  isobar parametrizations used in the conventional analysis method.

c.  $J^{PC} = 2^{-+}$ : The  $2^{-+}$  intensity correlations shown in the left column of Fig. 40 exhibit a vertical band around  $m_{3\pi} = 1.5$  GeV/ $c^2$  [below the  $\pi_2(1670)$ ]. The  $m_{\pi^{-}\pi^{+}}$  distribution peaks below the  $f_0(980)$ . This structure changes its shape and relative strength with  $t'$ . The role of the  $f_0(980)$  and  $f_0(1500)$  isobars is again illustrated by summing the intensities over the respective  $2\pi$  mass ranges, which are shown in the central and right columns of Fig. 40. For both  $\pi^{-}\pi^{+}$  mass regions, we observe a clear signal for the  $\pi_2(1880)$ . The intensity maximum around  $m_{3\pi} = 1.6$  GeV/ $c^2$  in the  $f_0(980)$  slice changes its shape and position with  $t'$ , and hence looks different from the  $\pi_2(1670)$  peak, as it is, for example, observed in the  $f_2(1270)$   $\pi$  decay mode and shown in Figs. 18(a), 18(c), 22(a), and 22(c). In addition, the position of the peak is  $t'$  dependent, which indicates a nonresonant contribution. The VES experiment [20] has reported on an excited  $\pi_2$  resonances at 2.09 GeV/ $c^2$ . It was observed as a 520 MeV/ $c^2$  broad enhancement in the  $[\pi\pi]_S$   $\pi$  and  $f_0(980)$   $\pi$  waves. We also observe a similarly broad structure in the  $3\pi$  system at  $m_{3\pi} \approx 2.2$  GeV/ $c^2$  correlated with a broad bump at  $2\pi$  masses of approximately

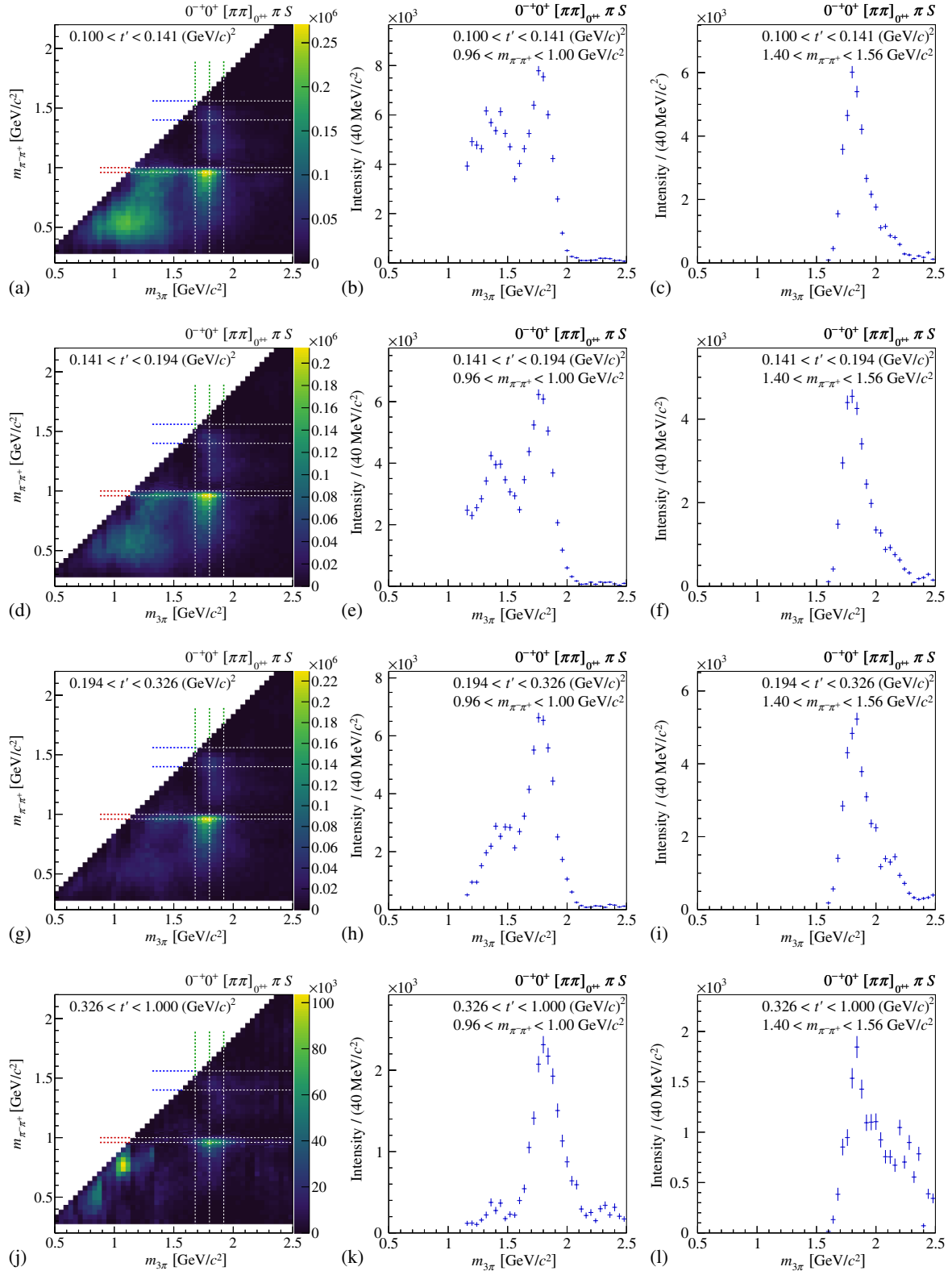


FIG. 38. Intensity of the  $[\pi\pi]_{0^{++}} \pi S$ -wave component of the  $J^{PC} M^e = 0^{-+}0^{+}$  amplitude resulting from the freed-isobar fits in four  $t'$  bins. Left column: two-dimensional representation of the intensity of the  $0^{-+}0^{+}[\pi\pi]_{0^{++}} \pi S$  wave as a function of  $m_{\pi^{-}\pi^{+}}$  and  $m_{3\pi}$ . Central and right columns: intensity as a function of  $m_{3\pi}$  summed over selected  $m_{\pi^{-}\pi^{+}}$  intervals around the  $f_0(980)$  (center) and around the  $f_0(1500)$  (right) as indicated by pairs of horizontal dashed lines in the left column. The vertical dashed lines indicate the centers of the  $m_{3\pi}$  bins discussed in Sec. VID.

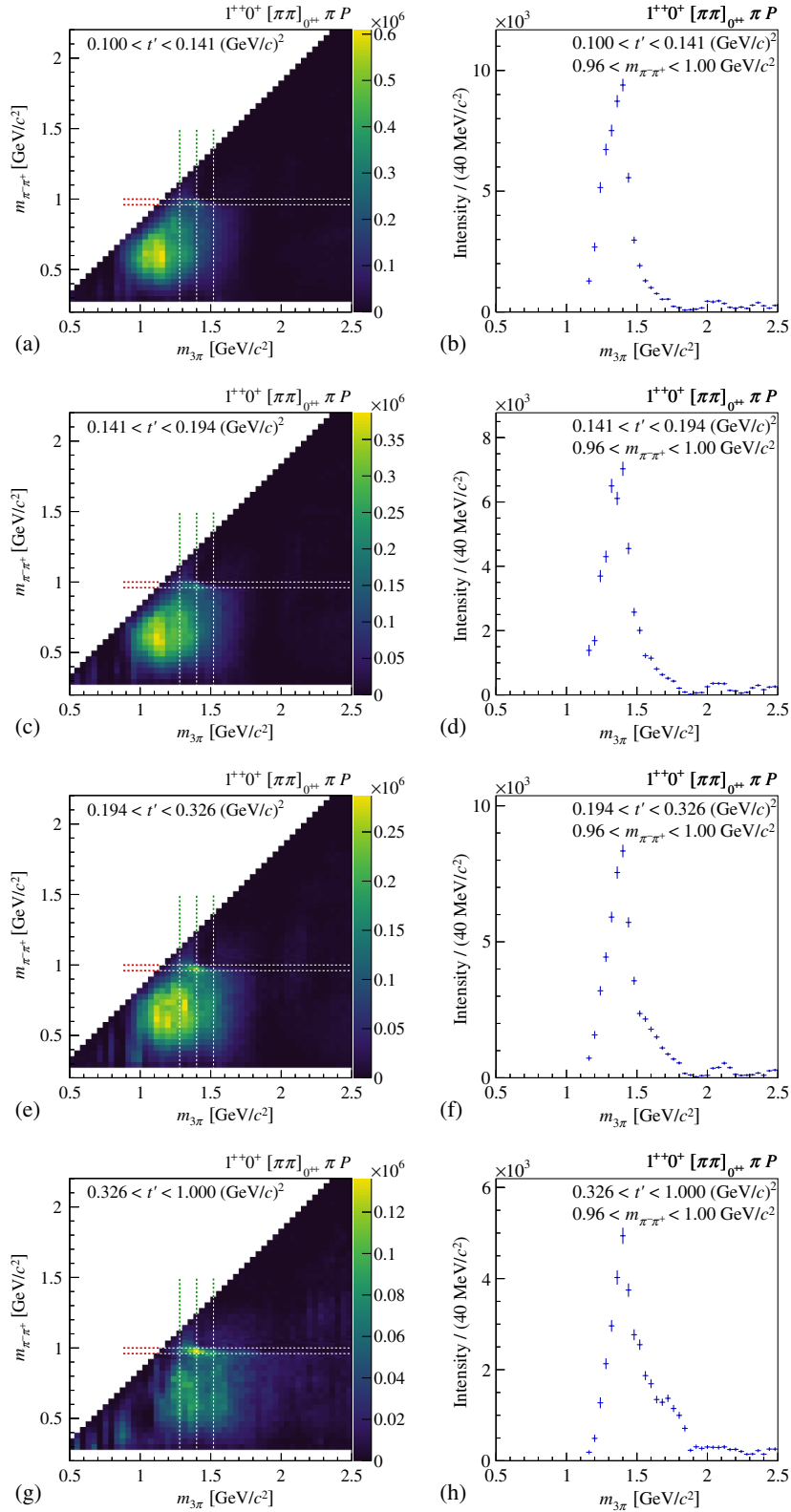
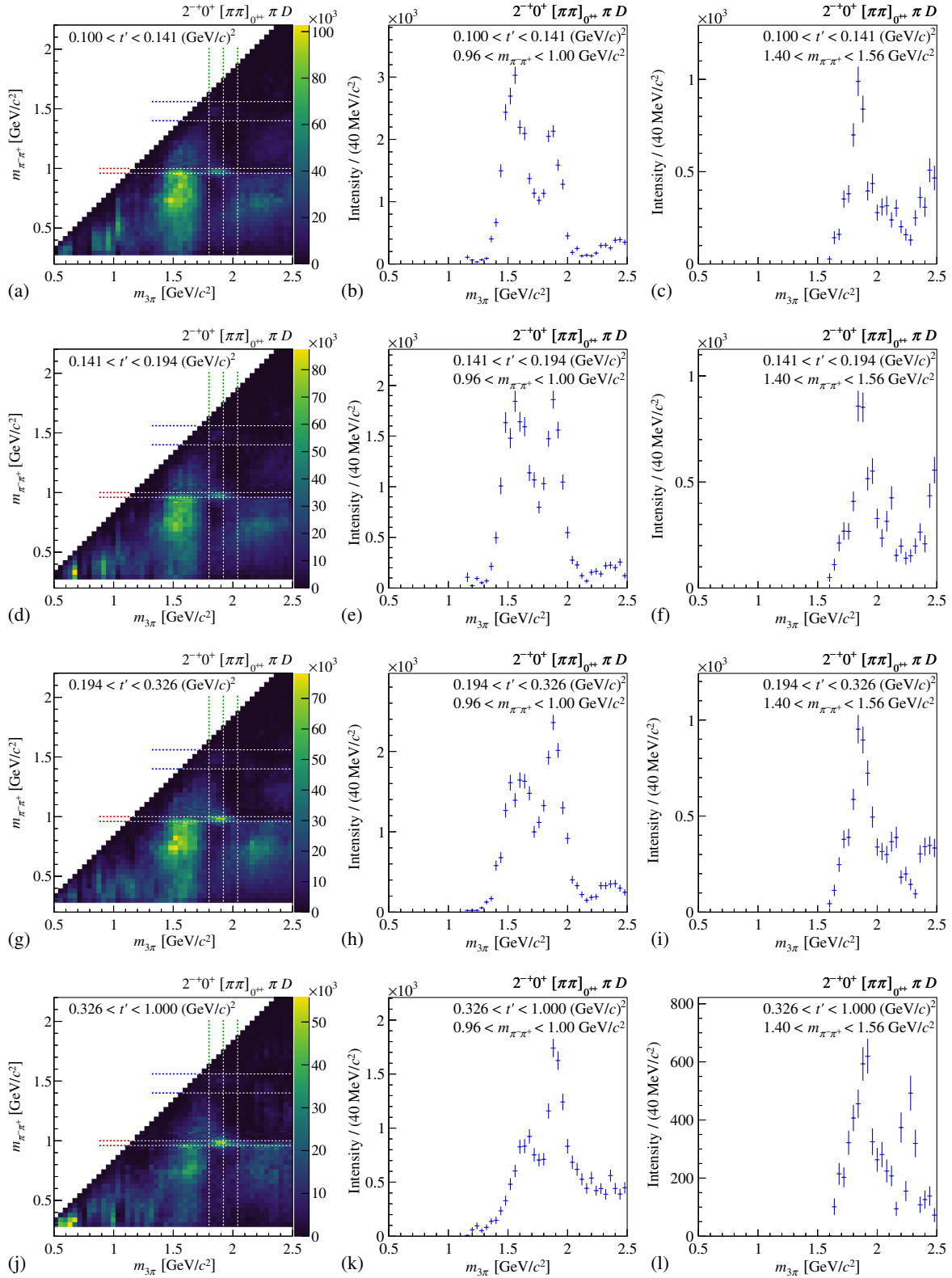


FIG. 39. Same as Fig. 38, but for the  $1^{++}0^+[\pi\pi]_{0^{++}}\pi P$  wave, except that the right column shows the  $m_{\pi^-\pi^+}$  interval around the  $f_0(980)$ .


 FIG. 40. Same as Fig. 38, but for the  $2^{-+}0^{+}[\pi\pi]_{0^{++}}\pi D$  wave.

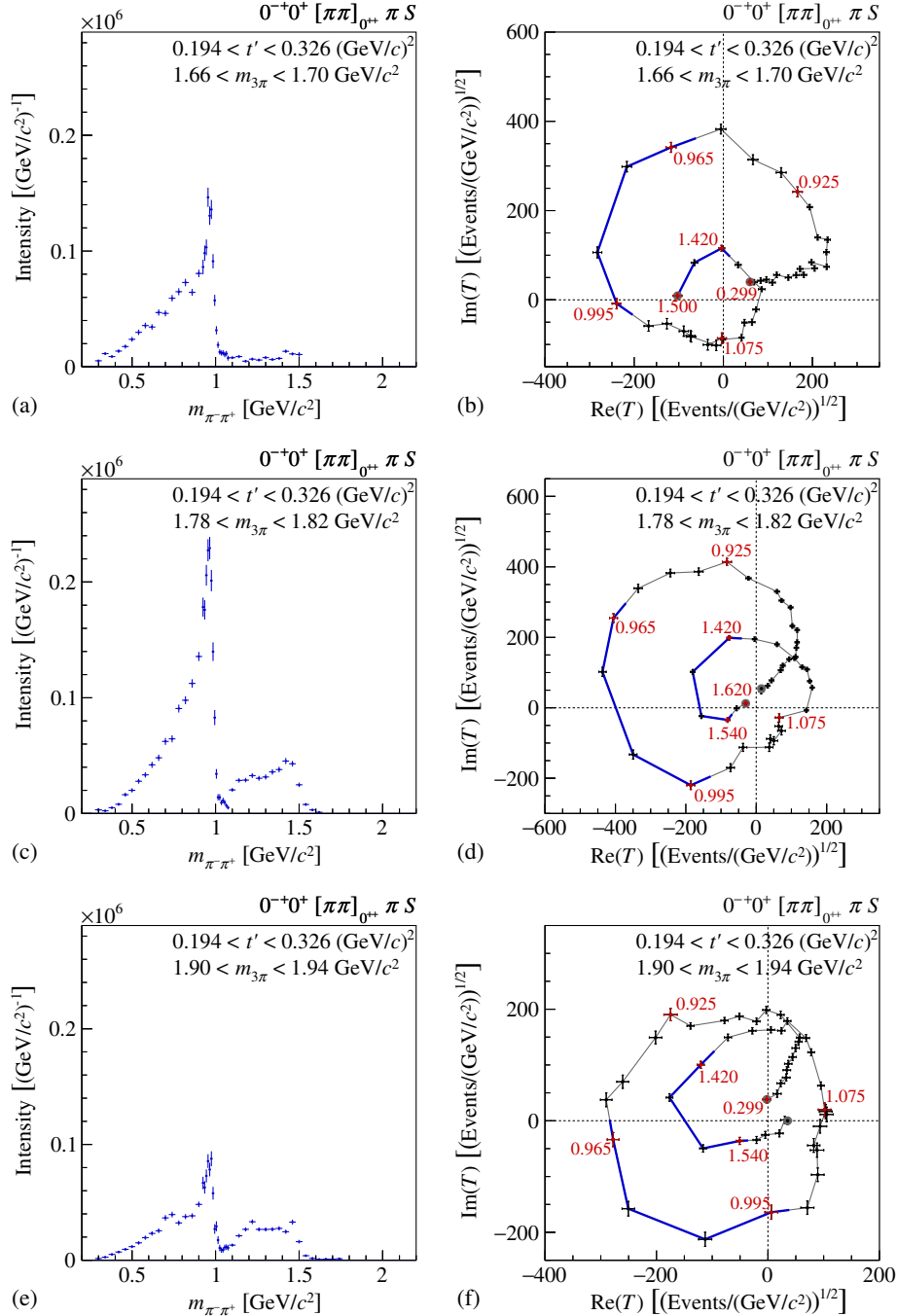
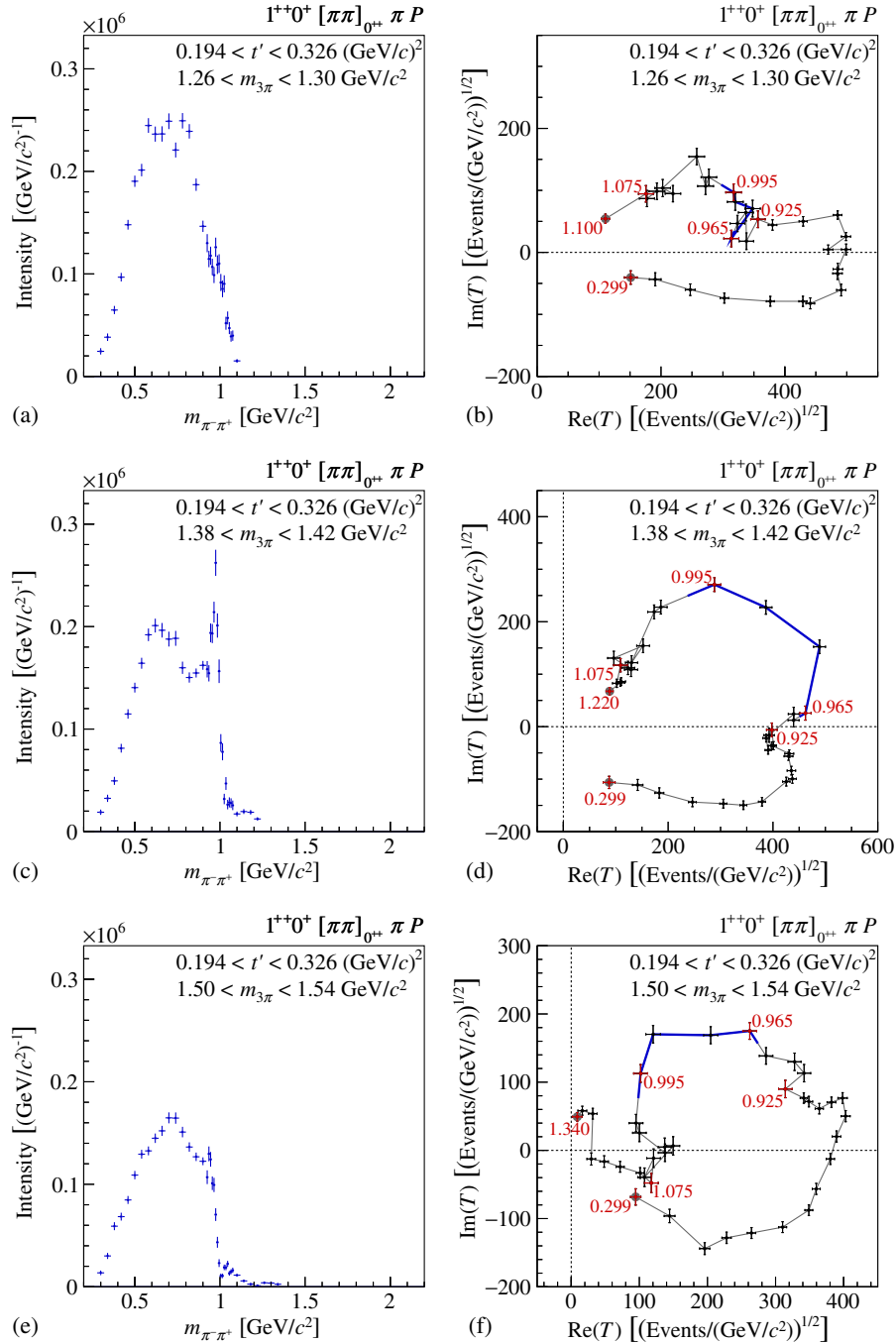


FIG. 41. The freed  $[\pi\pi]_{0^{++}}$  amplitude in the  $0^{-+}0^{+}[\pi\pi]_{0^{++}}\pi S$  wave in the range  $0.194 < t' < 0.326$   $(\text{GeV}/c)^2$  for three intervals in  $m_{3\pi}$ ; below (top row), at (center row), and above the  $\pi(1800)$  (bottom row). Left column: intensities as a function of  $m_{\pi^{-}\pi^{+}}$ ; Right column: Argand diagrams. The crosses with error bars are the result of the mass-independent fit. The numbers in the Argand diagrams show the corresponding mass value of the  $\pi^{-}\pi^{+}$  system. The data points are connected by lines in order to indicate the order. The line segments highlighted in blue correspond to the  $m_{\pi^{-}\pi^{+}}$  ranges around the  $f_0(980)$  from 960 to 1000  $\text{MeV}/c^2$  and, if phase space permits, around the  $f_0(1500)$  from 1400 to 1560  $\text{MeV}/c^2$ . The  $2\pi$  mass is binned in 10  $\text{MeV}/c^2$  wide intervals around the  $f_0(980)$  and in 40  $\text{MeV}/c^2$  wide slices elsewhere. The phase of the Argand diagrams is fixed by the  $1^{++}0^{+}\rho(770)\pi S$  wave.

$750 \text{ MeV}/c^2$ . The shape in  $m_{\pi^{-}\pi^{+}}$  seems to change as a function of  $t'$ . With the present analysis, we cannot confirm the resonance interpretation of this structure. While a corresponding peak is observed around

$m_{3\pi} = 2.2 \text{ GeV}/c^2$  in the conventional fixed-isobar fit in the  $2^{-+}0^{+}f_0(980)\pi D$  wave [see Fig. 25(c)], no pronounced correlation with the  $2\pi$  system in the  $f_0(980)$  mass region is seen in the freed-isobar fit.


 FIG. 42. Same as Fig. 41, but for the  $1^{++}0^+[\pi\pi]_{0^{++}} \pi P$  wave in three  $m_{3\pi}$  bins around the  $a_1(1420)$ .

#### D. Argand diagrams and $2\pi$ mass spectra for freed $\pi\pi$ S-wave isobars

The previous section discussed mainly the correlation of the  $\pi\pi$  S-wave and the  $3\pi$  partial-wave intensities. The two-dimensional transition amplitudes extracted from the data furthermore contain information about the  $m_{3\pi}$  and the  $m_{\pi^-\pi^+}$  dependences of the relative phases. These phases are measured with respect to the  $1^{++}0^+\rho(770) \pi S$  anchor wave as a function of  $2\pi$  mass. They give insight into the composition of the  $\pi\pi$  S-wave amplitude. In order to study

the influence of the  $3\pi$  system, we look at the  $2\pi$  invariant mass spectra for three  $3\pi$  mass bins, chosen below, at, and above clear  $3\pi$  resonance signals. The centers of the  $m_{3\pi}$  bins are indicated by green vertical lines in the left columns of Figs. 38 to 40.

a.  $J^{PC} = 0^{-+}$ : The wave with the freed  $[\pi\pi]_{0^{++}}$  isobar shows a clear signal for the  $\pi(1800)$  coupling to  $f_0(980) \pi$  and  $f_0(1500) \pi$ . The left column of Fig. 41 shows the  $[\pi\pi]_{0^{++}}$  intensity as a function of  $m_{\pi^-\pi^+}$  for three different values of  $m_{3\pi}$ , i.e. below, at, and above the  $\pi(1800)$

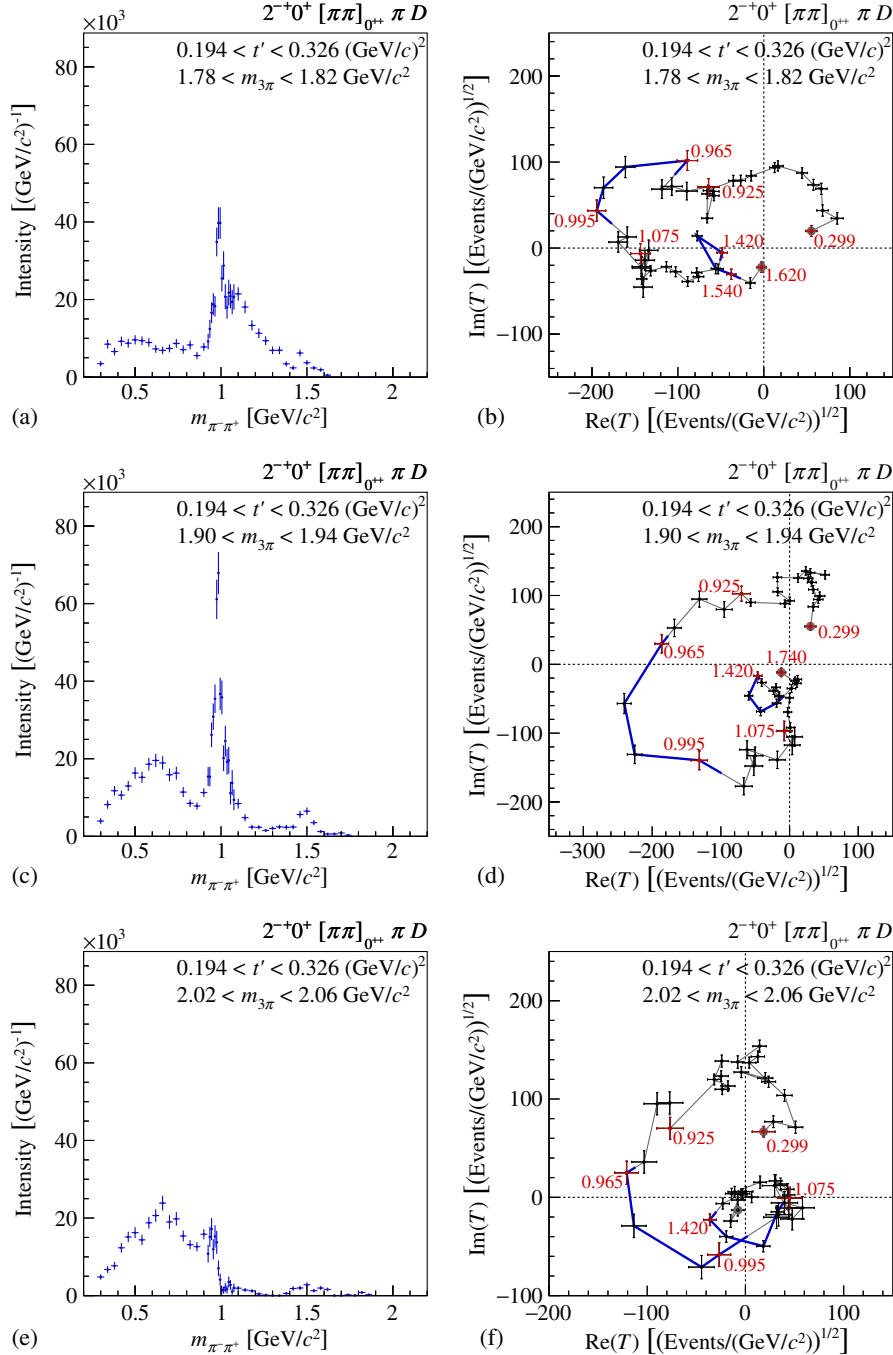


FIG. 43. Same as Fig. 41, but for the  $2^{-+}0^{+}[\pi\pi]_{0^{++}}\pi D$  wave in three  $m_{3\pi}$  bins around the  $\pi_2(1880)$ .

resonance for the region of larger  $t'$ , where the resonance signal is clearer. The three  $m_{\pi^{-}\pi^{+}}$  spectra are similar. We observe prominent signals for  $f_0(980)$ . Because of phase space, the  $f_0(1500)$  peak appears only in the two higher  $3\pi$  mass intervals. The enhancement of both states relative to the broad  $\pi\pi$   $S$ -wave component is strongest at the  $\pi(1800)$  mass. The right column of Fig. 41 shows the corresponding Argand diagrams measured with respect to the  $1^{++}0^{+}\rho(770)\pi S$  wave. For a fixed mass of the  $3\pi$  system, the Argand diagram describes magnitude and phase of the

$2\pi$  amplitude. The phase of the  $[\pi\pi]_{0^{++}}$  amplitude spans nearly two full circles about the origin in the  $2\pi$  mass range from threshold to about  $1.6\text{ GeV}/c^2$ . This reflects the resonance character of the  $f_0(980)$  and  $f_0(1500)$ . The positions of  $f_0(980)$  and  $f_0(1500)$  (marked by the blue line segments in the Argand diagrams) rotate counterclockwise with increasing  $m_{3\pi}$ , reflecting the growing phase of the resonance. We conclude a clear coupling of  $\pi(1800)$  to both  $f_0$  states, which is more pronounced than that to the broad component of the

$\pi\pi$  S-wave. There is no evidence for the  $f_0(1370)$  in this wave. The observed behavior of the  $[\pi\pi]_{0^{++}}$  phases corroborates the conclusions drawn from the intensity correlations in Fig. 38. In the  $\pi(1800)$  region, the gross features of the  $[\pi\pi]_{0^{++}}$  phase motion are similar to those observed by the *BABAR* experiment in the  $2\pi$  subsystem of  $D_s^+ \rightarrow \pi^+\pi^-\pi^+$  decays [66]. Differences in details are probably due to different nonresonant contributions in the two processes.

b.  $J^{PC} = 1^{++}$ : In this wave, the  $a_1(1420)$  region is most interesting. The extracted  $[\pi\pi]_{0^{++}}$  intensities are shown in the left column of Fig. 42 for three different values of  $m_{3\pi}$  in a similar way as explained above. For  $m_{3\pi}$  values around  $1.4 \text{ GeV}/c^2$ , a signal for the  $f_0(980)$  appears sitting above a broad  $\pi\pi$  S-wave structure. The complicated shape of the  $\pi^-\pi^+$  amplitude is again illustrated by the Argand diagrams shown in the right column of Fig. 42. Here, the  $f_0(980)$  contribution can be identified by the semicircle-like structure with a shifted origin, which appears at the  $a_1(1420)$  resonance. Comparing Figs. 42(d) and 42(f), a significant counterclockwise rotation of this structure by about  $90^\circ$  with respect to its center is observed above the  $a_1(1420)$ . This confirms the resonance interpretation of the  $a_1(1420)$  in the  $f_0(980) \pi$  decay. For  $m_{\pi^-\pi^+} < 0.8 \text{ GeV}/c^2$ , the amplitude does not change much with respect to  $m_{3\pi}$ . As a consequence, the relative phase of the  $f_0(980)$  component with respect to the broad  $\pi\pi$  S-wave structure also changes by about  $90^\circ$ . Hence the interference pattern changes from partly constructive at the  $a_1(1420)$  to partly destructive at the higher  $m_{3\pi}$  bin. This results in a sharp drop of the intensity in the  $2\pi$  mass spectrum above the  $f_0(980)$ , which is followed by low intensity at higher  $m_{\pi^-\pi^+}$ .

c.  $J^{PC} = 2^{-+}$ : The clearest signal in this wave is the  $\pi_2(1880)$  that couples to  $f_0(980) \pi$  and  $f_0(1500) \pi$ . We again study the  $2\pi$  subsystem in three  $3\pi$  mass regions. The intensity distributions and Argand diagrams are shown in Fig. 43. Also here we find semicircle-like structures with shifted origin that correspond to the  $f_0(980)$ , which is observed as a clear peak in the corresponding  $m_{\pi^-\pi^+}$  distributions. At higher values of  $m_{\pi^-\pi^+}$ , we observe an indication of another small circular structure in the Argand diagram, which is correlated with a rise of the intensity in the  $2\pi$  mass distribution attributable to  $f_0(1500)$ . The shape of the broad  $\pi\pi$  S-wave component at low  $2\pi$  masses is somewhat different from that of the other waves, exhibiting more intensity close to the threshold.

## VII. SUMMARY AND CONCLUSIONS

We have presented a detailed partial-wave analysis based on the world's currently largest data set of the exclusive  $\pi^-\pi^-\pi^+$  final state from diffractive pion scattering off a proton target. The PWA was performed independently in 100 bins of the  $3\pi$  mass  $m_{3\pi}$ , each of which was subdivided into eleven slices of the reduced four-momentum transfer

squared  $t'$ . We refer to this as *mass-independent fit*. It is based on the largest wave set used so far in a PWA of this final state, which contains in total 80 waves with positive reflectivity, 7 with negative reflectivity, and one incoherent isotropic wave representing three uncorrelated pions (see Sec. IV B and Table IX in Appendix A). In this paper, a subset of 18 partial waves with positive reflectivity accounting for 75.8% of the total intensity was studied in detail.

From the study of the general characteristics of partial-wave intensities, two classes of waves can be identified: for some waves, the shape of the mass spectrum shows little dependence on  $t'$  [see e.g. Figs. 17(b) and 17(d)], while for others moderate [see e.g. Figs. 18(a) and 18(c)] or even large variations [see e.g. Figs. 17(a) and 17(c)] are seen. These variations indicate the presence of weak or strong nonresonant contributions that do interfere with the resonant components and may have a characteristically different dependence on  $t'$ . Among the stable waves, where the peak positions do not significantly depend on  $t'$ , we find:

- (i)  $0^{-+}0^+ f_0(980) \pi S$
- (ii)  $1^{++}0^+ f_0(980) \pi P$
- (iii)  $2^{++}1^+ \rho(770) \pi D$
- (iv)  $2^{++}2^+ \rho(770) \pi D$
- (v)  $2^{-+}1^+ f_2(1270) \pi S$
- (vi)  $2^{-+}0^+ f_2(1270) \pi D$
- (vii)  $4^{++}1^+ \rho(770) \pi G$
- (viii)  $4^{++}1^+ f_2(1270) \pi F$

The following waves show significant peak shifts or large variations of the shapes of their mass distribution as a function of  $t'$ :

- (i)  $0^{-+}0^+ [\pi\pi]_S \pi S$
- (ii)  $1^{++}0^+ [\pi\pi]_S \pi P$
- (iii)  $1^{++}0^+ \rho(770) \pi S$
- (iv)  $1^{++}1^+ \rho(770) \pi S$
- (v)  $1^{++}0^+ f_2(1270) \pi P$
- (vi)  $2^{++}1^+ f_2(1270) \pi P$
- (vii)  $2^{-+}0^+ [\pi\pi]_S \pi D$
- (viii)  $2^{-+}0^+ \rho(770) \pi F$
- (ix)  $2^{-+}0^+ f_0(980) \pi D$
- (x)  $2^{-+}0^+ f_2(1270) \pi S$

In the subset of 18 waves, clear resonance peaks are found in the partial-wave intensities of the following decay modes:

- (i)  $\pi(1800) \rightarrow f_0(980) \pi S$ -wave
- (ii)  $\pi(1800) \rightarrow [\pi\pi]_S \pi S$ -wave
- (iii)  $a_1(1260) \rightarrow \rho(770) \pi S$ -wave
- (iv)  $a_1(1420) \rightarrow f_0(980) \pi P$ -wave
- (v)  $a_2(1320) \rightarrow \rho(770) \pi D$ -wave
- (vi)  $\pi_2(1670) \rightarrow f_2(1270) \pi S$ -wave
- (vii)  $\pi_2(1880) \rightarrow f_2(1270) \pi D$ -wave
- (viii)  $a_4(2040) \rightarrow \rho(770) \pi G$ -wave
- (ix)  $a_4(2040) \rightarrow f_2(1270) \pi F$ -wave

The new  $a_1(1420)$ , which was presented in Ref. [56], is only seen in the  $1^{++}0^+f_0(980)\pi P$  wave. No evidence for a corresponding resonance structure is observed in  $1^{++}0^+[\pi\pi]_S\pi P$ , nor in waves containing other isobars. The  $\pi_2(1670)$  and  $\pi_2(1880)$  seem to have different couplings to various decay modes. A peak attributable to the  $\pi_2(1670)$  appears, for example, dominantly in  $2^{-+}0^+f_2(1270)\pi S$ , while a  $\pi_2(1880)$  peak is dominant in  $2^{-+}0^+f_2(1270)\pi D$ . Both states seem to couple to the  $2^{-+}0^+\rho(770)\pi F$  wave, however, with different apparent strength as a function of  $t'$ . In turn, only the  $\pi_2(1880)$  shows a clear coupling to the  $f_0(980)\pi$  decay mode. The shape of the structure observed in this decay mode around  $m_{3\pi} = 1.6 \text{ GeV}/c^2$  changes as a function of  $t'$  (see Sec. VIC).

a.  *$t'$  dependences* We have investigated the production characteristics of the  $\pi^-\pi^-\pi^+$  final state by studying the  $t'$  dependence for the overall data sample as a function of  $m_{3\pi}$  as well as for individual partial-wave intensities in  $3\pi$  mass regions around known resonances. The fits to the overall  $t'$  spectra require two exponential functions in order to describe the fall-off with  $t'$  [see Figs. 30(c) and 30(d)]. The slopes of the two exponentials and their relative contributions change with increasing  $3\pi$  mass, leveling off for  $m_{3\pi} \gtrsim 1.3 \text{ GeV}/c^2$  (see Fig. 31).

The slope parameters for individual waves in  $3\pi$  mass regions around resonances exhibit a complex pattern. Qualitatively, mass regions with strong nonresonant contributions are characterized by a steep drop-off with  $t'$  and thus larger values for the slope parameter up to  $22 (\text{GeV}/c)^{-2}$ . Considerable deviations from the single-exponential behavior are observed for mass regions around the  $\pi(1300)$  in the  $0^{-+}0^+[\pi\pi]_S\pi S$  wave and around the  $a_1(1260)$  in  $1^{++}1^+\rho(770)\pi S$ . In these two waves, we find a minimum of the intensity at values of  $t'$  of about  $0.4 (\text{GeV}/c)^2$  [Fig. 35(a)] and  $0.6 (\text{GeV}/c)^2$  [Fig. 32(b)], respectively, which may be attributed to interference effects of different production processes. Other distributions can be described well by only a single exponential, a parametrization also employed for the fit of the low- $t'$  region in the case of dip structures. Mass regions dominated by resonances show typically a shallower drop-off with slope parameters between 7 and  $11 (\text{GeV}/c)^{-2}$ . However, these regions are often better described by a double-exponential model. Hence the observation of a steep component does not exclude a dominant resonant contribution.

For mass regions with clear resonance signals, e.g.  $a_2(1320)$  and  $a_4(2040)$ , slope parameters are found to be similar for different waves belonging to the same  $J^{PC}$ , even with different spin projections  $M$ . We have studied the production of waves with  $J^{PC} = 1^{++}$ ,  $2^{-+}$ , and  $2^{++}$  with different  $M$ . We observe a reduction in their production rate by about an order of magnitude with every unit of  $M$ . For the  $a_2(1320)$ , the intensity ratio for the two spin projections is in good agreement with the one observed in the  $\eta\pi^-$  decay channel [51]. At the same time, we confirm that the  $t'$

dependences follow the theoretically expected suppression factor  $(t')^M$  at small values of  $t'$  for  $M = 0, 1$ , and 2 (see Figs. 32 and 33). This observation points to the spin characteristics of the Pomeron exchange, which is dominant here.

The  $1^{++}0^+f_0(980)\pi P$  wave is of particular interest. In the mass region of the new  $a_1(1420)$ , this wave exhibits a nearly exponential  $t'$  spectrum with a slope parameter of about  $11 (\text{GeV}/c)^{-2}$ , which is similar to that of the  $\pi(1800)$  in the same decay mode. This supports the resonance interpretation of the  $a_1(1420)$  signal. The slope is in agreement with the slope parameter of about  $10 (\text{GeV}/c)^{-2}$  that was extracted for the  $a_1(1420)$  in a mass-dependent fit [56].

The  $2^{-+}$  waves show no clear pattern. Single-exponential fits in different decay modes around the  $\pi_2(1670)$  and  $\pi_2(1880)$  give slope values between 6 and  $11 (\text{GeV}/c)^{-2}$ . For those  $2^{-+}$  waves that are better described by two exponentials, the dominant slope has a similar range.

b.  *$\pi\pi S$ -wave amplitudes* For the first time, a detailed study of the amplitude of the  $\pi^-\pi^+$   $S$ -wave isobar with  $I^G J^{PC} = 0^+0^{++}$  in the decay of the  $\pi^-\pi^-\pi^+$  system was performed. This was achieved by using the *freed-isobar* technique (see Sec. VI). The  $2\pi$  amplitudes are extracted independently for different  $3\pi$  partial waves in each bin of  $m_{3\pi}$  and  $t'$ . We have presented the correlations of the intensities of the independent freed  $\pi^-\pi^+$  isobar amplitudes with those of the  $3\pi$  system for  $0^{-+}$ ,  $1^{++}$ , and  $2^{-+}$  three-pion  $J^{PC}$  quantum numbers. These correlations reveal a selective coupling of  $3\pi$  resonances to the scalar isobars  $f_0(980)$  and  $f_0(1500)$  and less clear correlations with a broad  $\pi\pi S$ -wave component. The new method does not only yield the two-dimensional intensity distribution, but also provides information about the full  $2\pi$  amplitude for each  $m_{3\pi}$  bin. In the corresponding Argand diagrams, signals for  $f_0(980)$  and  $f_0(1500)$  show up as semicircular structures with rapid counter-clockwise motion with increasing  $m_{\pi^-\pi^+}$ . In the three waves studied, there is no evidence for a distinct  $f_0(1370)$  resonance in the  $\pi^-\pi^+$  subsystem.

For  $J^{PC} = 0^{-+}$  and  $1^{++}$  of the  $3\pi$  system, the  $m_{3\pi}$  spectra connected to the broad component of the  $\pi\pi S$ -wave show enhancements around  $m_{3\pi} = 1.2 \text{ GeV}/c^2$ , which might naïvely be interpreted as  $a_1(1260)$  and  $\pi(1300)$ , respectively. These structures significantly change their shape as a function of  $t'$ , thereby suggesting that they are influenced by nonresonant processes. For the  $\pi(1800)$ , we observe a coupling to  $f_0(980)\pi$  and a somewhat weaker one to  $f_0(1500)\pi$ . The Argand diagram shows clear semicircular structures corresponding to the  $f_0(980)$  and  $f_0(1500)$ . Similarly, in the  $2^{-+} 3\pi$  wave, the coupling of the  $\pi_2(1880)$  to  $f_0(980)\pi$  and  $f_0(1500)\pi$  is seen. For the  $3\pi$  wave with  $J^{PC} = 1^{++}$ , we observe a clear correlation of the  $f_0(980)$  isobar with the new  $a_1(1420)$  resonance [56] in all bins of  $t'$ . This is in contrast to the broad component of the  $\pi\pi S$ -wave, which shows a strongly  $t'$ -dependent

correlation with  $m_{3\pi}$  and a shift of the intensity maximum towards higher values of  $m_{3\pi}$  with increasing  $t'$ . A possible explanation of this shift is the Deck process. At large values of  $t'$ , the rapidity gap between the  $[\pi\pi]_S$  system and the bachelor pion is increased (see Fig. 19), which leads to higher  $3\pi$  masses. The shift of intensity across the  $3\pi$  mass spectrum with  $t'$  could explain the complicated behavior of some  $t'$  spectra (see Sec. V).

Based on the analysis described in this paper, we extracted the properties of resonances and of nonresonant contributions as well as their production characteristics, which will be described in detail in a forthcoming paper [33].

### ACKNOWLEDGMENTS

We have received many suggestions and input during a series of PWA workshops: a joint COMPASS-JLab-GSI Workshop on Physics and Methods in Meson Spectroscopy (Garching/2008), Workshops on Spectroscopy at COMPASS held 2009 and 2011 in Garching, and in the context of the ATHOS workshop series (Camogli/2012, Kloster Seeon/2013, and Ashburn/2015). We are especially indebted to V. Mathieu, W. Ochs, J. Pelaez, M. Pennington, and A. Szczepaniak for their help and suggestions. S. U. Chung would like to thank the Technische Universität München IAS at the TU München and together with D. Ryabchikov the Excellence Cluster “Universe” for supporting many visits to Munich during the last years. We gratefully acknowledge the support of the CERN management and staff as well as the skills and efforts of the technicians of the collaborating institutions. This work is supported by Ministry of Education, Youth, and Sports, Czech Republic; “HadronPhysics2” Integrating Activity in FP7 (European Union); Commissariat à l’Énergie Atomique et aux Énergies Alternatives, Physique des 2 Infinis (Consortium d’Intérêt Scientifique en Ile de France), France and Agence Nationale de la Recherche, France; Bundesministerium für Bildung und Forschung, Germany, Deutsche Forschungsgemeinschaft, Germany, cluster of excellence “Origin and Structure of the Universe”, the computing facilities of the Computational Center for Particle and Astrophysics (C2PAP), Technische Universität München, Institute for Advanced Study, Germany, and Humboldt foundation (Germany); Steel Authority of India Limited (Community Social Responsibility), India and B. Sen fund (India); The Israel Academy of Sciences and Humanities, Israel; Istituto Nazionale di Fisica Nucleare, Italy; Ministry of Education, Culture, Sports, Science and Technology, Japan, Japan Society for the Promotion of Science, Japan, Daiko, and Yamada Foundations (Japan); Narodowe Centrum Nauki, Poland; Fundação para a Ciência e a Tecnologia, Portugal; European Organization for Nuclear Research, Geneva, Switzerland-Russian Foundation for Basic Research, Russia and Presidential Grant NSh-999.2014.2 (Russia).

TABLE IX. Wave set used for mass-independent fit: 80 waves with positive reflectivity, 7 with negative, plus an incoherent isotropic wave.

$J^{PC}M^e$	Isobar	$L$	Threshold [MeV/ $c^2$ ]
$0^{-+}0^+$	$[\pi\pi]_S$	$S$	—
$0^{-+}0^+$	$\rho(770)$	$P$	—
$0^{-+}0^+$	$f_0(980)$	$S$	1200
$0^{-+}0^+$	$f_2(1270)$	$D$	—
$0^{-+}0^+$	$f_0(1500)$	$S$	1700
$1^{++}0^+$	$[\pi\pi]_S$	$P$	—
$1^{++}1^+$	$[\pi\pi]_S$	$P$	1100
$1^{++}0^+$	$\rho(770)$	$S$	—
$1^{++}1^+$	$\rho(770)$	$S$	—
$1^{++}0^+$	$\rho(770)$	$D$	—
$1^{++}1^+$	$\rho(770)$	$D$	—
$1^{++}0^+$	$f_0(980)$	$P$	1180
$1^{++}1^+$	$f_0(980)$	$P$	1140
$1^{++}0^+$	$f_2(1270)$	$P$	1220
$1^{++}1^+$	$f_2(1270)$	$P$	—
$1^{++}0^+$	$f_2(1270)$	$F$	—
$1^{++}0^+$	$\rho_3(1690)$	$D$	—
$1^{++}0^+$	$\rho_3(1690)$	$G$	—
$1^{-+}1^+$	$\rho(770)$	$P$	—
$2^{++}1^+$	$\rho(770)$	$D$	—
$2^{++}2^+$	$\rho(770)$	$D$	—
$2^{++}1^+$	$f_2(1270)$	$P$	1000
$2^{++}2^+$	$f_2(1270)$	$P$	1400
$2^{++}1^+$	$\rho_3(1690)$	$D$	800
$2^{-+}0^+$	$[\pi\pi]_S$	$D$	—
$2^{-+}1^+$	$[\pi\pi]_S$	$D$	—
$2^{-+}0^+$	$\rho(770)$	$P$	—
$2^{-+}1^+$	$\rho(770)$	$P$	—
$2^{-+}2^+$	$\rho(770)$	$P$	—
$2^{-+}0^+$	$\rho(770)$	$F$	—
$2^{-+}1^+$	$\rho(770)$	$F$	—
$2^{-+}0^+$	$f_0(980)$	$D$	1160
$2^{-+}0^+$	$f_2(1270)$	$S$	—
$2^{-+}1^+$	$f_2(1270)$	$S$	1100
$2^{-+}2^+$	$f_2(1270)$	$S$	—
$2^{-+}0^+$	$f_2(1270)$	$D$	—
$2^{-+}1^+$	$f_2(1270)$	$D$	—
$2^{-+}2^+$	$f_2(1270)$	$D$	—
$2^{-+}0^+$	$f_2(1270)$	$G$	—
$2^{-+}0^+$	$\rho_3(1690)$	$P$	1000
$2^{-+}1^+$	$\rho_3(1690)$	$P$	1300
$3^{++}0^+$	$[\pi\pi]_S$	$F$	1380
$3^{++}1^+$	$[\pi\pi]_S$	$F$	1380
$3^{++}0^+$	$\rho(770)$	$D$	—
$3^{++}1^+$	$\rho(770)$	$D$	—
$3^{++}0^+$	$\rho(770)$	$G$	—
$3^{++}1^+$	$\rho(770)$	$G$	—
$3^{++}0^+$	$f_2(1270)$	$P$	960
$3^{++}1^+$	$f_2(1270)$	$P$	1140
$3^{++}0^+$	$\rho_3(1690)$	$S$	1380
$3^{++}1^+$	$\rho_3(1690)$	$S$	1380
$3^{++}0^+$	$\rho_3(1690)$	$I$	—

(Table continued)

TABLE IX. (*Continued*)

$J^{PC}M^e$	Isobar	$L$	Threshold [MeV/ $c^2$ ]
$3^{-+}1^+$	$\rho(770)$	$F$	—
$3^{-+}1^+$	$f_2(1270)$	$D$	1340
$4^{++}1^+$	$\rho(770)$	$G$	—
$4^{++}2^+$	$\rho(770)$	$G$	—
$4^{++}1^+$	$f_2(1270)$	$F$	—
$4^{++}2^+$	$f_2(1270)$	$F$	—
$4^{++}1^+$	$\rho_3(1690)$	$D$	1700
$4^{-+}0^+$	$[\pi\pi]_S$	$G$	1400
$4^{-+}0^+$	$\rho(770)$	$F$	—
$4^{-+}1^+$	$\rho(770)$	$F$	—
$4^{-+}0^+$	$f_2(1270)$	$D$	—
$4^{-+}1^+$	$f_2(1270)$	$D$	—
$4^{-+}0^+$	$f_2(1270)$	$G$	1600
$5^{++}0^+$	$[\pi\pi]_S$	$H$	—
$5^{++}1^+$	$[\pi\pi]_S$	$H$	—
$5^{++}0^+$	$\rho(770)$	$G$	—
$5^{++}0^+$	$f_2(1270)$	$F$	980
$5^{++}1^+$	$f_2(1270)$	$F$	—
$5^{++}0^+$	$f_2(1270)$	$H$	—
$5^{++}0^+$	$\rho_3(1690)$	$D$	1360
$6^{++}1^+$	$\rho(770)$	$I$	—
$6^{++}1^+$	$f_2(1270)$	$H$	—
$6^{-+}0^+$	$[\pi\pi]_S$	$I$	—
$6^{-+}1^+$	$[\pi\pi]_S$	$I$	—
$6^{-+}0^+$	$\rho(770)$	$H$	—
$6^{-+}1^+$	$\rho(770)$	$H$	—
$6^{-+}0^+$	$f_2(1270)$	$G$	—
$6^{-+}0^+$	$\rho_3(1690)$	$F$	—
$1^{++}1^-$	$\rho(770)$	$S$	—
$1^{-+}0^-$	$\rho(770)$	$P$	—
$1^{-+}1^-$	$\rho(770)$	$P$	—
$2^{++}0^-$	$\rho(770)$	$D$	—
$2^{++}0^-$	$f_2(1270)$	$P$	1180
$2^{++}1^-$	$f_2(1270)$	$P$	1300
$2^{-+}1^-$	$f_2(1270)$	$S$	—
Flat			—

## APPENDIX A: WAVE SET

Table IX lists the wave set used for the mass-independent fit. Note that in the reflectivity basis  $J^{PC} = (\text{even})^{++}$  waves with  $M^e = 0^+$  are mathematically forbidden [see Eq. (19) on page 18].

## APPENDIX B: SYSTEMATIC STUDIES OF PARTIAL-WAVE ANALYSIS MODEL

### 1. Rank of spin-density matrix

As pointed out in Sec. III C, ranks  $N_r > 1$  of the spin-density matrix provide a way of modeling incoherences between partial waves. This is done by introducing additional sets of transition amplitudes. These sets are assumed to correspond to different noninterfering production processes, each with its own production phase. By performing

the analysis in bins of  $t'$ , it was found that  $N_r = 1$  is sufficient for positive-reflectivity waves. This also leads to higher stability of the mass-independent fits.

In Fig. 44, we show in red the intensities of selected partial waves obtained from fits with rank 2 for the positive and negative-reflectivity waves. This is compared to the standard fit (blue data points), where rank 2 was used only for waves with  $\varepsilon = -1$ . In the rank-2 fit, the flat wave disappears completely and the intensity of the negative-reflectivity waves is approximately halved. Slight modifications of the shape of resonance structures are observed in some partial waves. Several partial waves exhibit artificial peak structures in the 1.0 to 1.3 GeV/ $c^2$   $3\pi$  mass region, like e.g. shown in Fig. 44(d). Altogether, we prefer to use rank 1 for the positive reflectivity waves.

### 2. Omission of waves with negative reflectivity

The PWA model defined in Sec. III has two types of incoherent contributions, rank and reflectivity [see Eq. (24)]. The latter one is determined by the naturality of the exchange particle (Regge-trajectory) mediating the scattering process. Including  $\varepsilon = -1$  partial waves, we effectively allow for the exchange of Reggeons other than the Pomeron, which is expected to be suppressed at beam energies of 190 GeV. In our PWA model, we have included seven waves with negative reflectivity (see Table IX in Appendix A). Negative and positive-reflectivity waves have different angular distributions. In order to study how well the fit is able to separate the two sectors, we have performed fits without any  $\varepsilon = -1$  waves. The result is shown in red in Fig. 45 for two selected waves. With the exception of the flat wave, the intensities of all waves stay practically unaltered. This demonstrates that the positive and negative-reflectivity sectors are well separated by the analysis method.

### 3. Variation of the isobar parametrization

In the employed PWA method, the  $X^-$  decay amplitudes  $\Psi_a^\varepsilon(\tau)$  [see Eq. (24)] are not allowed to have any free parameter. Fixed parametrizations for the isobar amplitudes  $\Delta_\xi(m_\xi)$  [see Eq. (8)] have to be used, which are taken from literature (see Table III). While eventually these parametrizations could be extracted from our data following the analysis scheme outlined in Sec. VI, for this paper we still use the conventional approach.

The  $\rho(770)$  is the dominant isobar. As discussed in Sec. IV A, different Breit-Wigner parametrizations exist for the  $\rho(770)$ . Using Eq. (32) instead of Eq. (40) for the mass-dependent width  $\Gamma(m)$  of the  $\rho(770)$  changes the intensity of the structure in the  $a_1(1260)$  mass region in the  $1^{++}0^+[\pi\pi]_S\pi P$  wave and that of the  $a_2(1320)$  signal in the  $2^{++}1^+f_2(1270)\pi P$  wave (see Fig. 46). Both structures seem to be contaminated by model leakage from the respective dominant  $\rho(770)\pi$  decay modes. The other 16 waves listed in Table V remain practically unchanged. When

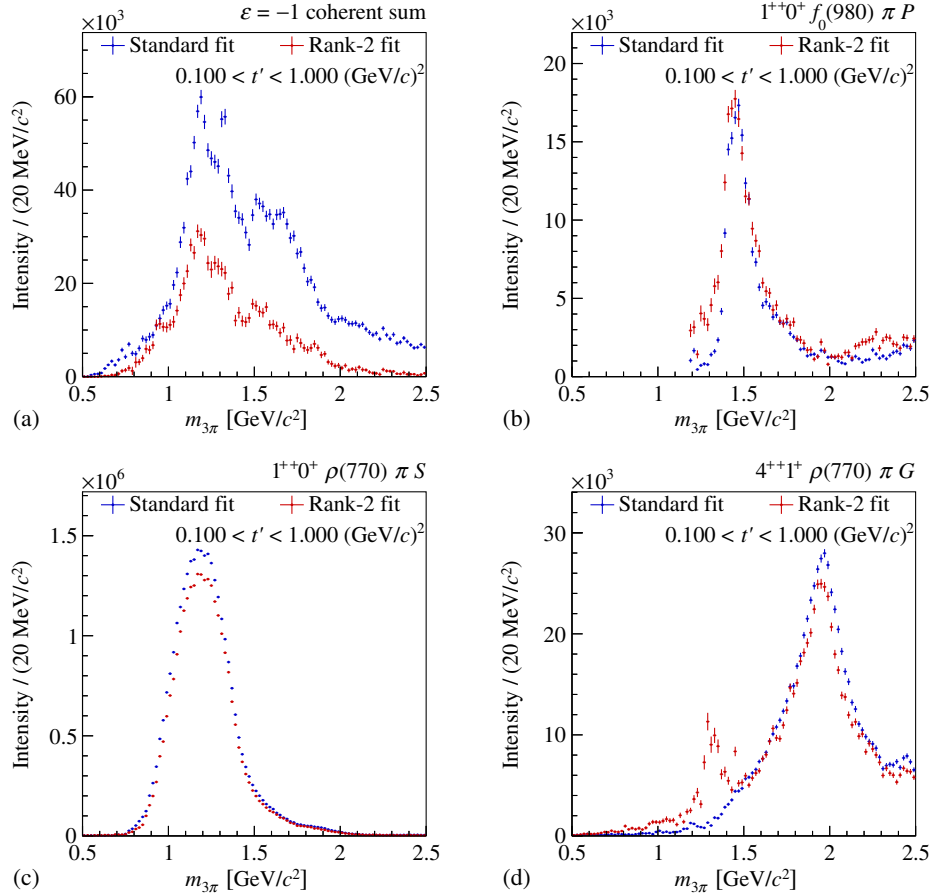


FIG. 44. Comparison of  $t'$ -summed partial-wave intensities obtained from the standard mass-independent fit with rank  $N_r = 1$  of the spin-density matrix for waves with  $\epsilon = +1$  and rank 2 for the ones with  $\epsilon = -1$  (blue/black) with the intensities from a fit with rank 2 for both sectors (red/gray).

using in addition the PDG averages for the  $\rho(770)$  parameters of  $m_0 = 775.26 \text{ MeV}/c^2$  and  $\Gamma_0 = 149.1 \text{ MeV}/c^2$  [9], the log-likelihood values, summed over the 11  $t'$  bins, decrease by more than 1000 units in the mass range between 0.95 and  $1.35 \text{ GeV}/c^2$ .

We have also investigated the sensitivity of the PWA result with respect to changes in the parametrization of the  $f_0(980)$  and  $[\pi\pi]_S$  isobars. For the  $f_0(980)$ , the Flatté parametrization used in the standard analysis is replaced by a modified  $S$ -wave Breit-Wigner amplitude of the form:

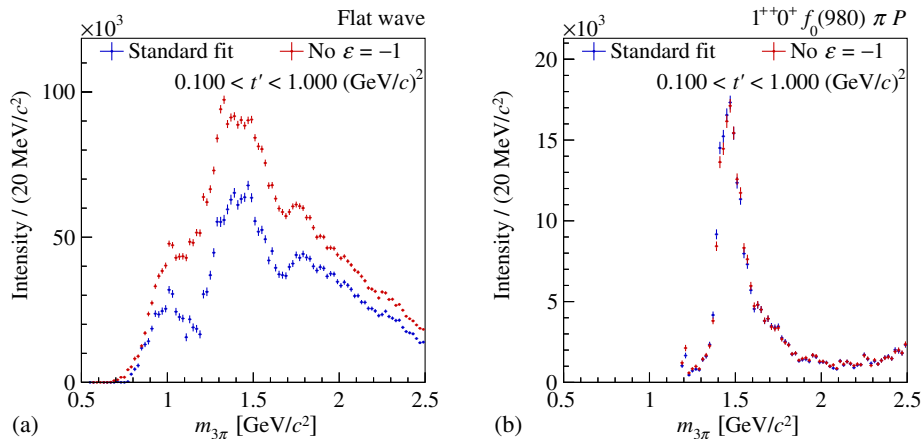


FIG. 45. Comparison of  $t'$ -summed partial-wave intensities obtained from the mass-independent fits with (blue/black) and without (red/gray)  $\epsilon = -1$  waves.

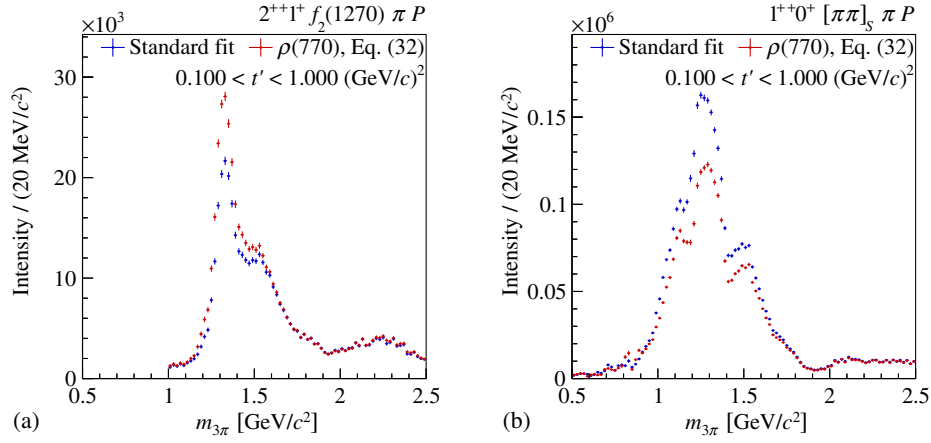


FIG. 46. Comparison of  $t'$ -summed partial-wave intensities obtained from mass-independent fits using two different parametrizations for the  $\rho(770)$  isobar amplitude: a Breit-Wigner with Eq. (40) (blue/black) and one with Eq. (32) (red/gray).

$$\Delta_{f_0(980)}(m; m_0, \Gamma_0) = \frac{m\Gamma_0}{m_0^2 - m^2 - im_0\Gamma(m)}, \quad (\text{B1})$$

where

$$\Gamma(m) = \Gamma_0 \frac{q}{q_0}. \quad (\text{B2})$$

The  $f_0(980)$  parameters are  $m_0 = 980 \text{ MeV}/c^2$  and  $\Gamma_0 = 40 \text{ MeV}/c^2$ . Figure 47 shows in red some selected partial-wave intensities from this study. The Breit-Wigner parametrization has less pronounced tails and covers a narrower  $2\pi$  mass range. This leads to nearly a factor of two lower intensities in the  $f_0(980)$   $\pi$  partial waves. The shapes

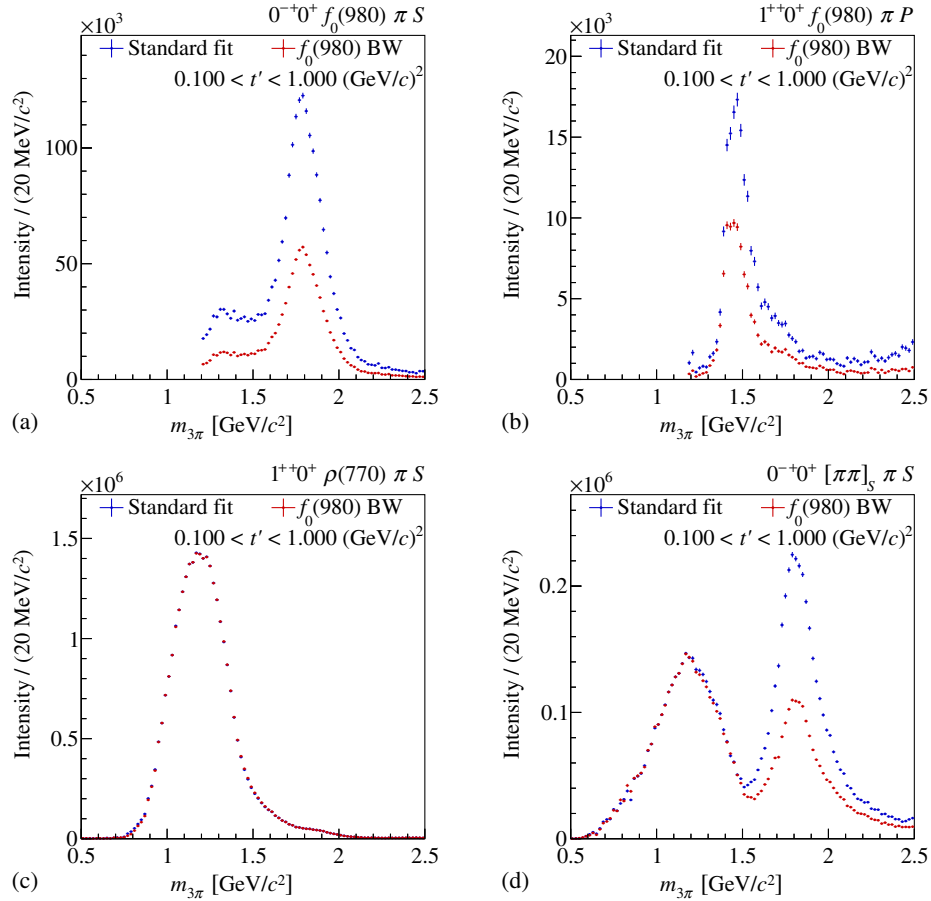


FIG. 47. Comparison of  $t'$ -summed partial-wave intensities obtained from mass-independent fits using two different parametrizations for the  $f_0(980)$  isobar amplitude: Flatté parametrization [Eq. (43), blue/black] and modified  $S$ -wave Breit-Wigner [Eq. (B1) with Eq. (B2), red/gray].

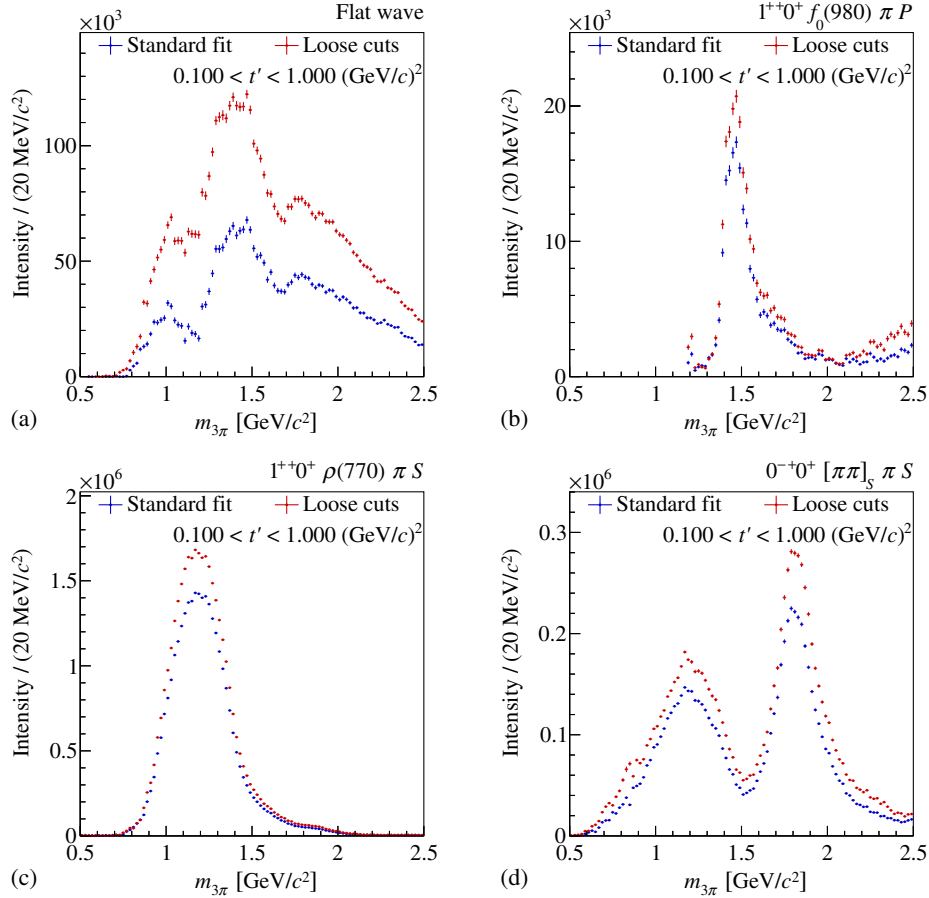


FIG. 48. Comparison of  $t'$ -summed partial-wave intensities obtained from mass-independent fits for standard event selection (blue/black) and a looser event selection (red/gray), where particle identification and central-production rejection have not been applied.

of the resonance structures in these waves remain unaltered. Interestingly, the  $\pi(1800)$  peak in the  $0^{-+}0^+[\pi\pi]_S\pi S$  wave also decreases when the Breit-Wigner parametrization is used for the  $f_0(980)$ . On the level of the mass-independent fit, this behavior cannot be explained. In contrast to the  $\pi(1800)$  peak, the structure in the  $\pi(1300)$  region remains

unaltered. The fit with the Flatté parametrization has a higher likelihood than the fit with the Breit-Wigner one.

Also for the broad component of the  $\pi\pi$  S-wave amplitude various parametrizations exist. In addition to the modified  $M$  solution from Ref. [41], we tried the  $K_1$  solution from Ref. [41] with the  $f_0(980)$  pole subtracted,

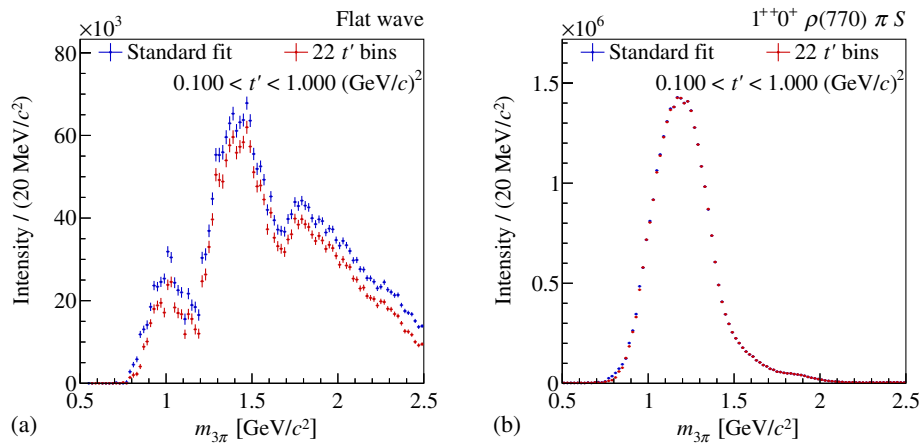


FIG. 49. Comparison of  $t'$ -summed partial-wave intensities obtained from mass-independent fits using two different  $t'$  binnings: 11  $t'$  bins (blue/black) and 22  $t'$  bins (red/gray).

using the modified  $S$ -wave Breit-Wigner amplitude of Eq. (B1) with Eq. (B2) [20]. In order to be consistent, the same  $f_0(980)$  amplitude was also used for the partial waves with the  $f_0(980)$  isobar. The result is very similar to the one of the fit with the modified  $M$  solution for the  $[\pi\pi]_S$  and the  $S$ -wave Breit-Wigner amplitude for the  $f_0(980)$  isobar discussed above.

#### 4. Variation of event selection

In order to study the potential influence of backgrounds from kaon diffraction, kaon pairs in the final state, and central-production reactions, the mass-independent fit was performed on a data sample, in which the particle identification in the

beam and spectrometer was not used and the rejection of central-production events as described in Sec. II C was not applied. Therefore, possible background contributions are expected to be enhanced in this data sample. The effect is shown in Fig. 48 for selected waves. The data sample with looser cuts contains approximately 20% more events in the analyzed range of  $m_{3\pi}$  and  $t'$ . Hence, the partial-wave intensities are larger and typically scale proportionally to the sample size. The peak shapes of resonances are in general unaffected by the different event selection. The most noteworthy effects of the looser cuts are an over-proportional increase of the flat-wave intensity by nearly a factor of two and an enhancement of structures at large  $3\pi$  masses in some waves.

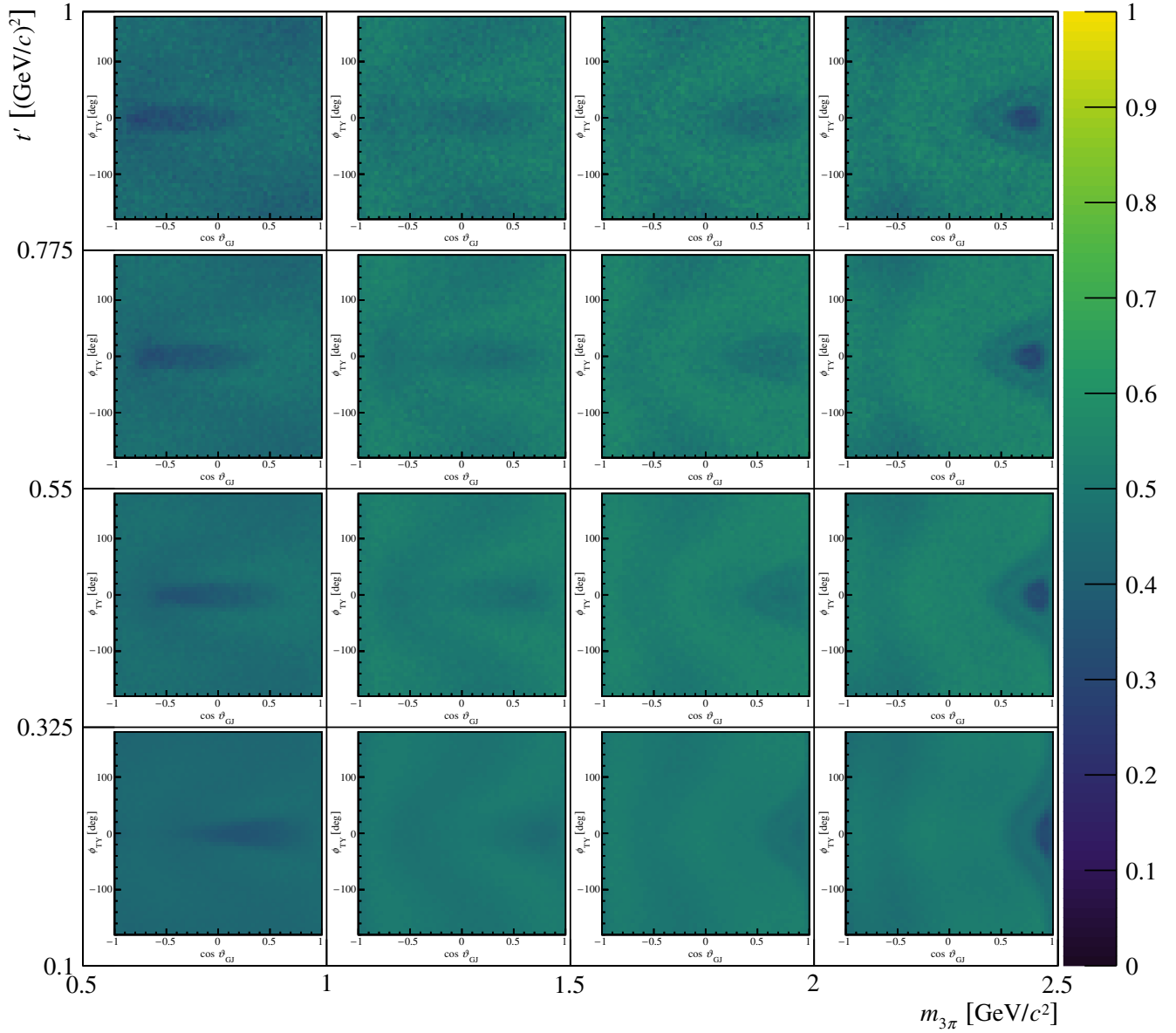


FIG. 50. Detection efficiency for  $\pi^-\pi^-\pi^+$  phase-space events in different regions of  $m_{3\pi}$  and  $t'$ . Each graph shows the detection efficiency as a function of the angles,  $\cos\vartheta_{GJ}$  (abscissa, from  $-1$  to  $+1$ ) and  $\phi_{TY}$  (ordinate, from  $-180^\circ$  to  $+180^\circ$ ), of the isobar in the Gottfried-Jackson frame.

### 5. Variation of $t'$ binning

In order to study, whether the chosen binning in the four-momentum transfer squared  $t'$  has any effect on the partial-wave analysis, the  $t'$  bins defined in Table IV and shown in Fig. 11 where halved, yielding in total 22 bins. The finer  $t'$  binning has practically no effect on the partial-wave intensities (see Fig. 49). Only the flat wave has lower intensity over the full  $m_{3\pi}$  range in the case of finer  $t'$  bins.

### APPENDIX C: ACCEPTANCE

In the following, we describe the  $\pi^-\pi^-\pi^+$  detection efficiency of the COMPASS apparatus in absolute terms. For this we have generated  $3\pi$  events distributed

isotropically in phase space and passed them through the COMPASS detector simulation and reconstruction chain. The same selection cuts were applied as used for the real data. For fixed values of  $m_{3\pi}$  and  $t'$ , the acceptance is a five-dimensional function, of which we show only projections.

Figure 50 shows the  $\pi^-\pi^-\pi^+$  detection efficiency as a function of the two angles,  $\cos\vartheta_{\text{GJ}}$  and  $\phi_{\text{TY}}$ , of the isobar in the Gottfried-Jackson frame (see Sec. III A for the definition). The acceptance is shown in four regions of  $m_{3\pi}$  and  $t'$ . The Monte Carlo data show a rather flat acceptance with a small dip for in-plane events at forward angles. This structure exhibits some dependence on  $t'$  and mass. The corresponding distributions in the helicity frame are shown in Fig. 51. Here, no significant structures are visible.

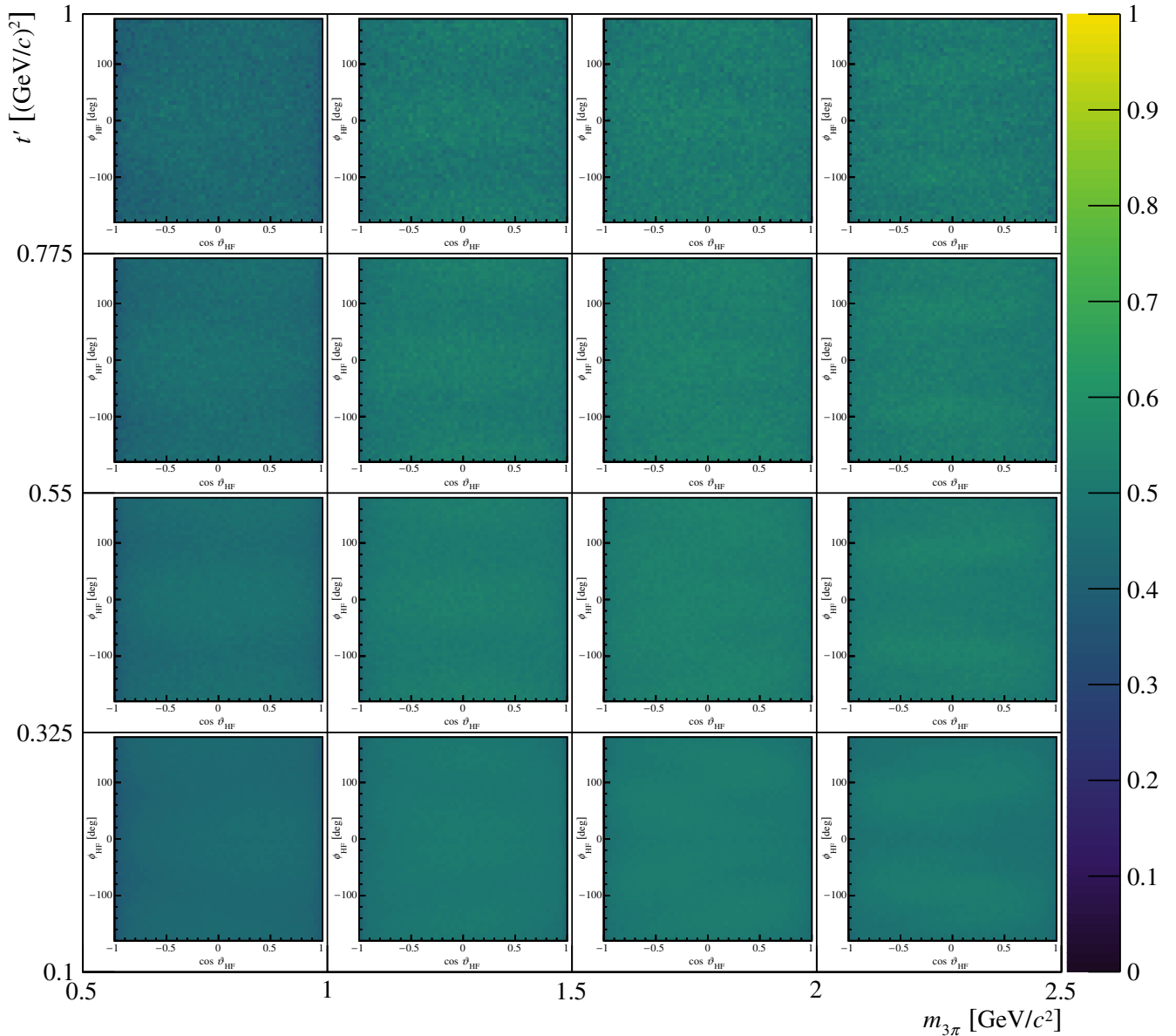


FIG. 51. Same as Fig. 50, but for the detection efficiency as a function of the angles,  $\cos\vartheta_{\text{HF}}$  and  $\phi_{\text{HF}}$ , of the  $\pi^-$  in the helicity frame.

- [1] E. Klempt and A. Zaitsev, *Phys. Rep.* **454**, 1 (2007).
- [2] C. Amsler, S. Eidelman, T. Gutsche, C. Hanhart, S. Spanier, and N. A. Törnqvist, *Chin. Phys. C* **38**, 784 (2014).
- [3] C. A. Meyer and E. S. Swanson, *Prog. Part. Nucl. Phys.* **82**, 21 (2015).
- [4] C. A. Meyer and Y. V. Haarlem, *Phys. Rev. C* **82**, 025208 (2010).
- [5] W. Ochs, *J. Phys. G* **40**, 043001 (2013).
- [6] V. Crede and C. A. Meyer, *Prog. Part. Nucl. Phys.* **63**, 74 (2009).
- [7] C. Adolph *et al.* (COMPASS Collaboration), *Eur. Phys. J. A* **50**, 79 (2014).
- [8] M. Alekseev *et al.* (COMPASS Collaboration), *Phys. Rev. Lett.* **104**, 241803 (2010).
- [9] K. A. Olive *et al.* (Particle Data Group Collaboration), *Chin. Phys. C* **38**, 090001 (2014).
- [10] N. Brambilla, S. Eidelman, P. Foka, S. Gardner, A. S. Kronfeld *et al.*, *Eur. Phys. J. C* **74**, 2981 (2014).
- [11] G. Ascoli, D. V. Brockway, H. B. Crawley, B. I. Eisenstein, R. W. Hanft, M. L. Ioffredo, and U. E. Kruse, *Phys. Rev. Lett.* **25**, 962 (1970).
- [12] G. Ascoli *et al.*, *Phys. Rev. D* **7**, 669 (1973).
- [13] C. Daum *et al.* (ACCMOR Collaboration), *Phys. Lett.* **89B**, 285 (1980).
- [14] C. Daum *et al.* (ACCMOR Collaboration), *Phys. Lett. B* **89B**, 276 (1980).
- [15] C. Daum *et al.* (ACCMOR Collaboration), *Phys. Lett.* **89B**, 281 (1980).
- [16] C. Daum *et al.* (ACCMOR Collaboration), *Nucl. Phys.* **B182**, 269 (1981).
- [17] G. S. Adams *et al.* (E852 Collaboration), *Phys. Rev. Lett.* **81**, 5760 (1998).
- [18] S. U. Chung *et al.* (E852 Collaboration), *Phys. Rev. D* **65**, 072001 (2002).
- [19] A. R. Dzierba, R. Mitchell, E. Scott, M. R. Shepherd, P. Smith, M. Swat, S. Teige, A. P. Szczepaniak, S. P. Denisov, V. Dorofeev, I. Kachaev, V. Lipaev, A. V. Popov, D. I. Ryabchikov, V. A. Bodyagin, and A. Demianov, *Phys. Rev. D* **73**, 072001 (2006).
- [20] D. V. Amelin *et al.* (VES Collaboration), *Phys. Lett. B* **356**, 595 (1995).
- [21] Y. A. Khokhlov (VES Collaboration), *Nucl. Phys.* **A663**, 596 (2000).
- [22] I. Kachaev *et al.* (VES Collaboration), *AIP Conf. Proc.* **619**, 577 (2002).
- [23] Yu. Khokhlov, V. Dorofeev, A. Ekimov, Y. Gouz, A. Ivashin, I. Kachaev, A. Karyukhin, V. Konstantinov, V. Matveev, V. Nikolaenko, B. Polyakov, D. Ryabchikov, A. A. Solodkov, A. V. Solodkov, O. Solovianov, and A. Zaitsev, *Nucl. Phys. B, Proc. Suppl.* **225–227**, 27 (2012).
- [24] S. Donnachie, H. G. Dosch, O. Nachtmann, and P. Landshoff, *Cambridge Monogr. Part. Phys., Nucl. Phys., Cosmol.* **19**, 1 (2002).
- [25] R. T. Deck, *Phys. Rev. Lett.* **13**, 169 (1964).
- [26] M. Jacob and G. C. Wick, *Ann. Phys. (N.Y.)* **7**, 404 (1959).
- [27] S.-U. Chung, Report No. BNL-76975-2006-IR, 2013 updated version of Report No. CERN-71-08.
- [28] J. D. Hansen, G. T. Jones, G. Otter, and G. Rudolph, *Nucl. Phys.* **B81**, 403 (1974).
- [29] S. U. Chung and T. L. Trueman, *Phys. Rev. D* **11**, 633 (1975).
- [30] D. Herndon, P. Soding, and R. J. Cashmore, *Phys. Rev. D* **11**, 3165 (1975).
- [31] J. D. Richman, Report No. CALT-68-1148, 1984.
- [32] C. W. Salgado and D. P. Weygand, *Phys. Rep.* **537**, 1 (2014), and references therein.
- [33] COMPASS Collaboration (to be published).
- [34] P. Abbon *et al.* (COMPASS Collaboration), *Nucl. Instrum. Methods Phys. Res., Sect. A* **577**, 455 (2007).
- [35] P. Abbon *et al.* (COMPASS Collaboration), *Nucl. Instrum. Methods Phys. Res., Sect. A* **779**, 69 (2015).
- [36] J. Bernhard, Ph. D. thesis, Johannes-Gutenberg-Universität, 2014.
- [37] F. Haas, Ph. D. thesis, Technische Universität München, 2014; Report No. CERN-THESIS-2013-277.
- [38] C. Zemach, *Phys. Rev.* **140**, B97 (1965).
- [39] C. Zemach, *Phys. Rev.* **140**, B109 (1965).
- [40] S.-U. Chung and J. M. Friedrich, *Phys. Rev. D* **78**, 074027 (2008).
- [41] K. L. Au, D. Morgan, and M. R. Pennington, *Phys. Rev. D* **35**, 1633 (1987).
- [42] M. Ablikim *et al.* (BES Collaboration), *Phys. Lett. B* **607**, 243 (2005).
- [43] G. Breit and E. Wigner, *Phys. Rev.* **49**, 519 (1936).
- [44] J. Blatt and V. Weisskopf, *Theoretical Nuclear Physics* (John Wiley & Sons, New York, 1952).
- [45] F. von Hippel and C. Quigg, *Phys. Rev. D* **5**, 624 (1972).
- [46] J. Pišút and M. Roos, *Nucl. Phys.* **B6**, 325 (1968).
- [47] M. G. Bowler, *Phys. Lett. B* **182**, 400 (1986).
- [48] S. M. Flatté, *Phys. Lett.* **63B**, 228 (1976).
- [49] I. A. Kachaev, in *3rd International Conference on Quarks and Nuclear Physics QNP* (Bloomington, IN, U.S.A., 2004).
- [50] Supplemental Material at <http://link.aps.org/supplemental/10.1103/PhysRevD.95.032004>.
- [51] C. Adolph *et al.* (COMPASS Collaboration), *Phys. Lett. B* **740**, 303 (2015).
- [52] T. Barnes, F. E. Close, P. R. Page, and E. S. Swanson, *Phys. Rev. D* **55**, 4157 (1997).
- [53] F. E. Close and P. R. Page, *Nucl. Phys.* **B443**, 233 (1995).
- [54] P. R. Page, E. S. Swanson, and A. P. Szczepaniak, *Phys. Rev. D* **59**, 034016 (1999).
- [55] J. Dudek and A. Szczepaniak, *AIP Conf. Proc.* **814**, 587 (2006).
- [56] C. Adolph *et al.* (COMPASS Collaboration), *Phys. Rev. Lett.* **115**, 082001 (2015).
- [57] F. Haas (COMPASS Collaboration), eConf **C110613** (2011), [arXiv:1109.1789](https://arxiv.org/abs/1109.1789).
- [58] G. Ascoli, L. M. Jones, B. Weinstein, and H. W. Wyld, *Phys. Rev. D* **8**, 3894 (1973).
- [59] G. Ascoli, R. Cutler, L. M. Jones, U. Kruse, T. Roberts, B. Weinstein, and H. W. Wyld, *Phys. Rev. D* **9**, 1963 (1974).
- [60] G. Cohen-Tannoudji, A. Santoro, and M. Souza, *Nucl. Phys.* **B125**, 445 (1977).
- [61] G. Cohen-Tannoudji, D. Levy, and M. Souza, *Nucl. Phys.* **B129**, 286 (1977).
- [62] A. C. B. Antunes, A. F. S. Santoro, and M. H. G. Souza, *Rev. Bras. Fis.* **14**, 397 (1984).

- [63] M. L. Perl, *High Energy Hadron Physics* (Wiley, New York, 1974).
- [64] T. Schlüter (COMPASS Collaboration), eConf **C110613** (2011), [arXiv:1108.6191](https://arxiv.org/abs/1108.6191).
- [65] E. M. Aitala *et al.* (E791 Collaboration), *Phys. Rev. D* **73**, 032004 (2006).
- [66] B. Aubert *et al.* (BABAR Collaboration), *Phys. Rev. D* **79**, 032003 (2009).